# Tectonic evolution of the Qilian Shan: An early Paleozoic orogen reactivated in the Cenozoic

Andrew V. Zuza[1,2,†], Chen Wu[3], Robin C. Reith[1], An Yin[1,3], Jianhua Li[4], Jinyu Zhang[5], Yuxiu Zhang[6], Long Wu[3], and Wencan Liu[3]

[1]*Department of Earth, Planetary, and Space Sciences, University of California, Los Angeles, California 90095-1567, USA*
[2]*Nevada Bureau of Mines and Geology, University of Nevada, Reno, Nevada 89557, USA*
[3]*Structural Geology Group, China University of Geosciences (Beijing), Beijing 10083, China*
[4]*Institute of Geomechanics, Chinese Academy of Geological Sciences, Beijing 100081, China*
[5]*Institute of Geology, China Earthquake Administration, Beijing 100029, China*
[6]*Asian Tectonics Research Group and College of Earth Science, Chinese Academy of Sciences, Beijing 100049, China*

## ABSTRACT

The Qilian Shan, located along the northeastern margin of the Tibetan Plateau, has experienced multiple episodes of tectonic deformation, including Neoproterozoic continental breakup, early Paleozoic subduction and continental collision, Mesozoic extension, and Cenozoic intracontinental orogenesis resulting from the India-Asia collision. In the central Qilian Shan, pre-Mesozoic ophiolite complexes, passive-continental margin sequences, and strongly deformed forearc strata were juxtaposed against arc plutonic/volcanic rocks and ductilely deformed crystalline rocks during the early Paleozoic Qilian orogen. To better constrain this orogen and the resulting closure of the Neoproterozoic–Ordovician Qilian Ocean, we conducted an integrated investigation involving geologic mapping, U-Th-Pb zircon and monazite geochronology, whole-rock geochemistry, thermobarometry, and synthesis of existing data sets across northern Tibet. The central Qilian Shan experienced two phases of arc magmatism at 960–870 Ma and 475–445 Ma that were each followed by periods of protracted continental collision. Integrating our new data with previously published results, we propose the following tectonic model for the Proterozoic–Paleozoic history of northern Tibet. (1) Early Neoproterozoic subduction accommodated the convergence and collision between the South Tarim–Qaidam and North Tarim–North China continents. (2) Late Neoproterozoic rifting partially separated a peninsular Kunlun-Qaidam continent from the southern margin of the linked Tarim–North China craton and opened the Qilian Ocean as an embayed marginal sea; this separation broadly followed the trace of the earlier Neoproterozoic suture zone. (3) South-dipping subduction along the northern margin of the Kunlun-Qaidam continent initiated in the Cambrian, first developing as the Yushigou supra-subduction zone ophiolite and then transitioning into the continental Qilian arc. (4) South-dipping subduction, arc magmatism, and the convergence between Kunlun-Qaidam and North China continued throughout the Ordovician, with a trench-parallel intra-arc strike-slip fault system that is presently represented by high-grade metamorphic rocks that display a pervasive right-lateral shear sense. (5) Counterclockwise rotation of the peninsular Kunlun-Qaidam continent toward North China led to the closure of the Qilian Ocean, which is consistent with the right-lateral kinematics of intra-arc strike-slip faulting observed in the Qilian Shan and the westward tapering map-view geometry of Silurian flysch-basin strata. Continental collision at ca. 445–440 Ma led to widespread plutonism across the Qilian Shan and is recorded by recrystallized monazite (ca. 450–420 Ma) observed in this study. Our tectonic model implies the parallel closure of two oceans of different ages along the trace of the Qilian suture zone since ca. 1.0 Ga. In addition, the Qilian Ocean was neither the Proto- nor Paleo-Tethys (i.e., the earliest ocean separating Gondwana from Laurasia), as previously suggested, but was rather a relatively small embayed sea along the southern margin of the Laurasian continent. We also document >200 km of Cenozoic north-south shortening across the study area. The observed shortening distribution supports models of Tibetan Plateau development that involve distributed crustal shortening and southward underthrusting of Eurasia beneath the plateau. This India-Asia convergence-related deformation is focused along the sites of repeated ocean closure. Major Cenozoic left-slip faults parallel these sutures, and preexisting subduction-mélange channels may have facilitated Cenozoic shortening and continental underthrusting.

## INTRODUCTION

Understanding the formation and evolution of Eurasia—the only continent assembled during the Phanerozoic (Scotese and McKerrow, 1990; Şengör and Natal'in, 1996; Sone and Metcalfe, 2008; Zuza and Yin, 2017)—greatly impacts our knowledge of processes of crustal formation, large-scale continental deformation (e.g., Burchfiel et al., 1989; Tapponnier et al., 2001; Xiao et al., 2004; Yin, 2010), and crustal growth (e.g., Windley, 1992; Jahn et al., 2004; Kröner et al., 2014). The assembly of the Eurasian continent occurred over a span of approximately 1 b.y., from the Neoproterozoic to the present, through multiple ocean-closure events and continental collisions (e.g., Zonenshain et al., 1990; Yin and Nie, 1996; Şengör and Natal'in, 1996; Heubeck, 2001; Badarch et al., 2002; Stampfli and Borel, 2002; Biske and Seltmann, 2010; Wu et al., 2016). The most recent of these collisions, between the Indian and Asian continents, led to the development of the Himalayan-Tibetan orogen and the related Tibetan Plateau (Fig. 1; e.g., Yin and Harrison, 2000; Royden et al., 2008; Yin, 2010).

The construction of much of the Tibetan Plateau has progressed since the Eocene (cf. Worley and Wilson, 1996; Murphy et al., 1997),
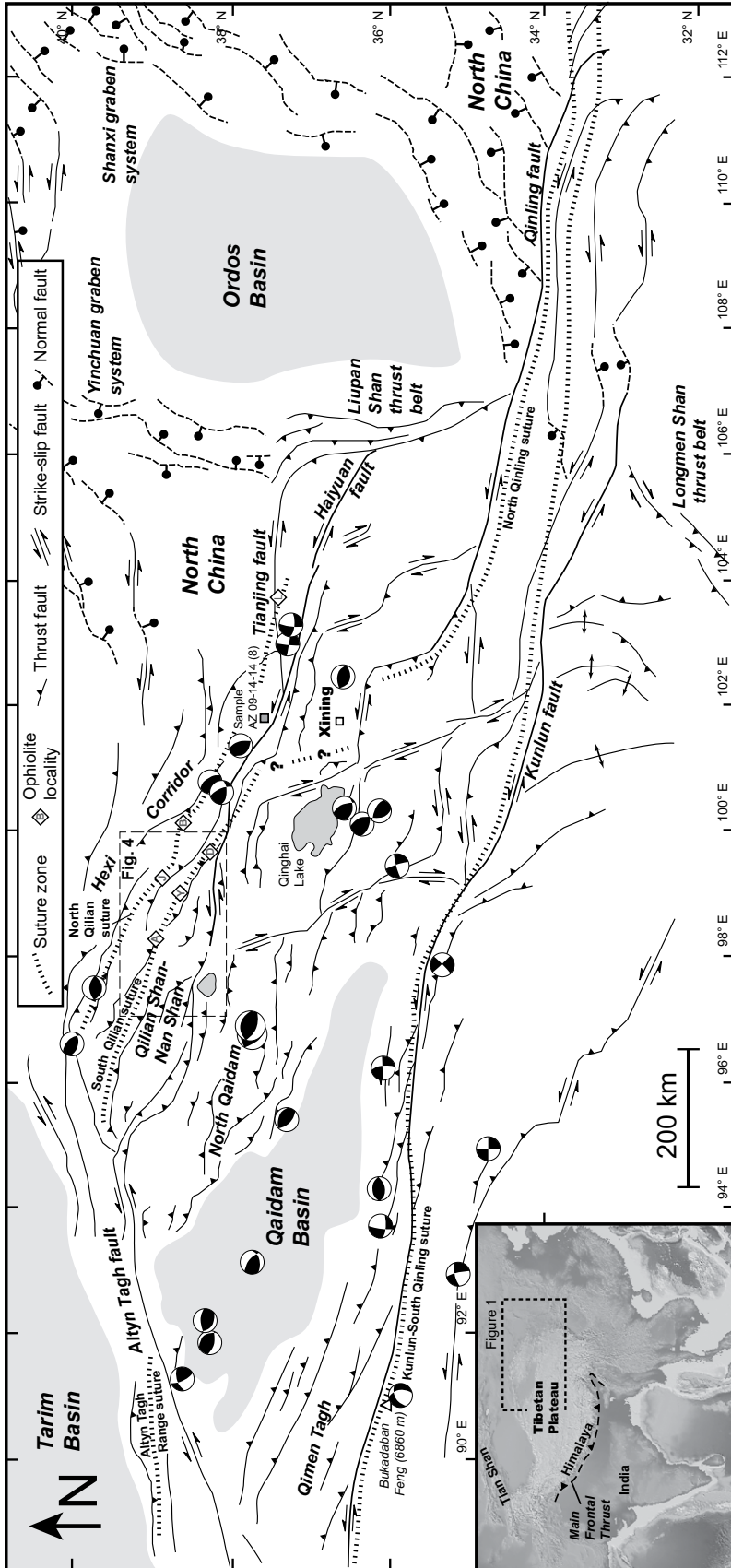
†azuza@unr.edu, avz5818@gmail.com.

**Figure 1. Regional tectonic map of the northeastern Tibetan Plateau from Yin and Harrison (2000), Taylor and Yin (2009), Gao et al. (2013), and Zuza et al. (2016). Inset shows the location of Figure 1 in the context of the India-Eurasian collision. Also shown is the location of Figure 4, and plutonic sample AZ 09-14-14 (8), which was collected outside of the mapping areas. Underlying base map is from GeoMapApp software, available online at www.geomapapp.org (Ryan et al., 2009). Abbreviated early Paleozoic Qilian ophiolites: A—Aoyougou; Y—Yushigou; D—Dongcaohe; J—Jiugequan; B—Biandukou; L—Laohushan.**

and this mostly Cenozoic feature overprints several major Proterozoic through Mesozoic collision and accretion events (e.g., Şengör and Natal'in, 1996; Heubeck, 2001; Burchfiel and Chen, 2012; Wu et al., 2016). Observations from decades of geologic and geophysical research support the growth of the Tibetan Plateau by a variety of processes, including: (1) Cenozoic lithospheric shortening through pure-shear thickening (e.g., Dewey and Bird, 1970; Dewey and Burke, 1973; England and Houseman, 1986; Dewey, 1988), (2) underthrusting of Indian or Asian lithosphere beneath the Tibetan crust (Argand, 1924; Willett and Beaumont, 1994; DeCelles et al., 2002; Kind et al., 2002; van Hinsbergen et al., 2011, 2012; Ye et al., 2015; Zuza et al., 2016), (3) removal of Tibetan mantle lithosphere and subsequent plateau uplift (e.g., England and Houseman, 1989; Harrison et al., 1992; Molnar et al., 1993), (4) middle- and/or lower-crustal channel flow driven by lateral pressure gradients (Zhao and Morgan, 1987; Bird, 1991; Royden et al., 1997; Clark and Royden 2000; Royden et al., 2008), (5) intracontinental subduction coupled with or without lateral extrusion along major strike-slip faults (Meyer et al., 1998; Tapponnier et al., 1990, 2001; Wang et al., 2001), (6) syncollision magmatic addition (Yin and Harrison, 2000; Mo et al., 2007), and/or (7) pre-Cenozoic crustal thickening (Worley and Wilson, 1996; Murphy et al., 1997; Wallis et al., 2003).

Detailed knowledge of the initial lithospheric conditions, prior to India-Asian collision at 65–55 Ma (e.g., Le Pichon et al., 1992; Zhu et al., 2005; Yin, 2010; van Hinsbergen et al., 2011; Hu et al., 2015), is required to test these models and advance our understanding of continental tectonics. For example, the existence of any precollisional topography in Tibet (e.g., Murphy et al., 1997; Kapp et al., 2005, 2007) changes the predicted timing, style, and magnitude of Cenozoic deformation required to generate the present-day morphology of the plateau (e.g., England and Searle, 1986; Kong et al., 1997; Liu-Zeng et al., 2008; Yang and Liu, 2009). In addition, well-constrained strain markers used to quantify Cenozoic deformation require an understanding of the Paleozoic and/or Mesozoic structural framework of Central Asia (e.g., Zhou and Graham, 1996; Sobel and Arnaud, 1999; Cowgill et al., 2003; Gehrels et al., 2003a, 2003b; Zuza and Yin, 2017).

This issue is particularly significant along the plateau's northeastern margin in the Qilian Shan, to the north of the left-slip Kunlun fault (Fig. 1). The actively deforming region involved early Paleozoic orogeny (e.g., Xiao et al., 2009; Song et al., 2013) and Mesozoic extension (Vincent and Allen, 1999; Chen et al., 2003), and not

surprisingly, the interaction among Paleozoic, Mesozoic, and Cenozoic structures is complex (Sobel and Arnaud, 1999; Gehrels et al., 2003a, 2003b; Yin et al., 2007b; Wu et al., 2017a). Presently, this region is dominated by the active Qilian Shan–Nan Shan thrust belt (Molnar and Tapponnier, 1975; Gaudemer et al., 1995; Meyer et al., 1998; Yin and Harrison, 2000; Cheng et al., 2015; Zuza et al., 2016), which occupies about one fifth of the Tibetan-Himalayan orogen (Fig. 1).

The Cenozoic Qilian Shan–Nan Shan thrust belt and the North Qaidam thrust system to the south (Yin et al., 2008a, 2008b) expose the early Paleozoic Qilian suture(s), early Paleozoic Qilian orogen, southern margin of the Precambrian North China craton, and northern Kunlun-Qaidam continent with Proterozoic basement (Figs. 1 and 2; Wang et al., 2013; Wu et al., 2017a). The abundance of ophiolite-bearing mélange and blueschist assemblages in the Qilian Shan led early workers to suggest that this region represents the site of the closed Qilian Ocean (Wang and Liu, 1976; Xiao et al., 1978). This ocean opened in the Neoproterozoic and closed during the early Paleozoic Qilian orogen (e.g., Yin and Harrison, 2000; Gehrels et al., 2003a, 2003b, 2011; Yin et al., 2007b; Xiao et al., 2009; Song et al., 2013, 2014; Wu et al., 2017a). The timing, subduction polarity, and nature of the Qilian arc and Qilian orogen, which accommodated the closure of the Qilian Ocean, remain poorly constrained.

In this contribution, we address some of these issues through an integrated field and analytical study involving detailed geologic mapping (~1:50,000 scale), structural analysis, sedimentology, geochronology, thermochronology, whole-rock geochemistry, and thermobarometry across the central Qilian Shan, near the Shule, Tuo Lai, and Heihe River Valleys

(~38.5°N, ~98.5°E) in the Qinghai and Gansu Provinces of western China. Our interdependent goals were to (1) establish the structural framework and quantify the magnitude of Cenozoic crustal shortening across the central Qilian Shan–Nan Shan thrust belt, and (2) improve our understanding of the pre-Cenozoic geology of northern Tibet and specifically provide new constraints on the early Paleozoic Qilian orogen.

## REGIONAL GEOLOGY OF NORTHERN TIBET

The 350-km-wide Qilian Shan–Nan Shan thrust belt extends for 1300 km across the northeastern margin of the Tibetan Plateau (Fig. 1). Northwest-trending ranges reach elevations of 4–5 km (the highest peaks are 5.7–5.8 km), and intermontane basins are 3–4 km in elevation. The Qilian Shan–Nan Shan exhibits a triangular eastward-tapering map-view pattern that links to the east with the left-slip Haiyuan fault (Fig. 1; Gaudemer et al., 1995; Cheng et al., 2015; Zuza and Yin, 2016). The thrust belt is bounded by the left-slip Altyn Tagh fault to the west (e.g., Burchfiel et al., 1989; Meyer et al., 1998; Yin et al., 2002; Cowgill et al., 2000, 2003, 2004a, 2004b, 2009), the North Qaidam and Qaidam Basin thrust systems to the south (e.g., Huang et al., 1996; Wang et al., 2006; Yin et al., 2008a, 2008b), and the Hexi Corridor foreland to the northeast (Fig. 1; Wang and Coward, 1993; Li and Yang, 1998; Métivier et al., 1998; Bovet et al., 2009; Zuza et al., 2016). Active deformation consists of a mixed-mode of thrusting and strike-slip faulting (e.g., Gaudemer et al., 1995; Meyer et al., 1998; Zuza and Yin, 2016). The western Qilian Shan consists of thrust and left-slip faulting along the Altyn Tagh fault (Molnar and Tapponnier, 1975; Peltzer et al., 1989),

whereas the eastern Qilian Shan involves left-slip faulting on the Haiyuan fault and thrusting (Fig. 1; Burchfiel et al., 1991; Gao et al., 2013).

### Deformational History

Northern Tibet is dominated by exposures of the early Paleozoic Qilian orogen and related North Qaidam ultrahigh pressure (UHP) metamorphic belt (Figs. 1 and 2; Yin and Harrison, 2000; Yin et al., 2007b; Menold et al., 2009; Song et al., 2013, 2014). The original configuration of these rocks was modified by Mesozoic extension, resulting from the closure of the Meso- and Paleo-Tethys Oceans (Pullen et al., 2008; Zhang et al., 2014), and Cenozoic intracontinental deformation associated with the India-Asia collision (Vincent and Allen, 1999; Yin and Harrison, 2000; Chen et al., 2003; Gehrels et al., 2003a, 2003b). Next, we briefly outline the important Phanerozoic tectonic events that affected northern Tibet, starting with the early Paleozoic history and progressing toward the present.

### *Paleozoic Tectonics*

The early Paleozoic Qilian orogen records the closure of the Qilian Ocean(s) as the Kunlun-Qaidam continent collided against the southern margin of the Tarim–North China cratons (Yin and Nie, 1996; Şengör and Natal'in, 1996; Sobel and Arnaud, 1999; Yin and Harrison, 2000; Gehrels et al., 2003a, 2003b; Yin et al., 2007b; Xiao et al., 2009; Song et al., 2013, 2014; Wu et al., 2017a). From north to south, the orogen consists of the mélange-ophiolite complex of the Qilian suture(s), the Ordovician–Silurian arc belt, and the intra-arc North Qaidam UHP metamorphic belt (Fig. 2; Yin and Harrison, 2000; Yin et al., 2007b; Menold et al., 2009, 2016; Song et al., 2013, 2014). Flysch, arc-type assem-



**Figure 2. Simplified sketch of important continents, cratons, and sutures in northern Tibet, including the Tarim craton, North China craton, and Kunlun-Qaidam continent. Early Paleozoic ophiolite occurrences (letters in diamonds), locations of Silurian high-pressure (HP) rocks, and the North Qaidam and Altun ultrahigh-pressure belts (NQ UHP and Al UHP, respectively) are also shown. Abbreviated early Paleozoic Qilian ophiolites (letters in diamond symbols): A—Aoyougou; Y—Yushigou; D—Dongcaohe; J—Jiugequan; B—Biandukou; L—Laohushan. Abbreviated sutures: AKM-D—Anyimaqen-Kunlun-Muztagh-Dabie Shan; J—Jinsha; NQG—North Qinling; NQN—North Qilian; SQN—South Qilian; TSYS—Tian Shan–Ying Shan.**
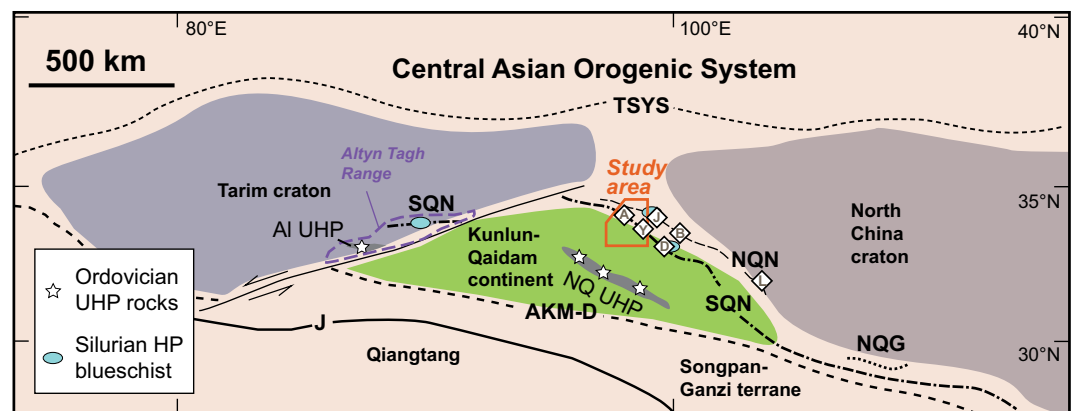
blages, ophiolites, and low- to high-grade metamorphic rocks are variably exposed throughout northern Tibet. Several important first-order problems regarding the development of the Qilian orogen remain unresolved (Fig. 3; Table 1). (1) How many arcs and what type of arcs (i.e., oceanic or continental) were involved in orogeny (e.g., Xiao et al., 2009; Yang et al., 2009, 2012; Song et al., 2013)? (2) Was the subduction polarity north- and/or south-dipping (e.g., Sobel and Arnaud, 1999; Yin and Harrison, 2000; Gehrels et al., 2003a, 2003b; Yin et al., 2007b; Xiao et al., 2009; Yang et al., 2009, 2012; Yan et al., 2010; Gehrels et al., 2011; Song et al., 2013)? (3) When did continental collision first initiate (e.g., Liu et al., 2006; Qi, 2003; Tung et al., 2007; Lin et al., 2010)? (4) When was the final closure of the Qilian Ocean (i.e., Devonian or Silurian; e.g., Xiao et al., 2009; Yang et al., 2012)?

### Mesozoic Extension

Mesozoic regional extension affected much of northern Tibet, including the Altyn Tagh Range, Qaidam Basin, Qilian Shan–Nan Shan, and Hexi Corridor, from southwest to northeast, respectively (Fig. 1; Huo and Tan, 1995; Vincent and Allen, 1999; Chen et al., 2003; Yin et al., 2008a, 2008b). This extension was expressed by the development of extensive Jurassic and Cretaceous extensional and transtensional basins (Vincent and Allen, 1999; Chen et al., 2003; Yin et al., 2008a, 2008b; Zuza et al., 2016). The magnitude of extension is unconstrained because of the limited exposure of Mesozoic rocks and structures. However, early Paleozoic muscovite $^{40}Ar/^{39}Ar$ ages from the footwall of Cretaceous normal faults indicate that the magnitude of Cretaceous normal faulting was relatively small (<10 km; Chen et al., 2003).

### Cenozoic Deformation

Cenozoic shortening in northern Tibet is accommodated across the Qilian Shan–Nan Shan and North Qaidam thrust belts (Yin et al., 2007a, 2008a, 2008b; Zuza et al., 2016), to the north and south, respectively (Fig. 1). The thrust belts are thick skinned, and most thrusts are northeast-dipping, with the prominent exception of the southwest-dipping North Qilian Shan frontal thrust system (Fig. 1; Zheng et al., 2010; Zuza et al., 2016). Cenozoic deformation juxtaposed Proterozoic–Paleozoic basement rocks against late Paleozoic through Cenozoic strata (Gaudemer et al., 1995; Meyer et al., 1998; Wang and Burchfiel, 2004; Yin et al., 2007a, 2007b; Zheng et al., 2010).

A detailed discussion of existing Cenozoic shortening estimates across the Qaidam Basin, North Qaidam, and Qilian Shan–Nan Shan thrust belts, and the implications for plateau construction mechanisms were presented in Zuza et al. (2016). Synthesized estimates suggest that northern Tibet accommodated a minimum of 250–350 km of Cenozoic north-south shortening (Yin et al., 2007a, 2008a, 2008b; Zuza et al., 2016), with higher shortening strain (>50% strain) focused along the northern margin of the thrust belt compared to the thrust-belt interior (i.e., >30%–35% strain; Zuza et al., 2016). Here, we present additional shortening estimates from the thrust belt interior based on our new geologic mapping and cross sections. Because fault offset and slip rate along the western termination of the Haiyuan fault appear to
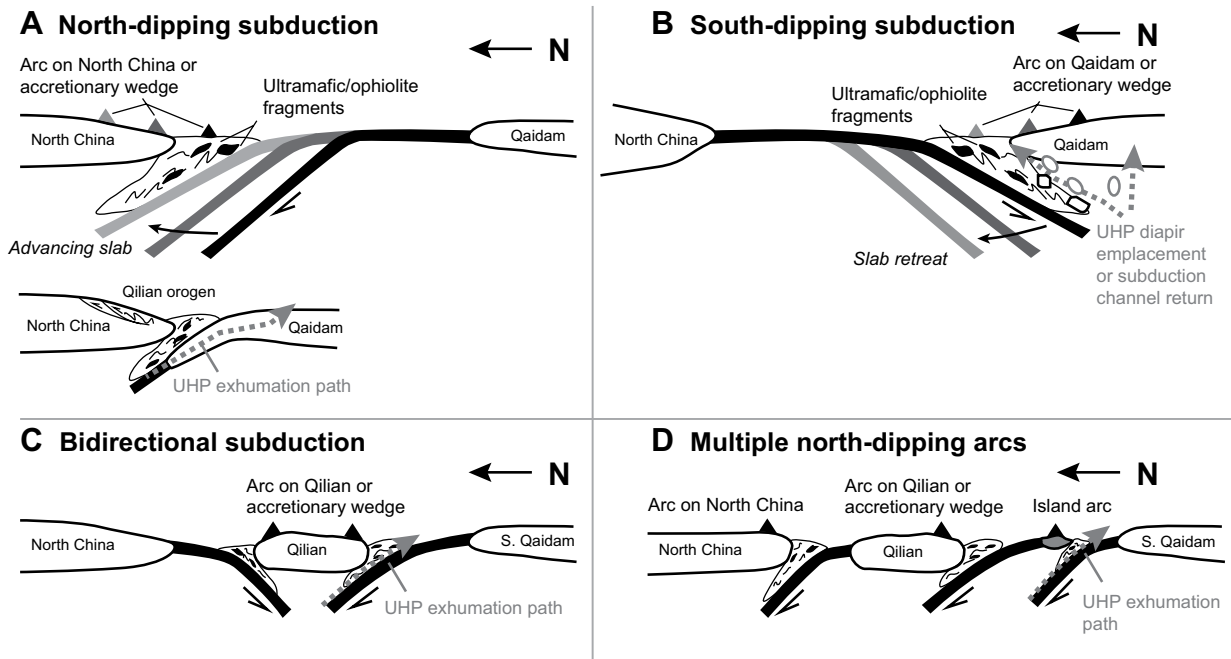


Figure 3. Major tectonic models proposed for the development of the early Paleozoic Qilian orogen, including the implied ultrahigh-pressure (UHP) rock exhumation paths. (A) The north-dipping subduction model requires the Qilian arc to have been constructed primarily on the North China craton with northward-migrating arc magmatism caused by subduction-slab shallowing. (B) The south-dipping subduction model requires the Qilian arc to develop along the northern margin of the Qaidam continent, with northward arc migration caused by slab steepening and rollback. (C) The bidirectional subduction model requires the Qilian arcs to develop within the Qilian microcontinent. In this scenario, two suture zones should have developed, including separate collisional orogens and forearc basins. (D) The multiple north-dipping arc model requires several arc belts, suture zones, and collisional events. The arcs may have developed on the North China craton, Qilian microcontinent (or North Qaidam), accretionary wedges, and/or oceanic lithosphere. See text and Table 1 for further discussion and references.

TABLE 1. TECTONIC MODEL PREDICTIONS FOR THE EARLY PALEOZOIC QILIAN ARC AND OROGEN

| Predictions | | | | | | |
|---|---|---|---|---|---|---|
| Spatial relationship between arc plutons and suture(s) | Arc basement | Explanation for wide and complex mélange/ophiolite belt | Northward younging of magmatism | Dextral shear zone in Qaidam at ca. 475 Ma | Explanation for North Qaidam UHP rocks | Key references |
| North-dipping subduction | | | | | | |
| Plutons north of suture | North China craton or accretionary material | Paleozoic continental deformation and Mesozoic/Cenozoic reorganization of main suture | Subduction-slab shallowing | Unrelated to Qilian arc | Subduction of Qaidam continent and intra-continental channel flow exhumation during collision | Yang et al. (2001), Song et al. (2005, 2006, 2013, 2014) |
| South-dipping subduction | | | | | | |
| Plutons south of main suture | Qaidam continent or accretionary material | Paleozoic continental deformation and Mesozoic/Cenozoic reorganization of main suture | Subduction-slab steepening and slab rollback | Intra-arc strike-slip fault | Subduction of North China craton and return along subduction channel or via diapirs | Sobel and Arnaud (1999), Gehrels et al. (2003a, 2003b), Yin et al. (2007a) |
| Bidirectional subduction | | | | | | |
| Sutures in surrounding arc belts to the north and south | Qilian microcontinent or oceanic lithosphere | Two Paleozoic collisions and subsequent later modification | Earlier initiation of southern north-dipping subduction | Intra-arc strike-slip fault and/or collision related | Subduction of southern Qaidam and channel flow exhumation along North Qaidam suture | Xiao et al. (2009)* |
| Multiple north-dipping arcs | | | | | | |
| Distinct belts of sutures and plutons | Microcontinent and/or oceanic lithosphere | Several Paleozoic collisions and subsequent modification | Arcs initiated and progressed at various times | Intra-arc strike-slip fault and/or collision related | Variable subduction of microcontinents and cratons | Li et al. (1978), Hsü et al. (1995), Yin and Nie (1996), Yang et al. (2002), Yin and Harrison (2000) |

*Note:* These hypotheses and predictions are based on the assumption that Mesozoic and Cenozoic deformation are constrained and restored. UHP—ultrahigh-pressure.
*This work also envisions multiple oceanic arcs, but it is most concerned with bidirectional subduction beneath the Qaidam microcontinent.

be negligible (≤15 km; Zuza and Yin, 2016; this study), east-west translation and modification of the pre-Mesozoic geology were minimal. However, the left-slip Altyn Tagh fault truncates the surface traces of the Qilian orogen and suture (Fig. 2). Paleozoic UHP and suture zone rocks in the Altyn Tagh Range (Altun UHP belt; e.g., Yang et al., 2006) may correlate with those in North Qaidam and the Qilian Shan, which indicates ~450 km of left-lateral offset on the Altyn Tagh fault (Figs. 1 and 2; Sobel and Arnaud, 1999; Yang et al., 2001; Zhang et al., 2001; Cowgill et al., 2003).

**Geology of the Early Paleozoic Qilian Orogen**

The primary tectonic domains of the early Paleozoic Qilian orogen include, from north to south (Fig. 2), the (1) southern margin of the North China craton, including Neoproterozoic passive-margin strata, (2) the North Qilian suture, which is a belt of discontinuously exposed ophiolitic material that locally experienced blueschist-facies metamorphism, (3) the South Qilian suture, which is a belt of variably exposed ophiolite fragments that do not record high-grade metamorphism, (4) a wide zone of arc volcanic and plutonic rocks associated with the Qilian arc, which respectively overlie and intrude amphibolite-grade metamorphic rocks, (5) the North Qaidam UHP metamorphic belt, with associated ophiolite complex, and (6) the Kunlun-Qaidam Precambrian con-

tinent (e.g., Yin et al., 2007b; Xiao et al., 2009; Song et al., 2013, 2014; Wu et al., 2017a, and references therein).

*Qilian Shan and North China*

The southern margin of the North China craton consists of Paleoproterozoic (ca. 2.3–1.8 Ga) basement with a Mesoproterozoic cover sequence (Xiu et al., 2002; Tung et al., 2007; Gong et al., 2011; Wan et al., 2013). Some of the oldest intrusions have ca. 2.3 Ga magmatic zircon ages and ca. 2.85 Ga zircon Hf model ages, which are similar to ages in the Kunlun-Qaidam continent, and thus the two continents may have shared a common Proterozoic history (Dan et al., 2012). The Neoproterozoic opening of the Paleo-Asian and Qilian Oceans along the northern and southern margins of the North China craton, respectively, is evidenced by widespread passive-margin deposits and ca. 825–600 Ma bimodal volcanic and intrusive rocks (Li et al., 2005; Tseng et al., 2006, 2007; Xu et al., 2015).

The discontinuously exposed North Qilian suture zone (Fig. 2) consists of ophiolite complexes, high-pressure metamorphic rocks, including lawsonite-bearing eclogite and blueschist, volcanic arc rocks, a westward-tapering Silurian flysch basin, and dispersed Devonian molasse (e.g., Pan et al., 2004; Liu et al., 2006; Song et al., 2007, 2013; Zhang et al., 2007; Xiao et al., 2009; Lin et a., 2010; Cheng et al., 2016). Ophiolite suites along this suture zone, which consist of gabbro, pillow basalt, diabase dikes, mafic rocks, and serpentinized peridotite,

are exposed at the Jiugequan, Biandukou, and Laohushan localities (Figs. 1 and 2). Zircon ages from gabbroic rocks or diabase dikes range from ca. 510 Ma to 470 Ma, with numerous inherited zircon grains in a single sample (Xia and Song, 2010; Lin et al., 2010; Song et al., 2013). The significant zircon inheritance coupled with a depleted mantle geochemical signatures suggest that the ophiolites are supra-subduction zone–type ophiolites (e.g., Shervais, 2001; Wakabayashi et al., 2010; Xia et al., 2012).

The South Qilian suture zone (Fig. 1) consists of suites of serpentinite, altered ultramafic rocks, gabbro, pillow basalt, and mélange with marl and chert that are exposed at the Aoyougou, Yushigou, and Dongcaohe localities, from northwest to southeast, respectively (Figs. 1 and 2; e.g., Yang et al., 2002; Shi et al., 2004; Tseng et al., 2007; Song et al., 2013). Magmatic zircons from gabbroic samples yield ages ranging from 550 Ma to 490 Ma (Yang et al., 2002; Shi et al., 2004; Tseng et al., 2007; Song et al., 2013). This range of inherited zircon ages is further evidence that these ophiolites may be supra-subduction zone–type ophiolites.

Whether the North and South Qilian sutures represent separate suture zones that record separate ocean closure events is debated (e.g., Mattinson et al., 2007; Yin et al., 2007b). Both "belts" consist of sporadic outcrops of ophiolite fragments that are discontinuously exposed throughout the Qilian Shan (Yin and Harrison, 2000; Song et al., 2013), and their exposure is directly controlled by Cenozoic thrusting (e.g.,

Yin et al., 2007b). The surface traces of both suture zones are truncated to the northwest against the left-slip Altyn Tagh fault (e.g., Sobel and Arnaud, 1999; Cowgill et al., 2003). The South Qilian suture trace appears to link to the southeast with the North Qinling suture zone (Fig. 2; Yin and Nie, 1996; Tseng et al., 2009).

The Kunlun-Qaidam basement of the Qilian Shan varies from west to east (Fig. 2). In the west, Mesoproterozoic cratonal and/or passive-margin strata, intruded by ca. 960–900 Ma plutons (Gehrels et al., 2003a, 2003b; Wu et al., 2016; this study), are juxtaposed against an eclogite-bearing metamorphic complex with 775–930 Ma magmatic zircons (Tseng et al., 2006; Tung et al., 2007; Xue et al., 2009) and paragneiss with detrital zircon grains older than 880 Ma (Tung et al., 2007). In the eastern Qilian Shan, Paleoproterozoic crystalline rocks are intruded by 1190–750 Ma plutons and overlain by a Neoproterozoic–Cambrian shelf sequence (Guo et al., 1999; Wan et al., 2001, 2003; Tung et al., 2007). Volcanic arc plutons with ages of 516–440 Ma are found throughout the Qilian Shan (Qian et al., 1998; Cowgill et al., 2003; Gehrels et al., 2003a; Su et al., 2004; Wu et al., 2004, 2006, 2010; Hu et al., 2005; Liu et al., 2006; Quan et al., 2006; He et al., 2007; Tseng et al., 2009; Dang, 2011; Xia et al., 2012; Xiao et al., 2012; Xiong et al., 2012; Tung et al., 2012; Song et al., 2013; Wu et al., 2016; this study). Silurian syncollisional plutons are also dispersed throughout the Qilian Shan (e.g., the ca. 424 Ma Jinfosi pluton dated by Wu et al., 2010).

### North Qaidam Metamorphic Belt

The northwest-trending early Paleozoic North Qaidam metamorphic belt is located along the northeastern margin of Qaidam Basin (Fig. 1). The metamorphic rocks, which locally experienced UHP metamorphism, are exposed in the Lüliang Shan, Xitie Shan, and Dulan localities (Mattinson et al., 2007; Yin et al., 2007b; Menold et al., 2009, 2016; Song et al., 2014). This belt is truncated to the northwest by the Altyn Tagh fault, and it is interpreted to have been offset ~450 km left-laterally to a position in the Altyn Tagh Range (Fig. 2). Metamorphic rocks at the Jianggelesayi and Bashiwake localities of the Altyn Tagh Range are correlative to those in the North Qaidam UHP metamorphic belt (Mattinson et al., 2007; Zhang et al., 2001; Yang et al., 2001; Yin and Harrison, 2000). Both metamorphic belts consist of orthogneiss, paragneiss, and marble, with lenses of eclogite and ultramafic rocks.

Most of the metamorphic rocks in North Qaidam, including the eclogite blocks and ophiolitic rocks, have experienced regional (epidote-) amphibolite facies metamorphism (Menold et al., 2009). The eclogite-bearing rocks experienced UHP metamorphism followed by later pervasive amphibolite-grade overprinting, but the ophiolite rocks do not show signs of prior UHP metamorphism (Menold et al., 2009). Because the ophiolite and UHP rocks are tightly folded together and their contacts are often transposed, the two units were probably juxtaposed and metamorphosed to epidote-amphibolite facies in the middle to lower crust (Yin et al., 2007b; Menold et al., 2009). All of the pre-Devonian metamorphic rocks in the North Qaidam metamorphic belt are bounded by north-dipping Cenozoic thrust faults, and the exposure of the epidote-amphibolite facies and UHP metamorphic rocks was strongly controlled by Cenozoic deformation (e.g., Sobel and Arnaud, 1999; Yin et al., 2007b).

### Tectonic Models for the Qilian Orogen

Despite many uncertainties, the following events have been widely accepted about the Qilian orogen. (1) An open ocean(s) existed from at least ca. 550 Ma to 448 Ma, as evidenced by the distribution of ophiolite fragments (Smith, 2006; Xiang et al., 2007; Tseng et al., 2007; Zhang et al., 2007; Xia and Song, 2010; Song et al., 2013). (2) Arc magmatism, subduction, and collision occurred from ca. 516 Ma to ca. 400 Ma, as evidenced by the distribution of arc-related and syncollisional plutons (Qian et al., 1998; Cowgill et al., 2003; Gehrels et al., 2003a; Su et al., 2004; Wu et al., 2004, 2006, 2010; Hu et al., 2005; Liu et al., 2006; Quan et al., 2006; He et al., 2007; Tseng et al., 2009; Dang, 2011; Xia et al., 2012; Xiao et al., 2012; Xiong et al., 2012; Song et al., 2013; Wu et al., 2016). (3) Metamorphic ages across the Qilian Shan span the Ordovician: 489–440 Ma U-Pb zircon rim ages (Song et al., 2006; Zhang et al., 2007), 466–462 Ma garnet Lu-Hf and Sm-Nd ages (Cheng et al., 2016), and 490–470 Ma in situ Th-Pb monazite ages (this study). Two distinct pulses of metamorphism are observed in the North Qaidam UHP rocks: the first at 490–460 Ma, and the second at 440–420 Ma (Mattinson et al., 2006; Menold et al., 2009, 2016; Song et al., 2014). (4) High-pressure blueschist, exposed in the northern Qilian Shan, yielded cooling ages ranging from 454–442 Ma ($^{39}$Ar/$^{40}$Ar white mica ages of Liu et al., 2006) to 415–413 Ma ($^{39}$Ar/$^{40}$Ar glaucophane ages of Lin et al., 2010).

In the central Qilian Shan, the boundary between the Qilian arc complex and the North China craton is expressed as a ductile right-slip shear zone in high-grade metamorphic rocks (e.g., Qi, 2003; Xiao et al., 2009) juxtaposed against a low-grade metamorphosed mafic to ultramafic mélange, Ordovician forearc strata, and ophiolite complexes. Silurian flysch deposits have been attributed to both a back-arc (Song et al., 2013) and forearc setting (Yan et al., 2007, 2010). Based on similar lithological assemblages, the Qilian orogen and suture(s) probably connected with the Qinling orogen to the southeast (e.g., Xu et al., 2008; Tseng et al., 2009; Dong et al., 2011; Wu et al., 2016, 2017a), forming a >1000-km-long early Paleozoic orogenic belt (Fig. 2).

Numerous tectonic models have been proposed to account for the geologic observations described here (Fig. 3; Table 1). Although the work presented here is focused on the central Qilian Shan, any viable tectonic model must also account for the geologic history of the Altyn Tagh Range, Kunlun Shan, Qaidam Basin, North Qaidam, and the North China craton (Figs. 1 and 3). This includes eclogite and UHP metamorphism of continental and oceanic material exposed in the Altyn Tagh Range and North Qaidam (Sobel and Arnaud, 1999; Zhang et al., 2005; Yin et al., 2007b; Menold et al., 2009; Song et al., 2014), early Paleozoic arc-related granitoids throughout northern Tibet, Cambrian-aged ophiolites including supra-subduction zone ophiolites (Song et al., 2013), ophiolitic mélange dispersed throughout the Qilian Shan, and early Paleozoic blueschist and eclogite in the northern Qilian Shan and Altyn Tagh Range (e.g., Wu et al., 1993; Liu et al., 2006; Song et al., 2006, 2007; Zhang et al., 2007; Xiao et al., 2009; Cheng et al., 2016; Fig. 1).

End-member models for the Qilian arc and orogen (see further discussions in Mattinson et al., 2007; Yin et al., 2007b) primarily differ in the number of arcs involved, the basement upon which the arc(s) was constructed (i.e., oceanic or continental crust), subduction polarity, timing of collision, and the processes responsible for UHP metamorphism and UHP rock exhumation (Fig. 3; Table 1). For example, a single south-dipping arc would require the arc plutons to intrude the Qaidam continent to the south of the Qilian suture and accretionary wedge (e.g., Sobel and Arnaud, 1999; Gehrels et al., 2003a, 2003b), whereas northward subduction would require the arc to develop north of the main suture within the North China craton (Figs. 3A and 3B; Song et al., 2006, 2013, 2014). The north-dipping-subduction model implies that the UHP metamorphic rocks were brought to UHP depths at the subduction zone and were exhumed hundreds of kilometers to the south through the Qaidam lithosphere (Figs. 3A and 3B; e.g., Song et al., 2006, 2014). This model cannot account for early Paleozoic magmatism within the Kunlun-Qaidam continent, south of the Qilian suture trace(s).

## GEOLOGIC MAPPING OF THE CENTRAL QILIAN SHAN

This study focused on the central Qilian Shan, near the town of Yanglong (~38.5°N, ~98.5°E; Fig. 4). Mapping was conducted along the Shule, Tuo Lai, and Heihe Rivers, which drain the Tibetan Plateau to the northwest. The river valleys, at elevations of ~3500 m, are bounded by approximately NW-trending ranges with moderate relief (~0.5–1.0 km); peak elevations reach >5.5 km. The southernmost range, just north of Hala Lake, is referred to as the Shule Nan Shan (Fig. 4). The ranges to the north have an average range spacing of 30–50 km and are known as the Tuo Lai Nan Shan, Tuo Lai Shan, North Qilian Shan (e.g., Zheng et al., 2010; Zuza et al., 2016), and Yumu Shan (e.g., Tapponnier et al., 1990), from south to north, respectively (Fig. 4).

Important geologic relationships and our detrital zircon geochronology results are summarized in a simplified tectonostratigraphic column (Fig. 5) and regional-scale geologic map (Fig. 6). A more detailed lithostratigraphy for the central Qilian Shan is presented in Figure 7, along with our new geochronology data.

Geologic maps of the Shule Nan Shan, Tuo Lai Nan Shan, and Tuo Lai Shan are shown in Figures 8 and 9.

### Map Units

Stratigraphic age assignments of lithologic units are primarily from Pan et al. (2004), and the more detailed framework used in this study is based on Gansu Geological Bureau (1989), Qinghai BGMR (1991), a stratigraphic review by Zhiyi and Dean (1996), our new detrital zircon data (Fig. 5B), and our own field observations. Map units range in age from Mesoproterozoic to Quaternary and are described next in turn.

#### *Sedimentary Units*

The oldest sedimentary rocks exposed in the central Qilian Shan consist of massive-bedded limestone and dolostone, commonly metamorphosed to marble, interbedded with low-grade metamorphosed basalt and volcaniclastic layers. The carbonate and marble rocks have a distinct massive blue/gray or orange appearance. The stratigraphic thickness of this unit probably exceeds 3–7 km, but it is poorly constrained because its basal contact with the underlying metamor-

phosed basement is not observed, and internal deformation has affected the original stratigraphy (Fig. 6). The regional geologic map of Pan et al. (2004) gave this unit a Changchengian age (i.e., Paleoproterozoic or Mesoproterozoic) on the basis of an older regional geologic survey (Gansu Bureau of Geology, 1974). However, we reassign a Neoproterozoic age (labeled Z) based on recent geochronology studies on the widespread basalt (U-Pb zircon ages of 600–580 Ma; Xu et al., 2015) that is interbedded with carbonate strata (Mao et al., 1998; Xia et al., 1999).

Ordovician rocks consist of low-grade metamorphosed sandstone, siltstone, and limestone with minor volcanic and volcaniclastic rocks. A distinctive blue-gray limestone unit (labeled $O_{lm}$) appears to conformably overlie the Ordovician volcano-siliciclastic strata (labeled O). The lowest part of this unit is intruded by granitoids and intermediate to mafic dikes. All Ordovician rocks are variably deformed, and the original sedimentary relationships are obscured. Although Zhiyi and Dean (1996) stated that siltstone, volcanic rocks, and volcaniclastic rocks overlie thick limestone deposits ($O_{lm}$), this relationship was not directly observed in this mapping area and may have been obscured by
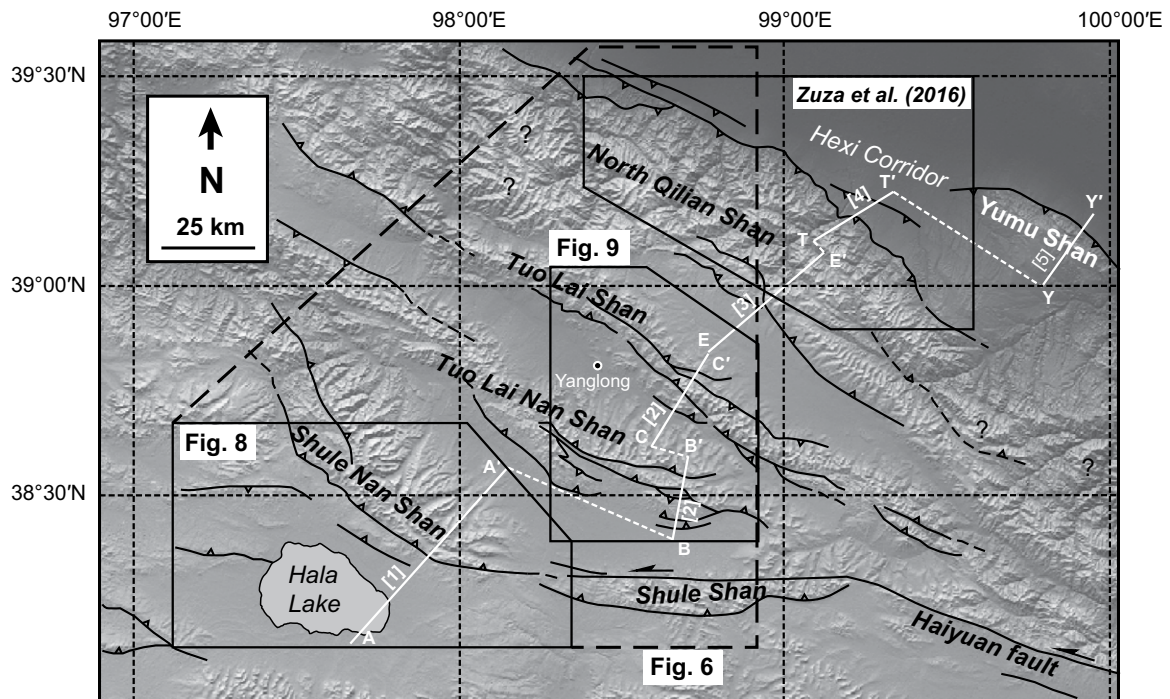


**Figure 4. Cenozoic tectonic map of northern Tibet after Yin et al. (2007a, 2008a, 2008b), Gao et al. (2013), Zuza et al. (2016), and our own observations. The underlying base map is from GeoMapApp software, available online at www.geomapapp.org (Ryan et al., 2009). Boxes indicate the locations of the composite map in Figure 6 and mapping areas in Figures 8 and 9. Also shown in white are the cross-section lines across the central Qilian Shan–Nan Shan thrust belt. Cross-section data sources: [1] map presented in Figure 8, [2] map presented in Figure 9, [3] compiled regional maps (Gansu Geological Bureau, 1989; Qinghai BGMR, 1991; Pan et al., 2004), [4] seismic-reflection analysis presented in Zuza et al. (2016), and [5] work by Tapponnier et al. (1990).**
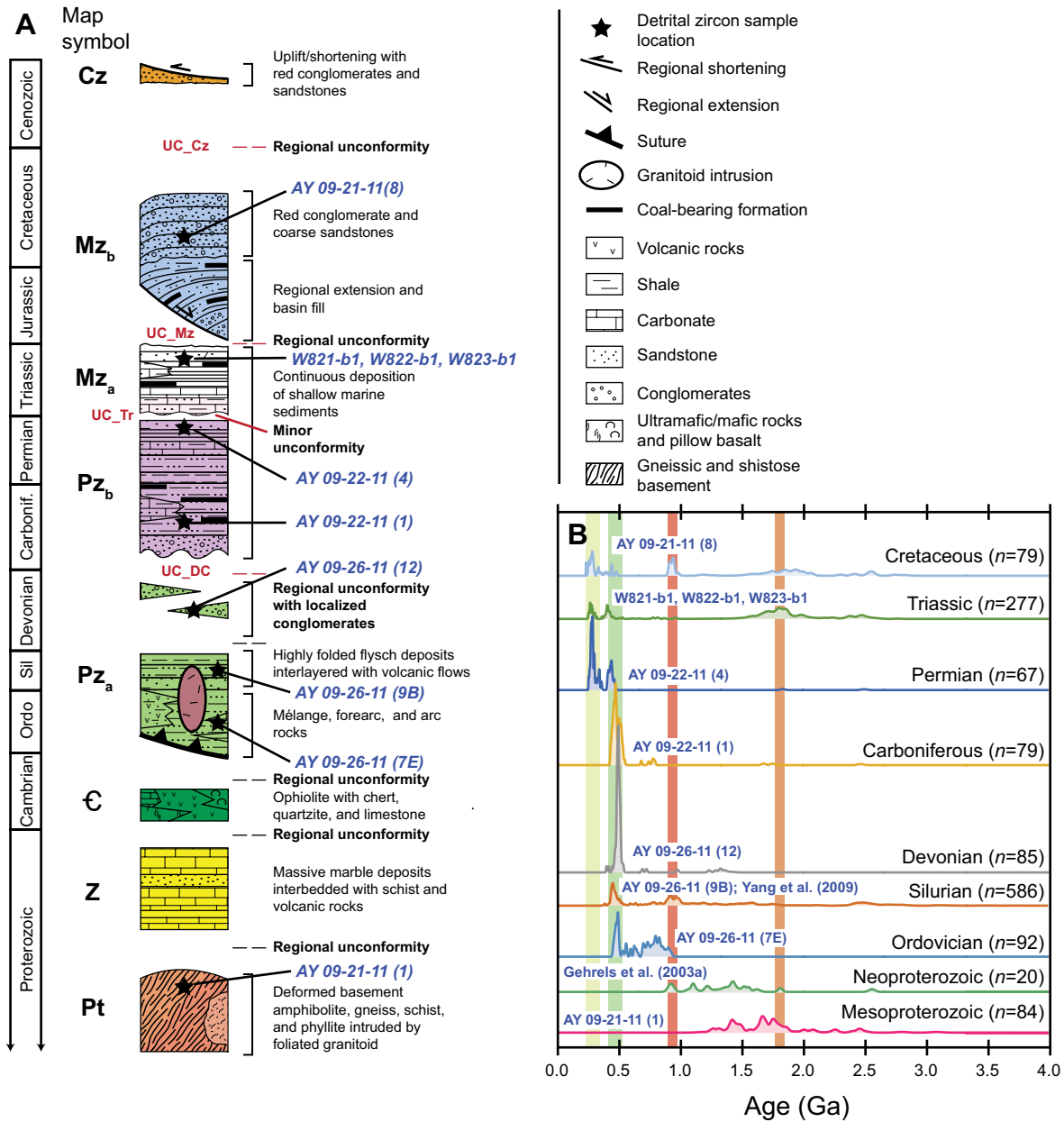
**Figure 5. (A) Tectonostratigraphy of the central Qilian Shan. Black stars show the position of U-Pb detrital zircon samples from major units. Map symbols and color scheme correspond to simplified regional units presented in the Figure 6 regional map. (B) Detrital zircon age spectra of the major tectonic units. Data are from this study, Gehrels et al. (2003a), and Yang et al. (2009).**

later deformation. Ordovician rocks probably represent a complex mélange of forearc, accretionary wedge, and foreland-basin strata (Zhiyi and Dean, 1996; Xiao et al., 2009).

Silurian rocks (labeled S) are absent from the mapping area, but they are found elsewhere in the Qilian Shan. The rocks unconformably overlie Ordovician strata and are often isoclinally folded with bedding transposed. The strata consist of minor conglomerate layers interbedded with siltstone, shale, and sandstone (Fig. 6; Yang et al., 2009; Yan et al., 2010). Conglomerate clasts and the sedimentary rocks are dominated by volcanic and granitic gneiss clasts and lithic grains, respectively. Most of the observed sections appear to be turbidite successions with interfingering conglomerate beds (Yan et al., 2010). Silurian rocks are considered to represent a flysch basin that transitions into molasse deposits (Du et al., 2003).

Devonian strata (labeled D) are mostly absent from the central Qilian Shan, but where outcrops exist to the north and south, they unconformably overlie deformed Proterozoic–early Paleozoic rocks (Fig. 6). They consist of terrestrial conglomerate, sandstone, mudstone, and minor volcanic rocks, and deposits do not exceed 300 m in thickness (Qinghai BGMR, 1991). These deposits are interpreted to represent molasse that was deposited in intermontane and/or foreland basins during Qilian orogeny (e.g., Xia et al., 2003; Yan et al., 2007). This unit is disconformably overlain by younger units.

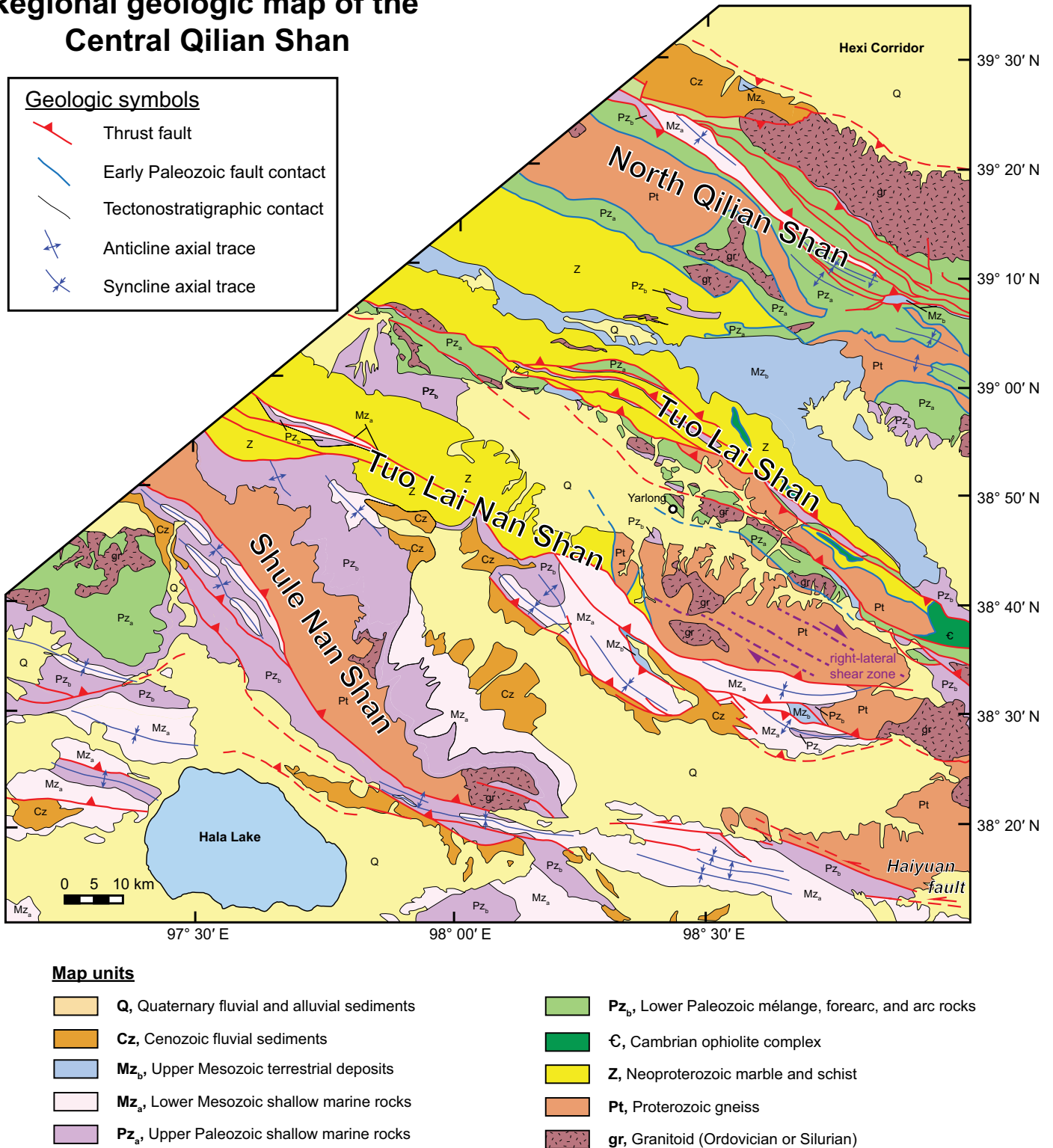# Regional geologic map of the Central Qilian Shan



**Figure 6. Regional geologic map of the central Qilian Shan based on a compilation of Gansu Geological Bureau (1989), Qinghai BGMR (1991), Pan et al. (2004), and our own geologic mapping and structural interpretations. The map units are from a simplified tectonostratigraphic scheme presented in Figure 5; location is shown in Figure 4.**
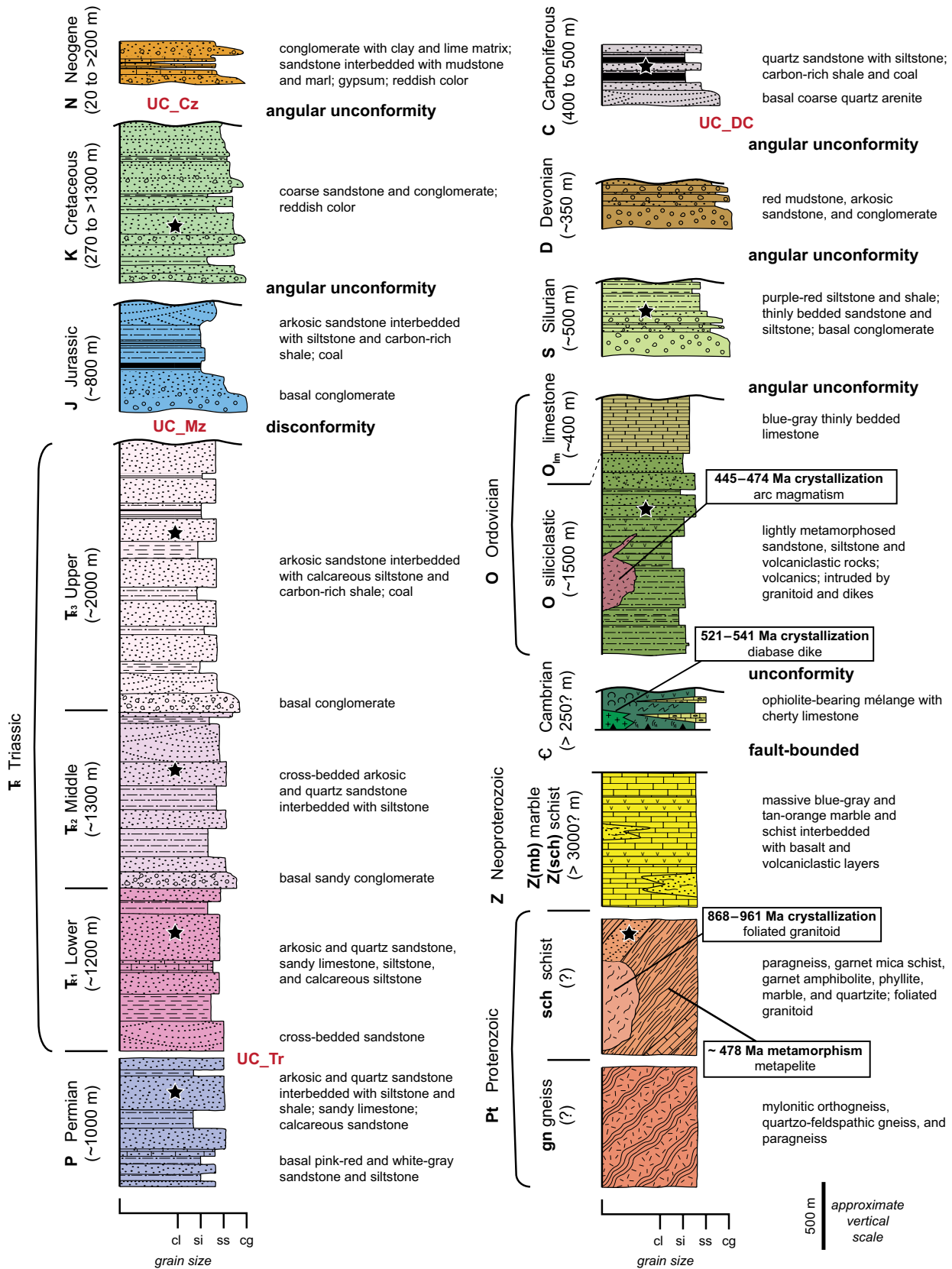
**Figure 7. Lithostratigraphy of the central Qilian Shan, specific to the Tuo Lai and Shule Shan. Age assignments are from Qinghai BGMR (1991), Pan et al. (2004), Xu et al. (2015), and our own observations. Also shown are U-Pb detrital zircon samples of major units (black stars; see Fig. 5) and geochronology results from Figures 11 and 13. Grain size abbreviations: cl—clay; si—silt; ss—sandstone; cg—conglomerate.**
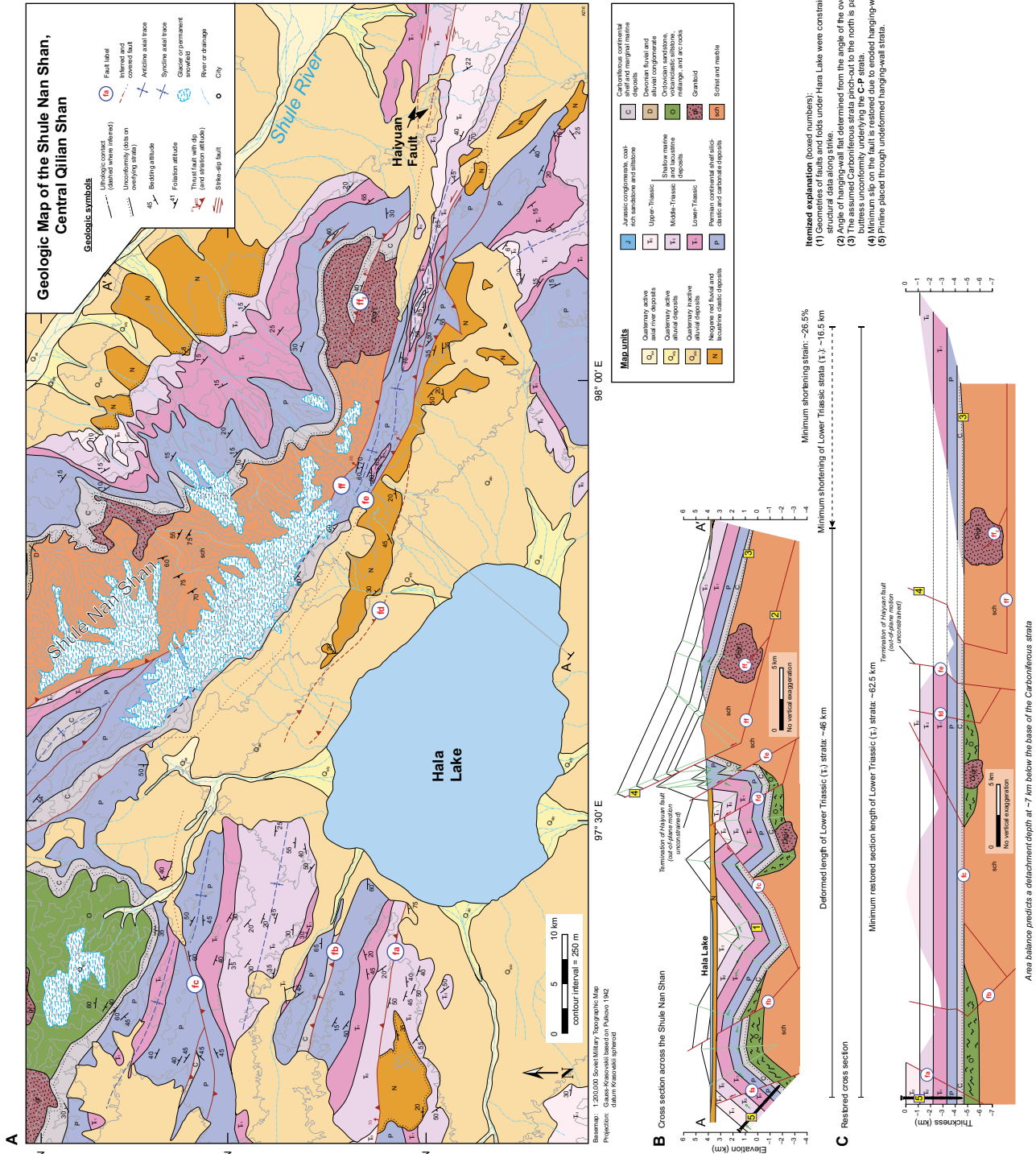
Figure 8. (A) Geologic map of the Shule Nan Shan and Hala Lake basin (for location, see Fig. 4) compiled from unpublished Chinese geologic maps, Gansu Geological Bureau (1989), Qinghai BGMR (1991), satellite-image analysis (e.g., Landsat 7 and 8, and Google Earth), and our own structural interpretations. The base map projection is from a 1:200,000 scale Soviet topographic map. (B) Cross section across the Shule Nan Shan area. (C) Restored cross section of the Shule Nan Shan area. See text for major cross-section assumptions and discussion, and see part A for cross-section line location. (Figure DR1 is a full-sized map of this figure [see footnote 1].)

**Figure 9.** (A) Geologic map of the Tuo Lai Nan Shan and Tuo Lai Shan (for location, see Fig. 4) based on unpublished Chinese geologic maps, Qinghai BGMR (1991), and our own detailed mapping. The base map is a Landsat 7 satellite image that was acquired in 2012. Also plotted is a focal mechanism for a 1993 $M_w$ = 5.9 earthquake that occurred in the Tuo Lai Nan Shan, as recalculated by Chu et al. (2009) from the Global Centroid Moment Tensor (CMT) catalogue. Stretching lineation and foliation measurements from the metamorphic basement rocks are plotted separately to the north and south of fault 4 (i.e., the fault labeled "f4"). (B) Unfolded structural data (i.e., foliation and lineation attitudes) from the metamorphic basement units that represent the pre-Carboniferous state (see GSA Data Repository [text footnote 1] for explanation). (C–E) Geologic cross sections across the Tuo Lai Shan and Tuo Lai Nan Shan in a deformed and restored states. Cross-section lines are presented in part A. (Figure DR2 is a full-sized map of this figure [see footnote 1].)

Carboniferous strata (labeled C) overlie Ordovician–Devonian rocks and other nonsedimentary units as part of a regionally extensive angular unconformity. A basal coarse-grained quartz arenite, displaying prominent cross-bedding, is overlain by quartz sandstone and interbedded siltstone, with minor carbon-rich shale and coal. The unit experienced strong internal but localized deformation along the shaley coal layers. Carboniferous rocks are 400–500 m thick. Permian strata are mapped as a single ~1-km-thick unit (labeled P; Fig. 6). The lower section consists of distinctive pink-red and white-gray coarse sandstone and interbedded siltstone. The upper section is made up of arkosic and quartz sandstone interbedded with siltstone and shale, and sandy limestone.

Conformably overlying these rocks are Triassic strata, which are thick (>4 km) and divided into the Lower ($\mathbb{R}_1$), Middle ($\mathbb{R}_2$), and Upper ($\mathbb{R}_3$) Triassic units. Lower Triassic ($\mathbb{R}_1$) rocks have a basal unit of massive cross-bedded gray sandstone overlain by arkosic and quartz sandstone, sandy limestone, siltstone, and calcareous siltstone (Fig. 6). The Middle Triassic ($\mathbb{R}_1$) strata are dominated by basal sandy conglomerate and cross-bedded arkosic and quartz sandstone with minor siltstone. Upper Triassic rocks ($\mathbb{R}_3$) consist of a basal conglomerate with overlying arkosic sandstone interbedded with calcareous siltstone, darker organic-rich shale, and distinctive coal layers (Fig. 6).

The overlying Jurassic rocks (labeled J) are generally parallel to Upper Triassic strata, although a regional disconformity between these two units exists (Yin et al., 2008b). Jurassic strata are 800 m thick and consist of a basal conglomerate overlain by arkosic sandstone interbedded with siltstone, organic-rich shale, and numerous coal beds (Fig. 6). This unit is generally restricted to valleys in the central Qilian Shan and is not cliff forming.

Cretaceous rocks (labeled K) consist of polymictic conglomerate and coarse sandstone that is reddish in color. This unit is exposed on both sides of the Tuo Lai Shan, and its absolute thickness is not known. Map-view relationships require Cretaceous strata to be >270 m thick. In the Hexi Corridor to the north, Cretaceous rocks are observed to be >3 km thick (Zhiyi and Dean, 1996; Zuza et al., 2016). They often exhibit a growth strata geometry and are interpreted to have been deposited in extensional grabens or rift basins (Yin et al., 2008b).

Cenozoic rocks are predominantly Miocene through Pliocene in age (labeled N, for Neogene; Qinghai BGMR, 1991; Zhiyi and Dean, 1996; Bovet et al., 2009), although the south-ernmost deposits may be as old as late Oligocene (e.g., Zhuang et al., 2011). They consist of red fluvial and lacustrine sediments. Conglomerate, sandstone, and mudstone have a clay, marl, or limestone matrix. Gypsum layers are prevalent. Quaternary sediments consist of alluvial, fluvial, and glaciofluvial deposits (Li and Yang, 1998; Zhao et al., 2002). They are differentiated in our mapping as active axial river deposits (labeled $Q_{ax}$), active alluvial deposits (labeled $Q_{aly}$), and inactive alluvial deposits (labeled $Q_{alo}$).

## Ophiolite Sequence Unit

An ophiolite complex, locally referred to as the Yushigou ophiolite suite (Shi et al., 2004; Hou et al., 2006; Song et al., 2013), is exposed in the northern portion of the mapping area. This complex variably consists of ophiolitic mélange and fragments of an incipient oceanic arc. The unit has been assigned a Cambrian age (labeled $\mathbb{C}$) based on reported fossils (Xiao et al., 1978) and geochronology data (Shi et al., 2004; Song et al., 2013; this study). The unit consists of ultramafic to mafic rocks, pillow basalts, and limestone and quartzite-sandstone knockers with chert. In addition, there are outcrops of massive plagioclase-pyroxene gabbro, which were mapped separately (labeled ga). There is significant deformation within the complex, and the lithologic contacts are highly sheared. Taken together, this unit represents part of the Qilian suture zone (Fig. 1), which connects with the Aoyougou ophiolite (Zhang et al., 2001; Xiang et al., 2007) to the northwest and the Dongcaohe ophiolite (Tseng et al., 2007) to the southeast (Fig. 1).

## Metamorphic Rocks

Metamorphosed basement rocks are widespread in the mapping area, and they are divided into three groups: gneiss, paraschist, and foliated granitoid. The paraschist (labeled sch) is characterized by mica ± garnet schist, quartzite, foliated garnet amphibolite, marble, and local phyllite and slate. These rocks have been interpreted as part of a Proterozoic passive margin (Gehrels et al., 2003a, 2003b). Detrital zircon ages (discussed later) confirm a maximum Mesoproterozoic age (Fig. 5B). The gneiss unit (labeled gn) is composed of quartzo-feldspathic gneiss, mylonitic orthogneiss, and paragneiss. These rocks are inferred to be Proterozoic in age based on previous geologic maps (Qinghai BGMR, 1991; Pan et al., 2004). Foliated granitoid bodies (granodiorite to quartz diorite; labeled $gr_f$) intrude both the gneiss and schist units. The foliations within in all of the metamorphic units are parallel across lithologic contacts, and all units are variably mylonitized with well-defined stretching lineations. In certain locations, both quartz and feldspar grains are ductilely deformed and recrystallized, indicating crystal plastic deformation. All of these metamorphic rocks were previously inferred to have Precambrian protolith ages (Qinghai BGMR, 1991; Gehrels et al., 2003a; Pan et al., 2004). Our geochronologic results indicate that the foliated granitoids have magmatic ages spanning 950–900 Ma (Wu et al., 2017a), providing an early Neoproterozoic minimum-age bound for the protolith of the metamorphic complex that it intrudes.

## Granitoids

Numerous early Paleozoic granitoid plutons are exposed throughout the Qilian Shan region. These plutons have been assigned ages ranging from 516 Ma to 345 Ma, and most are attributed to arc and/or syn- to postorogenic magmatism (Qinghai BGMR, 1991; Qian et al., 1998; Cowgill et al., 2003; Gehrels et al., 2003a; Su et al., 2004; Wu et al., 2004, 2006, 2010; Hu et al., 2005; Liu et al., 2006; Quan et al., 2006; Zhang et al., 2006; He et al., 2007; Tseng et al., 2009; Dang, 2011; Xia et al., 2012; Xiao et al., 2012; Xiong et al., 2012; Song et al., 2013; Wu et al., 2017a). Several large (10–50 km$^2$) and many minor (1–10 km$^2$) plutonic bodies are exposed in the mapping area. They range in composition from alkali feldspar granite to syenite to quartz monzonite. These bodies intrude the Proterozoic gneiss and schist complex and the Ordovician strata, but they are unconformably overlain by Carboniferous and younger strata. This relationship places a lower-age bound on plutonism, such that the granitoids must be older than the Carboniferous. Our geochronology data indicate that these plutons crystallized between 474 and 455 Ma. One of the plutonic bodies had a reported K-Ar age of 345 ± 17 Ma (Qinghai BGMR, 1991), but our new U-Pb zircon ages suggest a crystallization age of ca. 450 Ma for this granitoid. The units are mapped as undifferentiated granitoid (gr), except where a crystallization age has been determined, either from this study or other work. Minor dikes with compositions similar to the granitoids were also mapped.

In the Tuo Lai Shan, gabbroic plutonic rocks, diabase dikes, and basaltic volcanic rocks are found in Yushigou ophiolitic complex of the Qilian suture. U-Pb zircon ages from gabbro range from 555 Ma to 516 Ma (Shi et al., 2004; Song et al., 2013). Tholeiitic pillow basalts are also found within this mélange (Fig. 10M), and whole-rock geochemical data suggest that they are normal-type mid-ocean-ridge basalts (N-MORB; Song et al., 2013).
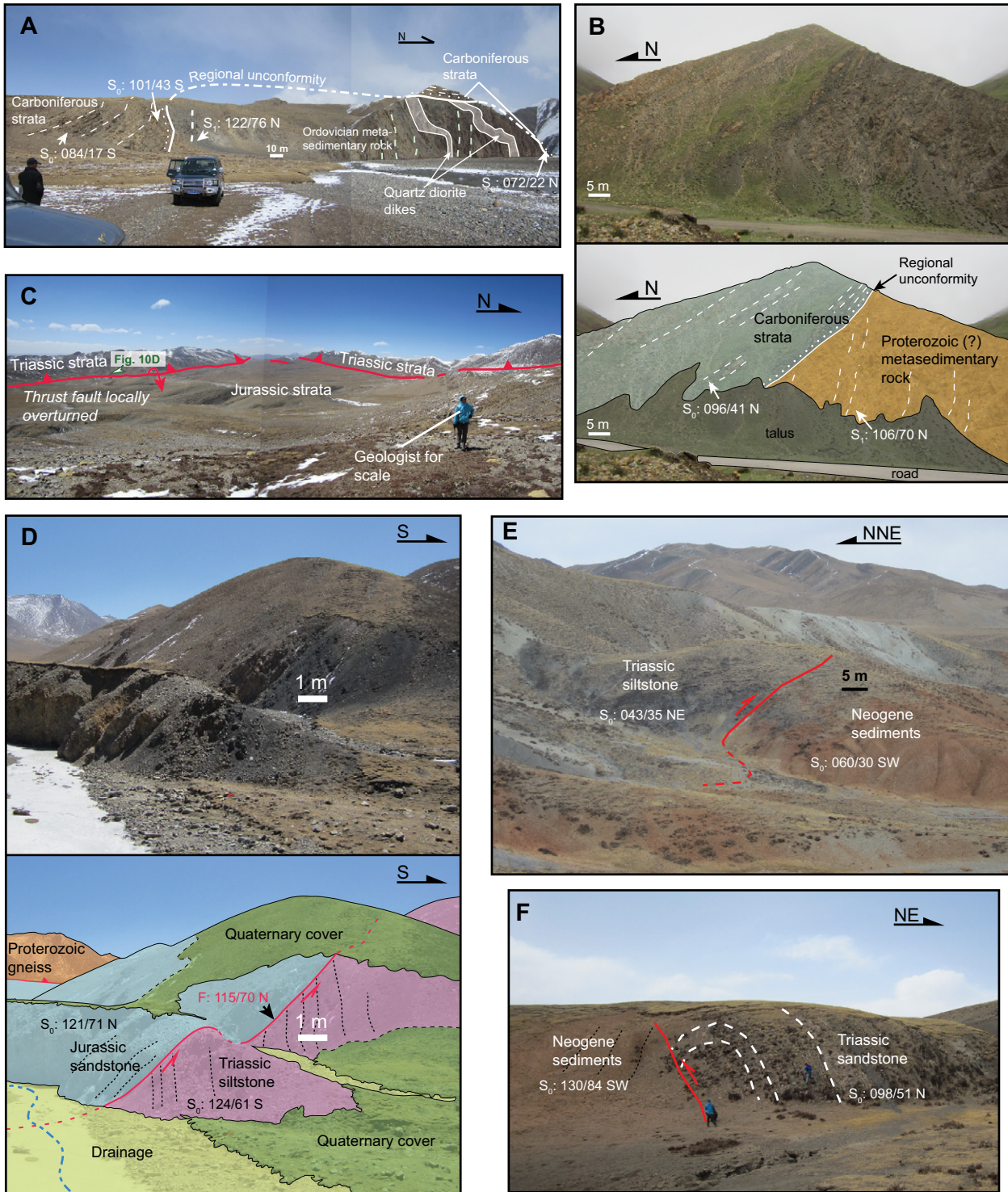
**Figure 10 (*on this and following two pages*). Field photographs from the central Qilian Shan displaying important geologic relationships discussed in text. Photograph locations are shown in Figure 9. (A) Broad anticline showing regional unconformity at the base of the Carboniferous strata, which unconformably overlie Ordovician metasedimentary rocks. (B) The regional unconformity at the base of the Carboniferous strata, which unconformably overlie Proterozoic metasedimentary rocks. (C) Triassic strata thrust over a valley of Jurassic rocks from both the north and the south. Note that the north-vergent thrust in the south of this image places Lower Triassic rocks over Jurassic strata and is overturned. See part D for a close-up view. (D) Overturned thrust fault that originally placed Lower Triassic rocks on Jurassic strata. (E–F) Thrust faults that place Triassic strata over Neogene sediments.**
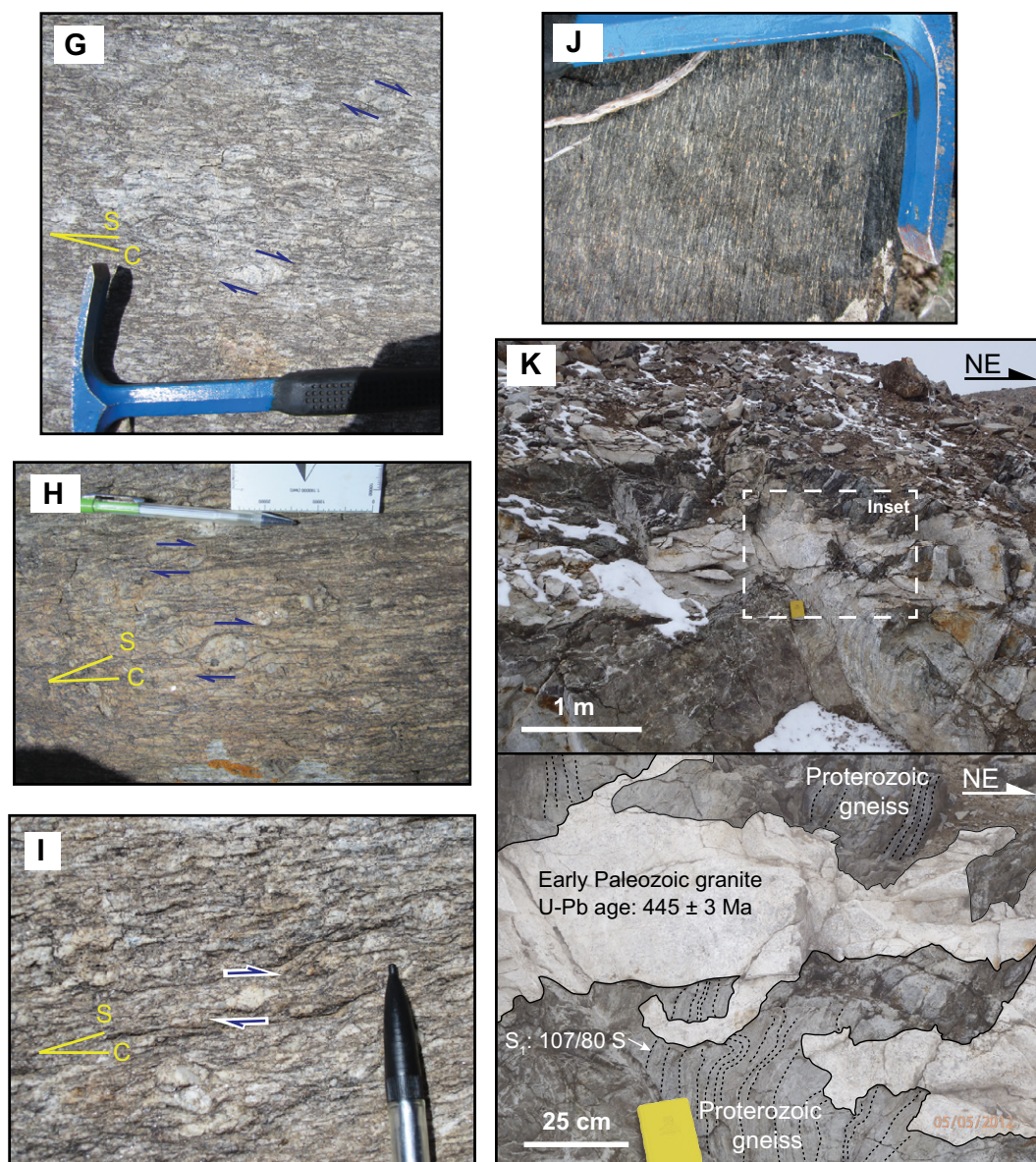
Figure 10 (*continued*). (G–I) Foliated granitoid rocks, often mylonitized, showing a right-lateral shear sense. Rocks have a near-vertical northwest-striking foliation and subhorizontal stretching lineations. (J) Strongly foliated garnet amphibolite rocks. Rocks have a near-vertical northwest-striking foliation. Note the plagioclase coronas rimming the garnet grains, and the shear sense in these rocks is also right-lateral. (K) An undeformed early Paleozoic granitoid dike crosscuts the Proterozoic gneiss. The U-Pb zircon crystallization age of the dike constrains the maximum age of metamorphism of the gneiss.

## Regional Unconformities

Four distinct Phanerozoic unconformities are recognized in the mapping area (Figs. 5–9), herein named for the unit that overlies the unconformity (Figs. 5 and 7). These unconformities are significant because (1) they represent periods of rock uplift (e.g., deformation), erosion, and/or other reasons for nondeposition, and (2) they can be used to illustrate the pre-unconformity geometries of the older rock units. For example, Carboniferous and Cretaceous unconformities in the Tuo Lai Shan both overlie Ordovician strata. This requires the Ordovician rocks to have been at or near the surface in both the Carboniferous and Cretaceous. Thus, these rocks reached the surface prior to Cenozoic deformation.

The oldest unconformity, which is also the most widespread, consists of Carboniferous strata (locally Devonian and/or Permian) overlying Proterozoic basement and Ordovician–Silurian strata (e.g., Qilian arc/orogen rocks; named UC_DC in Figs. 5 and 7). It is prevalent throughout the Shule Nan Shan, Tuo Lai Nan Shan, and Tuo Lai Shan (Figs. 10A and 10B), where Carboniferous strata overlie the Pt, Z, and O units. This unconformity is a key marker horizon in our balanced cross sections.

In one locality along the southern flank of the Tuo Lai Nan Shan, Triassic rocks ($\text{\Fontauri}_2$) unconformably overlie Carboniferous and Proterozoic rocks, including the aforementioned Carboniferous unconformity (Fig. 9; UC_Tr in Figs. 5 and 7). Triassic strata are discordant from the underlying Carboniferous strata by ~10° (Fig. 9). Just to the south, in an overturned anticline, Permian and Triassic rocks (P-$\text{\Fontauri}_3$) make up a conformable and continuous sequence. This suggests that this unconformity surface projects to at least below Permian strata in the anticline, and it cuts up section to the north to its location within the Triassic rocks as a buttress unconformity. In this scenario, a thin veneer of Carboniferous strata was deposited on top of the basement that had topography following early Paleozoic Qilian orogeny. Deposition was restricted to topographic lows. Permian through Lower Triassic rocks were deposited on this relatively flat surface, and there was either a topographic high to the north or the sediment deposition simply pinched out to the north.
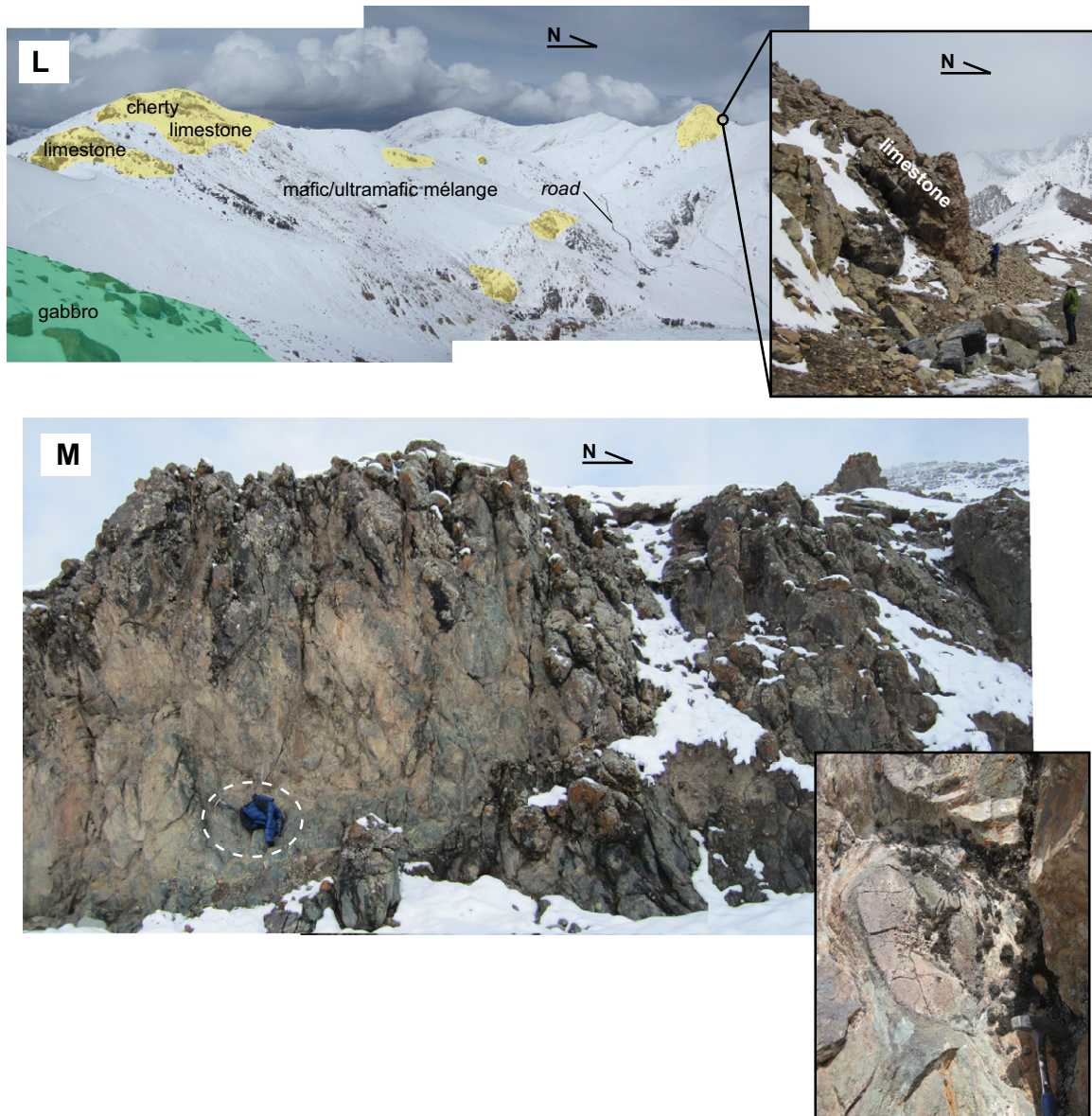
**Figure 10 (*continued*). (L) View of cherty-sandy "knockers" in mélange material. Sketched outlines highlight approximate location, size, and position of "knockers" within the mélange. Note the dirt roads for approximate scale. Inset shows outcrop view of limestone "knocker" within mélange. (M) Outcrop of pillow basalts; note the circled jacket and rock hammer for scale. Inset shows a close-up view of pillow basalt with hammer for scale.**

Middle and Upper Triassic rocks were evenly deposited over the underlying strata.

The last two unconformities—at the base of Cretaceous and Cenozoic rocks (UC_Mz and UC_Cz, respectively, in Figs. 5 and 7)—were caused by regionally extensive tectonic events. The Mesozoic unconformity was related to the initiation of widespread extension across northern Tibet (e.g., Vincent and Allen, 1999; Chen et al., 2003). This unconformity primarily consists of Jurassic and/or Cretaceous rocks angularly unconformably and disconformably overlying Paleozoic and Proterozoic strata. Along the southern flank of the Tuo Lai Shan, Cretaceous rocks were unconformably deposited on top of Ordovician rocks and Carboniferous strata. This observation provides two important constraints. First, the Ordovician and Carboniferous rocks were both at or near the surface at the time of Cretaceous deposition. Second, an event is required to have tilted the Carboniferous unconformity and Carboniferous–Permian rocks prior to the deposition in the Cretaceous. This unconformity surface is folded in a northwest-trending ~1-km-wavelength syncline (Fig. 9). Cretaceous rocks were also deposited unconformably on Proterozoic–Paleozoic rocks, along the northern flank of the same range. The Heihe River valley makes up a large Cretaceous basin that stretches ~140 km to the southeast to the city of Qilian.

Cenozoic rocks, assigned a middle Miocene age, are only exposed in the southern portions of the mapping areas (Figs. 8 and 9). They were deposited over Jurassic and Upper Triassic strata, which indicates that prior to Cenozoic deformation, these Mesozoic rocks were close to the surface. The development of this unconformity represents the initiation of Cenozoic deformation related to the Himalayan-Tibetan orogen.

# GEOCHRONOLOGY METHODS

## U-Pb Zircon Geochronology of Igneous Rocks

Zircon grains were separated by traditional methods and mounted in epoxy with standard zircons. Analyses were conducted on two separate ion microprobe instruments; analyses were performed either on the sensitive high resolution ion microprobe II (SHRIMP-II) at the Beijing SHRIMP Center, Institute of Geology, Chinese Academy of Geological Sciences (CAGS) in Beijing following the procedures of Williams (1998), or on a CAMECA IMS-270 secondary ion mass spectrometer (SIMS) at the University of California–Los Angeles (UCLA) using the analytical procedures of Quidelleur et al. (1997). Grains were first imaged with a cathode luminescence (CL) detector on a scanning electron microscope (SEM) to guide analysis and aid in age interpretation (Fig. DR3), and more detailed methodology descriptions can be found in the GSA Data Repository.[1]

Our goal in U-Pb zircon dating of the igneous samples was to determine their crystallization age. We analyzed 15–25 gains from each sample (Fig. DR3 [see footnote 1]) and examined the resulting age distribution of concordant analyses. If multiple age populations existed, the weighted mean age of the youngest population of zircon ages was interpreted as the crystallization age (Fig. 11), although we realize each plutonic body may consist of multiple intrusive pulses (e.g., Coleman et al., 2004). Distinctly older age populations were generally attributed to inheritance (Fig. 11). Younger zircon ages are less straightforward to interpret but are probably the result of Pb loss due to a younger reheating event. Additional criteria for excluding specific analyses are given along with the full isotopic data and spot locations in the GSA Data Repository (see footnote 1). Most of analyzed zircon grains are early Paleozoic in age, and we report their $^{206}Pb/^{238}U$ ages (Table 2). For samples that yielded Neoproterozoic ages, we report their $^{206}Pb/^{207}Pb$ ages (Table 2).

## U-Pb Detrital Zircon Geochronology of Sedimentary Samples

Randomly mounted detrital zircon grains from sedimentary samples were analyzed on an Agilent 7500a quadrupole–inductively coupled

plasma–mass spectrometer (Q-ICP-MS) with an ArF laser-ablation system at the Institute of Tibetan Plateau Research, Chinese Academy of Science, following the analytical procedures outlined in Xie et al. (2008). An expanded methodology description, isotopic data for analyses, and concordia diagrams for each detrital zircon sample are in the GSA Data Repository (see footnote 1). We only considered analyses that were <30% discordant or <5% reversely discordant (e.g., Gehrels et al., 2011).

## In Situ Th-Pb Monazite Geochronology

To constrain the age of metamorphism, we conducted in situ Th-Pb dating of monazite. Monazite grains appear in metasedimentary rocks near the garnet isograd (Smith and Barreiro, 1990). Monazite dating can be complicated because monazite is a relatively reactive phase that readily grows new age domains during progressive or repeated metamorphism (e.g., Foster et al., 2000; Catlos et al., 2002; Pyle and Spear, 2003; Pyle et al., 2005; Kohn et al., 2005; Rasmussen and Muhling, 2007; Williams et al., 2007; Bosse et al., 2009). In situ dating allows for determination of the relationship between monazite grains and the tectonic fabric (Harrison et al., 1995), and when monazite grains are included in porphyroblasts (e.g., garnet or staurolite), they are shielded from Pb loss and/or dissolution during retrograde metamorphism (Montel et al., 2000; Kohn et al., 2005; Gasser et al., 2012; cf. Martin et al., 2007). Thus, the ages of included grains should represent the timing of peak metamorphism (Harrison et al., 1997), assuming a single garnet-growth event. Matrix ages may or may not equal these ages (Catlos et al., 2002). Combining the interpreted monazites ages with estimated pressure-temperature (*P-T*) conditions (e.g., Spear, 1993) allows for the metamorphic evolution of the rock to be constrained.

Monazite grains were too small (~5–50 μm) to be clearly identified on an optical microscope (Fig. 12). Doubly polished thin sections were examined first with a petrographic microscope to determine the metamorphic textures. Samples with synkinematic garnet growth were targeted because the age of a monazite included in garnet should constrain the timing of garnet-in reactions during a regional shearing event (Smith and Barreiro, 1990). Thin sections were examined with a SEM in backscatter mode (Fig. 12; Scherrer et al., 2000). Monazite grains, which appear brighter than most other phases in backscatter, were observed in the matrix and included in garnet. Their identity was qualitatively confirmed with energy-dispersive X-ray spectroscopy on the SEM. Chosen monazite grains were relocated on a reflected-light

microscope and photographed at 10× and 20× to aid identification on the ion probe optics. The thin sections were cut, and target regions were mounted in epoxy and coated with gold, along with monazite standards.

Grains were dated in situ, following the procedure of Harrison et al. (1995, 1999) and Catlos et al. (2002) on the CAMECA IMS-270 SIMS at UCLA. A 10–15 nA O⁻ beam was focused to a diameter of 15–20 μm. The interelement fractionations among U, Th, and Pb during analysis were corrected by using a linear calibration curve for Pb/Th versus $ThO_2/Th$ for the monazite standards. Two monazite standards were used during two separate analytical sessions; the first session used monazite standard 44069 (thermal ionization mass spectrometry [TIMS] age of 424.9 ± 0.4 Ma and a sensitive high-resolution ion microprobe [SHRIMP] age of 426 ± 3 Ma; Aleinikoff et al., 2006), and the second used monazite standards 44069 and 554 (TIMS age of 45.3 ± 1.4 Ma; measured by M. Tatsumoto, as cited in Harrison et al., 1999). The complete listing of isotopic data is given in Table 3, and interpreted Th-Pb monazite age results are shown in Figure 13.

# GEOCHRONOLOGY SAMPLE DESCRIPTIONS AND RESULTS

## U-Pb Zircon Geochronology of Igneous Rocks

Thirteen samples were analyzed: six slightly deformed to undeformed samples from the early Paleozoic Qilian arc, two mafic dike samples from the ophiolite complex, one tonalitic dike sample that crosscuts Ordovician rocks, and four foliated granitoid samples from the metamorphic basement (Table 2). All of the samples were collected from the primary mapping area (Fig. 9), except for one that was collected from a large pluton ~300 km to the east (Fig. 1; Table 2). Concordia diagrams showing the results of single-shot zircon analyses and relative probability plots of the ages for each sample are shown in Figure 11. The interpreted crystallization ages for the igneous samples are summarized in Table 2.

All of the undeformed and some of the deformed plutonic bodies exposed throughout the central Qilian Shan (e.g., Figs. 8 and 9) were previously inferred to be early Paleozoic in age (e.g., Qinghai BGMR, 1991; Pan et al., 2004; Wu et al., 2016, 2017a). We analyzed six of these granitoid samples to constrain the timing of local magmatism (Table 2). Two samples were collected from a large undeformed alkali feldspar granite body in the Tuo Lai Nan Shan that intrudes the foliated Proterozoic gneiss (Fig. 9).
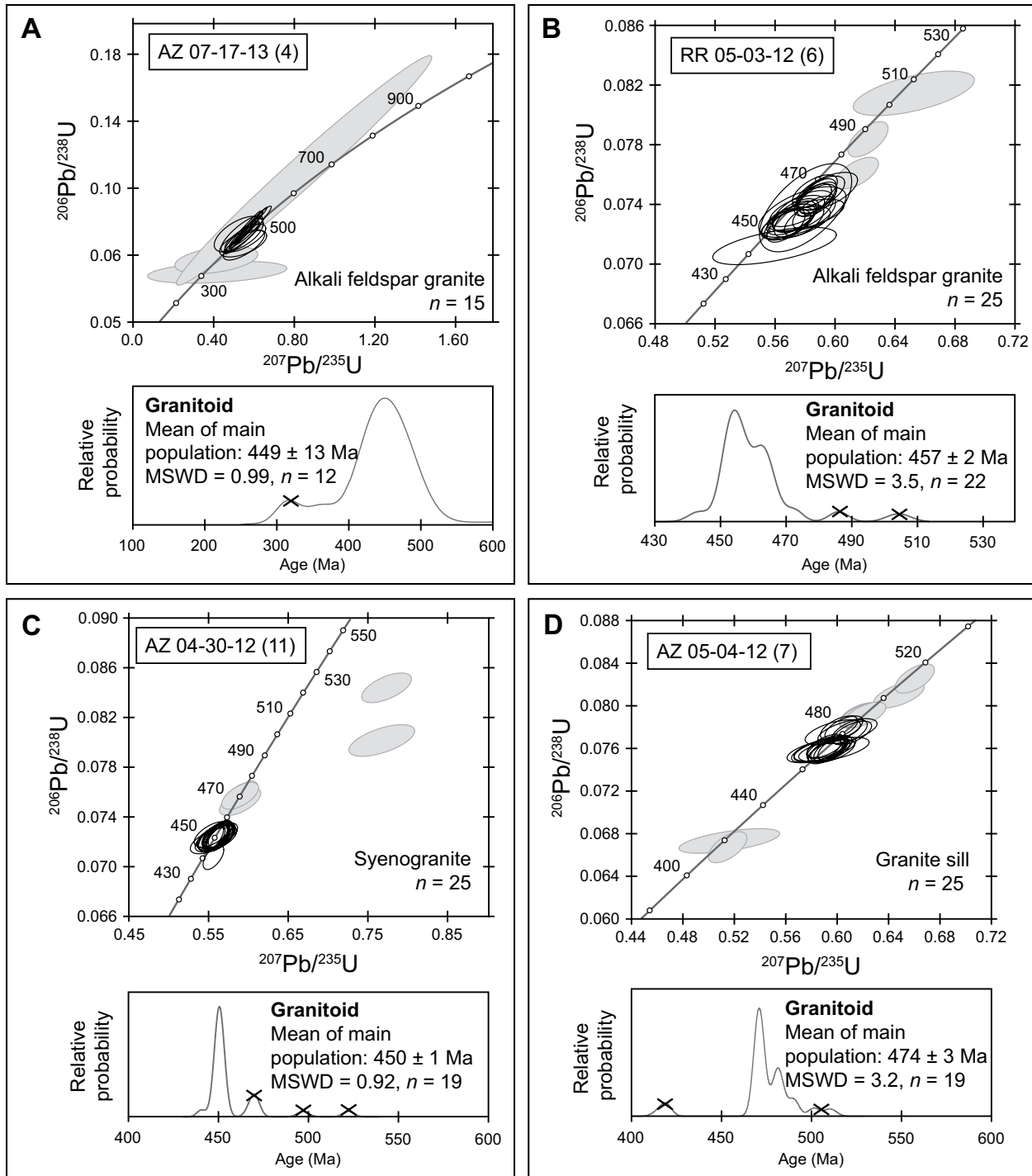
Figure 11 (*on this and following three pages*). **U-Pb concordia diagrams showing results of single-shot zircon analyses (see spots in Fig. DR3 [see text footnote 1]) and relative probability plots of zircon ages for each sample. Error ellipses are 2σ, and gray shaded ellipses show individual analyses that were excluded from weighted mean calculations. Only concordant ages are plotted in probability distributions, and crossed out peaks were not included in weighted mean calculation. All weighted mean ages are U-Pb ages (unless specified) at the 95% confidence level. See text for further discussion of rationale and Figure 9 for sample locations. Note that tonalitic dike analysis shown in Figure 11M shows a scattered spread of ages; calculated weighted mean ages of two age clusters provide age constraints on the basement that the dike intrudes. Plots were created with Isoplot 4.1 of Ludwig (2003). MSWD—mean square of weighted deviates.**
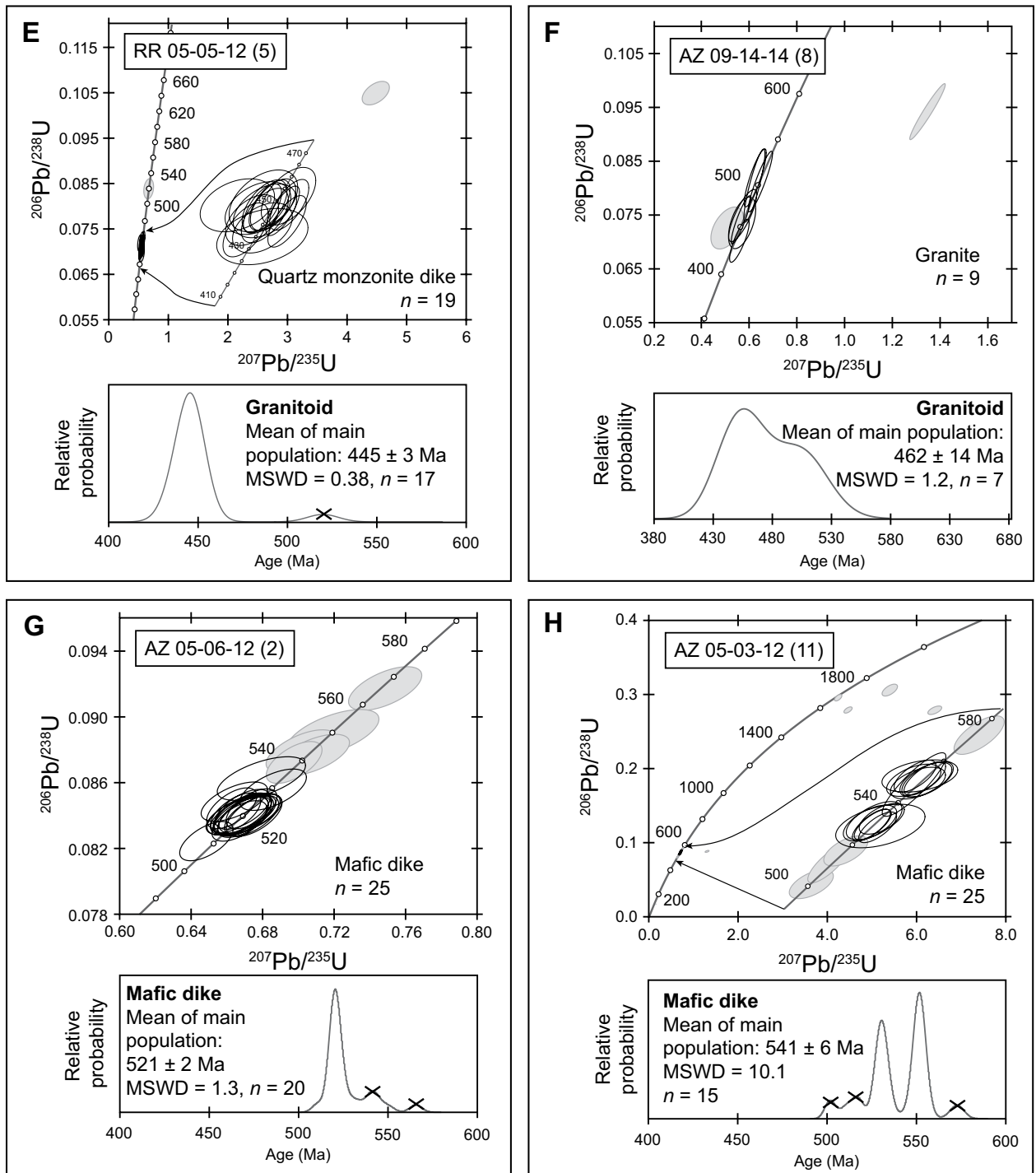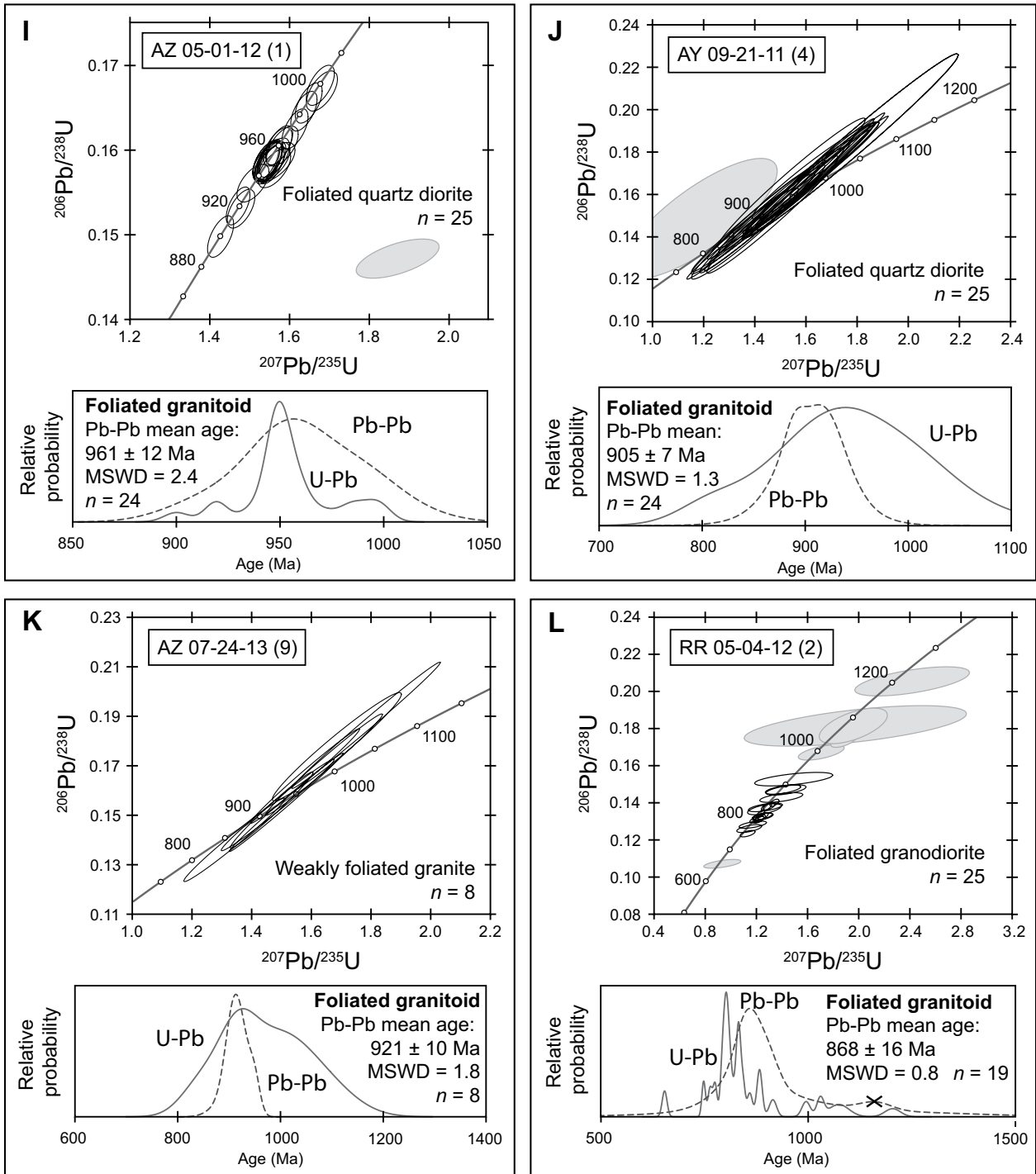
**E** RR 05-05-12 (5)

Quartz monzonite dike
*n* = 19

**Granitoid**
Mean of main
population: 445 ± 3 Ma
MSWD = 0.38, *n* = 17

**F** AZ 09-14-14 (8)

Granite
*n* = 9

**Granitoid**
Mean of main population:
462 ± 14 Ma
MSWD = 1.2, *n* = 7

**G** AZ 05-06-12 (2)

Mafic dike
*n* = 25

**Mafic dike**
Mean of main
population:
521 ± 2 Ma
MSWD = 1.3, *n* = 20

**H** AZ 05-03-12 (11)

Mafic dike
*n* = 25

**Mafic dike**
Mean of main
population: 541 ± 6 Ma
MSWD = 10.1
*n* = 15

Figure 11 (*continued*).

Figure 11 (*continued*).

**Figure 11 (*continued*).**

Sample AZ 07-17-13 (4) was collected on the southern flank of that range. Fifteen zircons were analyzed, and U-Pb ages range from 314 Ma to 680 Ma (Fig. 11A). The weighted average of 12 concordant analyses is 449 ± 13 Ma (mean square of weighted deviates [MSWD] = 0.99). The other analyses were excluded because of discordance or low radiogenic Pb. Sample RR 05-03-12 (6) was collected ~6.5 km northeast of the previous sample. Twenty-five grains were analyzed, yielding ages that range from 451 Ma to 510 Ma (Fig. 11B). Twenty-two grains define the youngest age population, and the weighted mean of these ages is 457 ± 2 Ma (MSWD = 3.5). This same plutonic body was previously

assigned a K-Ar age of 345 ± 17 Ma on a regional 1:200,000 scale geologic map (Qinghai BGMR, 1991).

Sample AZ 04-30-12 (11) was from an undeformed syenogranite located along the northeastern bank of the Tuo Lai River in the Tuo Lai Shan (Fig. 9). The pluton intrudes the Proterozoic metamorphic unit, including a strongly foliated granitoid, and it is unconformably overlain by Carboniferous strata. Ordovician metasedimentary rocks are thrust over the pluton ~500 m to the northeast of the sample location. Twenty-five zircons were analyzed yielding 22 concordant ages that range from 441 Ma to 522 Ma (Fig. 11C). The four older grains are

interpreted to be inherited, and the weighted mean of the younger population of 19 analyses is 450 ± 1 Ma (MSWD = 0.92).

Sample AZ 05-04-12 (7) was part of a granite sill that intrudes the medium- to low-grade metamorphosed unit in the Tuo Lai Shan (Fig. 9). Twenty-five grains were analyzed, and all yielded concordant ages ranging 420 Ma to 511 Ma (Fig. 11D). Two ages are distinctly younger (ca. 418 Ma), which may have resulted from Pb loss during younger metamorphism, and one population of ages is distinctly older due to older zircon-grain inheritance. The weighted mean of the average population of 19 ages is 474 ± 3 (MSWD = 3.4), which we interpret as the best estimate of a crystallization age. Sample RR 05-05-12 (5) was from a NE-SW–oriented undeformed quartz monzonite dike (Fig. 9) that crosscuts the foliations of a Proterozoic gneiss (Fig. 10K). We analyzed 19 zircons; 18 analyses gave concordant U-Pb ages that range from 435 Ma to 520 Ma (Fig. 11E). The oldest grains are interpreted to be inherited. The youngest population of 17 analyses yielded a weighted mean age of 445 ± 3 Ma (MSWD = 0.38), which is interpreted as the crystallization age of this granite dike.

Sample AZ 09-14-14 (8) was collected from a granite pluton located ~300 km to the east of the main mapping area (Fig. 1). The large pluton is exposed in a restraining bend of the left-slip Haiyuan fault. Nine grains were analyzed; one was normally discordant, and one was reversely discordant (Fig. 11F). The remaining seven grains yielded concordant ages that range from 438 Ma to 508 Ma. The weighted mean age of these concordant ages is 462 ± 14 Ma (MSWD = 1.2).

We analyzed 25 zircons from two medium-grained diabase bodies that intrude the internally deformed ophiolite complex: AZ 05-06-12 (2) and AZ 05-03-12 (11). Sample AZ 05-06-12 (2) yielded 25 concordant ages that range from

TABLE 2. SUMMARY OF ZIRCON GEOCHRONOLOGY RESULTS

| Sample | Rock type | Latitude (°N) | Longitude (°E) | Elevation (m) | Interpreted age (Ma) | MSWD | *n* |
|---|---|---|---|---|---|---|---|
| RR 05-05-12 (5) | Quartz monzonite dike | 38°34.698′ | 98°31.760′ | 4584 | 445 ± 3 | 0.38 | 17 out of 19 |
| AZ 07-17-13 (4) | Alkali feldspar granite | 38°28.546′ | 98°49.882′ | 4290 | 449 ± 13 | 0.99 | 12 out of 15 |
| AZ 04-30-12 (11) | Syenogranite | 38°34.473′ | 98°58.035′ | 3911 | 450 ± 1 | 0.92 | 19 out of 25 |
| RR 05-03-12 (6) | Alkali feldspar granite | 38°29.415′ | 98°54.218′ | 3982 | 457 ± 2 | 3.5 | 22 out of 25 |
| AZ 09-14-14 (8)* | Granite | 37°37.658′ | 101°49.904′ | 3198 | 462 ± 14 | 1.2 | 7 out of 9 |
| AZ 05-04-12 (7) | Granite | 38°41.752′ | 98°45.627′ | 3850 | 474 ± 3 | 3.2 | 19 out of 25 |
| AZ 05-06-12 (2) | Diabase dike | 38°36.800′ | 98°58.486′ | 4509 | 521 ± 2 | 1.3 | 20 out of 25 |
| AZ 05-03-12 (11) | Diabase dike | 38°36.640′ | 98°59.398′ | 4442 | 541 ± 6 | 10.1 | 15 out of 25 |
| RR 05-04-12 (2) | Foliated granitoid | 38°32.708′ | 99°00.082′ | 4060 | 868 ± 16[†] | 0.79 | 19 out of 25 |
| AY 09-21-11 (4) | Foliated granitoid | 38°41.418′ | 98°37.762′ | 3551 | 905 ± 7[†] | 1.3 | 24 out of 25 |
| AZ 04-30-12 (4)[§] | Tonalitic dike | 38°33.522′ | 98°55.447′ | 3778 | 912 ± 21[†] | 0.053 | 3 out of 16 |
| AZ 07-24-13 (9) | Weakly foliated granitoid | 38°42.472′ | 98°38.763′ | 3554 | 921 ± 10[†] | 1.8 | 8 out of 8 |
| AZ 05-01-12 (1) | Foliated granitoid | 38°39.452′ | 98°41.372′ | 3624 | 961 ± 12[†] | 2.4 | 24 out of 25 |

*Note:* MSWD—mean square of weighted deviates.
*Sample collected outside of primary study area.
[†]Pb-Pb age (all others are U-Pb ages).
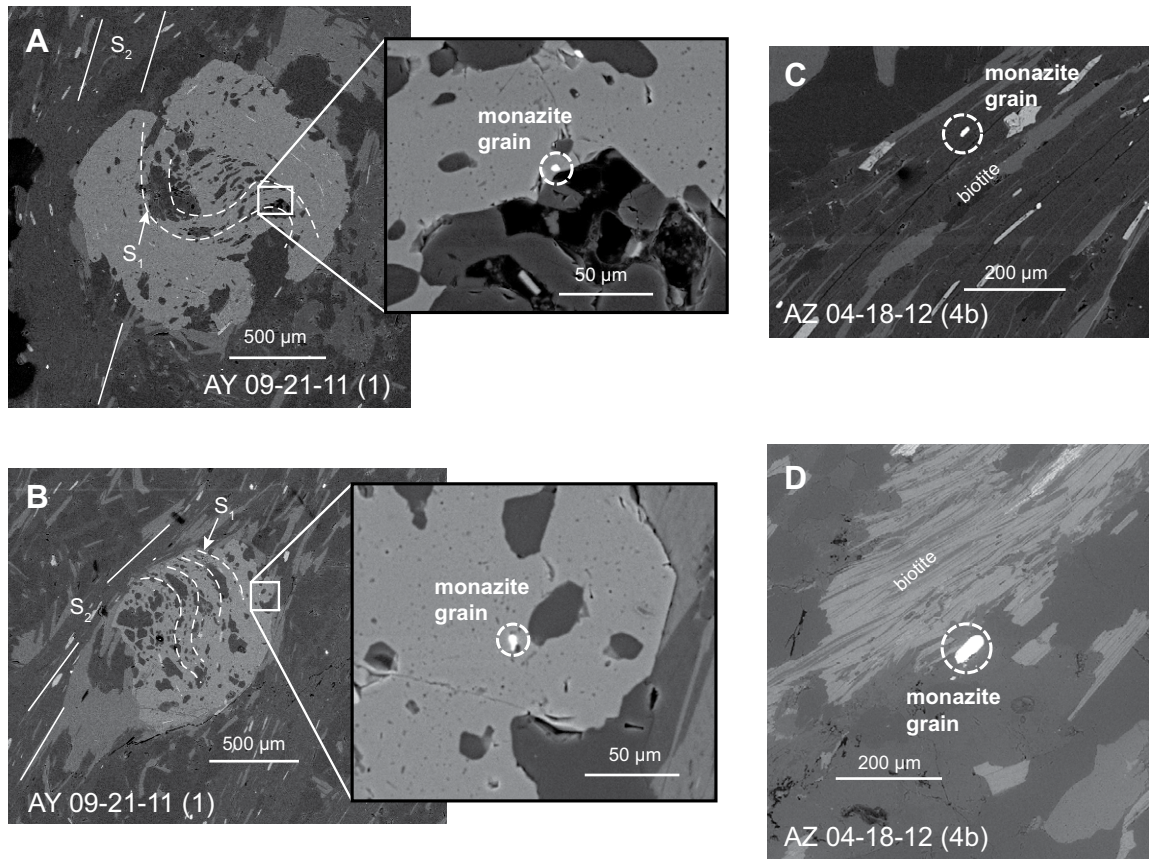[§]Range of ages picked up by intrusion; interpreted age is a well-defined age population.

**Figure 12. Scanning electron microscope (SEM) images of representative garnet and monazite grains from the garnet–mica schist samples that were targeted for in situ Th-Pb monazite dating. (A–B) Synkinematic garnet with an included monazite grain. (C–D) Matrix monazite grains. Note the size difference between matrix and included-in-garnet monazite grains.**

511 Ma to 566 Ma (Fig. 11G). We interpret the weighted mean of the youngest population of 20 analyses to best represent the crystallization age, which yields a mean age of 521 ± 2 Ma (MSWD = 1.3). Analyses of zircon grains from sample AZ 05-03-12 (11) yielded 20 concordant yet diverse ages, ranging from a U-Pb age of 501 Ma to a Pb-Pb age of ca. 1670 Ma (Fig. 11H). There are several distinct age populations and significant zircon inheritance. If we assume that the oldest age population is inherited grains, the weighted mean age of the middle population of ages ($n = 15$) may best represent the crystallization age of the diabase: 541 ± 6 Ma (MSWD = 10.1). The youngest set of ages may be the result of Pb loss, as fluid infiltration and mineral modification may have occurred within the highly deformed and altered ophiolite complex. Alternatively, these young 511–501 Ma ages may reflect later pulsed intrusion or slow cooling.

The two previously discussed samples are part of Yushigou ophiolite suite (e.g., Hou et al., 2006; Song et al., 2013), which includes tholeiitic pillow basalts (Hou et al., 2006; Song et al., 2013). The prevalence of inherited zircon ages in both intrusive samples suggests that these mafic intrusions are not related to MORB generated within the oceanic lithosphere. Zircon ages from gabbro samples in this complex yielded concordant ages ranging from 566 Ma to 530 Ma (Song et al., 2013), and similar inherited zircon ages were also observed in the Dongcaohe and Jiugequan ophiolite suites (Fig. 1; Xia and Song, 2010; Xia et al., 2012; Song et al., 2013). In light of these observations, we believe that the Yushigou ophiolite may have formed in a supra-subduction zone setting (Shervais, 2001; Wakabayashi et al., 2010), and these zircon ages may record a period of early subduction initiation (e.g., Stern, 2004). Similar conclusions have been made regarding the Jiugequan ophiolite complex that is exposed ~25 km to the north (Fig. 2; Xia and Song, 2010).

The high-grade metamorphic unit is intruded by several large foliated granitoid bodies (Fig. 9). Granitoid foliations (Figs. 10G–10I), ranging from weakly foliated to mylonitized, are parallel to foliations of the high-grade gneiss, schist, and amphibolite rocks into which they intrude. The original crystallization age of this plutonic body places a minimum age on the protolith age of the basement unit. Two samples were collected from a mylonitized granitoid (quartz diorite to granodiorite) along the southern bank of the Tuo Lai River in the Tuo Lai Nan Shan: AZ 05-01-12 (1) and AY 09-21-11 (4) (Fig. 9). The mylonitized granite has near-vertical NW-SE–striking foliations and subhorizontal stretching lineations, which are parallel to structures found throughout the Tuo Lai Nan Shan metamorphic belt (Fig. 9). Twenty-five zircons were analyzed from sample AZ 05-01-12 (1), and one was normally discordant (Fig. 11I). The remaining analyses yielded Pb-Pb ages that range from 941 Ma to 1016 Ma, with a majority of the ages clustering at ca. 960 Ma. The weighted mean Pb-Pb age of 24 grains is 961 ± 12 Ma (MSWD = 2.4). Seventeen grains were analyzed from sample AY 09-21-11 (4), and all of the ages were concordant (Fig. 11J). Individual Pb-Pb zircon ages range

TABLE 3. MONAZITE ISOTOPIC DATA FOR CENTRAL QILIAN SHAN SAMPLES

| Spot | Mz loc.* | Age (Ma) $^{208}$Pb/$^{232}$Th | 1σ | $^{206}$Pb/$^{238}$U | 1σ | $^{206}$Pb* (%) | Isotopic ratios $^{208}$Pb*/$^{232}$Th | 1σ | $^{206}$Pb*/$^{238}$U | 1σ | $^{207}$Pb*/$^{235}$U | 1σ | $^{207}$Pb*/$^{206}$Pb | 1σ | ThO$_2$/Th |
|------|----------|------|-----|------|-----|------|------|-----|------|-----|------|-----|------|-----|------|
| Sample AZ 04-18-12 (4b): 38.50647°N, 98.69933°E (4314 m) | | | | | | | | | | | | | | | |
| 16m3_1 | m | 433.9 | 20.2 | 400.2 | 41.3 | 99.4 | 0.02170 | 0.00102 | 0.00681 | 0.4822 | 0.0513 | 0.05460 | 0.000606 | 0.00681 | 2.56 |
| 21m3_14 | m | 774.5 | 126.0 | 400.9 | 79.7 | 99.1 | 0.03906 | 0.00650 | 0.01320 | 0.4894 | 0.1010 | 0.05532 | 0.000961 | 0.01320 | 1.50 |
| 22m3_13 | m | 441.4 | 16.3 | 461.7 | 44.5 | 98.7 | 0.02208 | 0.00082 | 0.00742 | 0.5602 | 0.0562 | 0.05472 | 0.000544 | 0.00742 | 2.92 |
| 24m3_19 | m | 454.4 | 20.4 | 398.7 | 39.4 | 99.1 | 0.02273 | 0.00103 | 0.00650 | 0.4858 | 0.0498 | 0.05522 | 0.000692 | 0.00650 | 2.59 |
| 25m3_15 | m | 458.9 | 19.6 | 448.4 | 46.0 | 97.7 | 0.02296 | 0.00099 | 0.00765 | 0.5572 | 0.0604 | 0.05610 | 0.001070 | 0.00765 | 2.67 |
| 26ag3_18 | g | 495.8 | 47.9 | 313.3 | 53.0 | 94.4 | 0.02483 | 0.00243 | 0.00863 | 0.3902 | 0.0689 | 0.05683 | 0.001720 | 0.00863 | 1.79 |
| 26g3_16 | g | 492.1 | 27.1 | 276.3 | 34.9 | 95.9 | 0.02464 | 0.00137 | 0.00565 | 0.3264 | 0.0430 | 0.05406 | 0.001150 | 0.00565 | 2.31 |
| Sample AY 09-21-11 (2): 38.71306°N, 98.60619°E (3514 m) | | | | | | | | | | | | | | | |
| 10g2_3 | g | 526.0 | 31.7 | 535.8 | 93.2 | 95.9 | 0.02636 | 0.00161 | 0.01570 | 0.6988 | 0.1590 | 0.05848 | 0.007710 | 0.01570 | 2.23 |
| 12g2_4 | g | 567.8 | 33.8 | 685.9 | 81.4 | 76.9 | 0.02849 | 0.00172 | 0.01400 | 0.8445 | 0.3350 | 0.05456 | 0.019400 | 0.01400 | 2.34 |
| 1am1_2 | m | 529.2 | 27.3 | 553.8 | 76.0 | 97.8 | 0.02653 | 0.00139 | 0.01280 | 0.7251 | 0.1070 | 0.05863 | 0.001810 | 0.01280 | 2.39 |
| 1m1_1 | m | 526.7 | 24.4 | 543.7 | 63.7 | 97.8 | 0.02640 | 0.00124 | 0.01070 | 0.7055 | 0.0875 | 0.05815 | 0.001190 | 0.01070 | 2.54 |
| 20g3_12 | g | 528.9 | 24.3 | 443.5 | 48.6 | 96.5 | 0.02651 | 0.00123 | 0.00807 | 0.5678 | 0.0686 | 0.05782 | 0.002330 | 0.00807 | 2.57 |
| 3m1_3 | m | 422.0 | 19.0 | 373.1 | 35.4 | 97.4 | 0.02110 | 0.00096 | 0.00581 | 0.4781 | 0.0489 | 0.05819 | 0.001670 | 0.00581 | 2.60 |
| 5g1_4 | g | 532.1 | 20.9 | 525.7 | 48.3 | 97.1 | 0.02667 | 0.00106 | 0.00814 | 0.6415 | 0.0702 | 0.05476 | 0.002710 | 0.00814 | 2.93 |
| 7m1_7 | m | 575.5 | 30.7 | 589.5 | 84.1 | 98.6 | 0.02888 | 0.00156 | 0.01430 | 0.7412 | 0.1110 | 0.05614 | 0.000734 | 0.01430 | 2.35 |
| 8m2_9 | m | 554.5 | 33.1 | 564.0 | 87.7 | 97.6 | 0.02781 | 0.00168 | 0.01480 | 0.6903 | 0.1140 | 0.05475 | 0.001500 | 0.01480 | 2.22 |
| 9m2_6 | m | 577.9 | 35.3 | 612.4 | 102 | 98.2 | 0.02900 | 0.00180 | 0.01740 | 0.7970 | 0.1400 | 0.05801 | 0.001070 | 0.01740 | 2.19 |
| *Session #1 calibration: 0.096x − 11.234 (±0.727)* | | | | | | | | | | | | | | | |
| Sample AY 09-21-11 (2): 38.71306°N, 98.60619°E (3514 m) | | | | | | | | | | | | | | | |
| 11g1_0 | g | 469.1 | 15.2 | | | 95.7 | 0.02348 | 0.000772 | | | | | | | 0.45 |
| 3m1_1 | m | 489.2 | 12.0 | | | 93.7 | 0.02450 | 0.000610 | | | | | | | 0.40 |
| 15m1_2 | m | 488.4 | 5.0 | | | 98.8 | 0.02446 | 0.000253 | | | | | | | 0.33 |
| 4m1_3 | m | 472.0 | 3.8 | | | 99.7 | 0.02363 | 0.000191 | | | | | | | 0.39 |
| 10m2_0 | m | 439.8 | 19.9 | | | 87.3 | 0.02200 | 0.001010 | | | | | | | 0.38 |
| 23m2_1 | m | 479.0 | 5.5 | | | 99.8 | 0.02398 | 0.000280 | | | | | | | 0.38 |
| *Session #2 calibration: 0.0300x + 0.19 (±0.009)* | | | | | | | | | | | | | | | |

*Monazite (Mz) location: matrix (m) or included in garnet (g).

from 884 Ma to 948 Ma, and the weighted mean age is 905 ± 7 Ma (MSWD = 1.3). Across the Tuo Lai River, 3 km to the northeast, the basement granitoid is only weakly foliated (Fig. 9). Sample AZ 09-24-13 (9) was collected from this weakly foliated granitoid (Fig. 9), and eight zircons were analyzed, yielding a range of Pb-Pb zircon ages from 891 Ma to 949 Ma (Fig. 11K).

The weighted mean age of all of the analyses is 921 ± 10 Ma (MSWD = 1.8).

A body of strongly foliated granitoid is exposed ~20 km to the east in the Tuo Lai Shan. Twenty-five zircons were analyzed from sample RR 05-04-12 (2), which was collected from this unit (Fig. 9), yielding a wide range of ages (Fig. 11L). The youngest grain has a U-Pb age

of 655 ± 6 Ma and a distinctly low Th/U ratio (0.04; Table DR1 [see footnote 1]), which may be related to multiple zircon growth episodes or later metamorphism. By excluding both this youngest age and the significantly older inherited ages (ca. 1.2–1.0 Ga), we obtained a weighted mean Pb-Pb age from 19 grains of 868 ± 16 Ma (MSWD = 0.79). These ca. 950–
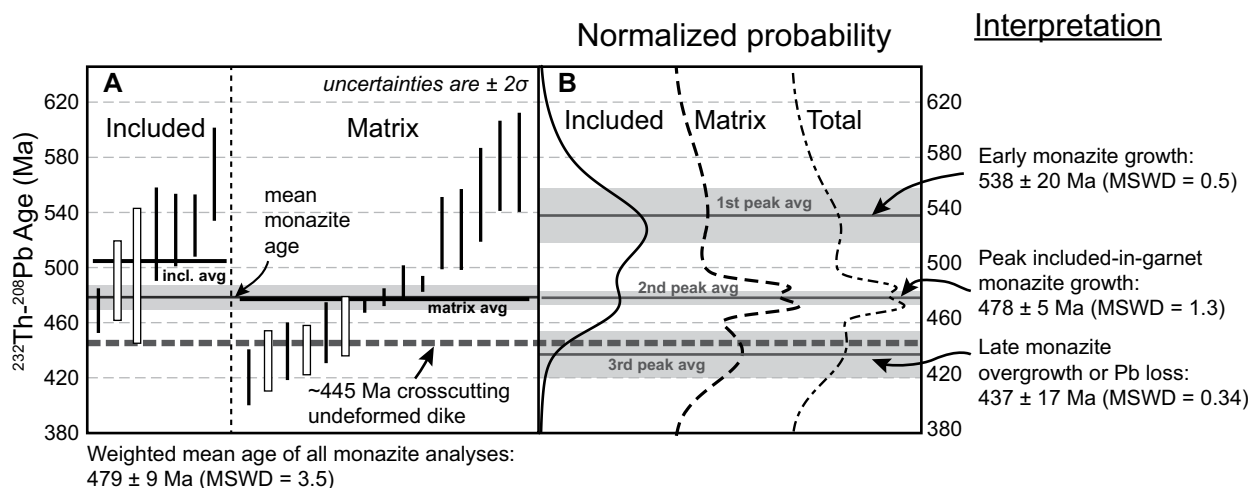


Figure 13. In situ Th-Pb monazite dating results from metapelite samples; note that one analysis is a U-Pb age, as discussed in the text. Analyses from sample AY 09-21-11 (2) are shown with solid black lines, and those from sample AZ 04-18-12 (4b) are shown with black-outlined rectangles. (A) Weighted mean ages of the entire population, the included-in-garnet grains, and the matrix grains. Also shown is the apparent U-Pb zircon crystallization age of the dike that crosscuts the foliation of the metamorphic complex. (B) Normalized probability density plot of the monazite ages of the included-in-garnet grains, matrix grains, and the total population. Interpretations of the three significant age populations are indicated. MSWD—mean square of weighted deviates.

850 Ma Neoproterozoic ages for the foliated granitoid rocks indicate that the protolith for the paragneiss and paraschist units must be older than ca. 0.85 Ga because the plutons intrude these metasedimentary rocks.

Sample AZ 04-30-12 (4) is from an E-W–trending leucocratic tonalite dike that intrudes the Ordovician metasedimentary rock (Fig. 10A). Sixteen zircons were analyzed, and only six provided concordant ages, ranging from ca. 1.9 Ga to ca. 0.9 Ga (Fig. 11M). Although no meaningful crystallization age can be determined, two concordant age clusters yielded weighted Pb-Pb mean ages of 1837 ± 18 Ma (n = 2) and 912 ± 21 Ma (n = 3), which must reflect inheritance of wall-rock zircons of the Proterozoic basement. Two best-fit discordia lines intercept concordia at ca. 0.9 Ga. The first discordia line has a lower-intercept age of 916 ± 70 Ma and may represent older inherited grains that fell off the concordia as a result of Pb loss or metamorphic mineral overgrowth at ca. 0.9 Ga, whereas the second has an upper-intercept age of 915 ± 69 Ma, which probably represents an original crystallization event at ca. 0.9 Ga with subsequent Pb loss that caused younger ages to fall of the concordia (Fig. 11M). These observations are consistent with the dike intruding through Proterozoic basement.

## U-Pb Detrital Zircon Geochronology of Sedimentary Samples

Ten detrital zircon samples were analyzed from eight different units with distinct depositional ages that range from Proterozoic to Cretaceous (Fig. 5). The results are presented in Figure 5B as normalized probability plots. Detailed stratigraphic and provenance analysis for each sample and geologic unit is in preparation and will be presented elsewhere (Y. Zhang, Oct. 2016, personal commun.). Here, we briefly discuss important age constraints provided by the detrital zircon data.

Sample AY 09-21-11 (1) is a garnet–mica schist collected along the Tuo Lai River valley from the Proterozoic schist unit (i.e., Pt[sch]; Fig. 8). The sample has prominent age peaks at 1.43 Ga, 1.7 Ga, and 1.75 Ga, and minor Paleoproterozoic age peaks. The sample possesses Archean zircon grains with concordant ages (Fig. 5B; Fig. DR4 [see footnote 1]). The three youngest grains with overlapping ages have a weighted mean age of 1272 ± 20 Ma (MSWD = 1.8), which suggests a Mesoproterozoic age for the Pt(sch) rock unit (Wu et al., 2017a).

Ordovician metasedimentary sample AY 09-26-11 (7E) shows a dominant zircon-age peak at 450–500 Ma (Fig. 5B), which is consistent with Ordovician strata being deposited in a

forearc setting. Minor Neoproterozoic zircon grains were probably shed from the Qilian-Qaidam basement that experienced widespread volcanism at this time (Tung et al., 2007; Tseng et al., 2007). Silurian strata—including sample AY 09-26-11 (9B) and data from Yang et al. (2009)—show a prominent Ordovician age peak and small populations of Proterozoic ages (Fig. 5B). The appearance of older Proterozoic grains in the Silurian samples suggests the unroofing of older basement by the time of Silurian strata deposition.

The Devonian and Carboniferous samples (i.e., AY 09-26-11 [12] and AY 09-22-11 [1]) are both dominated by 450–500 Ma age signatures, which are probably associated with the Qilian arc (Fig. 5B). The Permian and Mesozoic detrital zircon samples display minor peaks associated with early Paleozoic Qilian orogeny (i.e., 450–500 Ma) and a larger zircon age population at 300–230 Ma (Fig. 5B). This Permian–Triassic peak may either be associated with the Kunlun arc to the south (e.g., Pullen et al., 2008; Wu et al., 2016) or an arc along the northern margin of the North China craton to the north (e.g., Xiao et al., 2003; Wu et al., 2017b). The Triassic samples (and overlying Cretaceous sample) show a pronounced Paleoproterozoic zircon age peak that the Permian sample lacks (Fig. 5B), suggesting a reorganization of the source rocks or drainage systems. The Permian–Triassic transition also corresponds to an observed minor unconformity (UC_Tr in Figs. 5 and 7), which corroborates that this area was locally deformed or otherwise affected during this time.

## In Situ Th-Pb Monazite Geochronology

Two garnet–mica schist samples were selected for in situ monazite geochronology: AY 09-21-11 (2) and AZ 04-18-12 (4) (for sample locations, see Fig. 9). Both samples are composed garnet, biotite, white mica, minor chlorite, quartz, and plagioclase, with minor amounts of spinel, rutile, tourmaline, zircon, and monazite. The inclusion trail patterns in many of the garnet grains indicate synkinematic growth (Fig. 12). Our thermobarometry data indicate that although these samples are located ~25 km apart, they experienced similar overlapping amphibolite-grade *P-T* conditions. Observed matrix monazite grains are relatively large (15–50 μm in diameter), whereas grains included in garnet are very small (<15–20 μm in diameter). Many grains (~100) were identified and documented, but only 23 were analyzed, including seven grains that were included in garnet and 16 that were found in the matrix.

Both samples yielded similar and overlapping Th-Pb ages populations for both included-in-

garnet and matrix monazites (Fig. 13; Table 3). Because the individual monazite ages from both samples span similar ranges, we herein analyze and discuss all of the ages together. Although the apparent Th-Pb monazite ages can be biased by varying Th content in the unknown analyses as compared to the standard-grain analyses (Stern and Berman, 2001), the ages show no correlation between Th or U concentrations (Table 3). In addition, the U-Th-Pb systematics were concordant on a plot of $^{208}$Pb*/$^{206}$Pb* versus $^{248}$ThO/$^{254}$UO (plot not shown; e.g., Harrison et al., 1995). All of the in situ Th-Pb monazite ages range from 772 Ma to 421 Ma (Table 3). The oldest single age analysis has large uncertainties (i.e., 772 ± 131 Ma), but this same sample yielded a concordant U-Pb age of 401 ± 80 Ma (Table 3). For this analysis only, we used the U-Pb age, and therefore the modified monazite-age range of the entire population is 576 Ma to 421 Ma (Fig. 13).

Monazite age populations from both the matrix and those included in garnet overlap within error (Fig. 13A). The weighted mean ages of included-in-garnet and matrix monazite grains are 505 ± 18 Ma (MSWD = 2.1) and 477 ± 11 Ma (MSWD = 4.3), respectively. The spread of overlapping age populations suggests protracted monazite and garnet growth during the Ordovician (Fig. 13). The weighted mean age of all analyses, 479 ± 9 Ma (MSWD = 3.5; Fig. 13A), broadly constrains the timing of prograde metamorphism. However, the relatively high MSWD values suggest that either the analyzed monazites record multiple age populations, or the analytical errors are too small. Given that individual analysis uncertainties are ~5%–10%, it is probable that the monazite analyses represent multiple monazite age populations, reflecting protracted growth.

Examination of normalized probability density plots of the monazite ages—divided into groups of included-in-garnet grains, matrix grains, and the total population (Fig. 13B)—reveals three distinct age populations. The lack of a correlation between age and Th or U concentrations suggests that these differences in apparent age are not due to monazite-grain composition variation (e.g., Stern and Berman, 2001). Included-in-garnet grain ages are all older than ca. 460 Ma, and they show two age peaks at ca. 475 Ma and ca. 535 Ma. The oldest age peak correlates with a subtle age population in the matrix monazite analyses that broadly spans ca. 550–530 Ma. The weighted mean age of all monazite grain analyses in this population is 538 ± 20 Ma (MSWD = 0.5; Fig. 13B). These grains may represent the first generation of monazite growth, possibly caused by crustal thickening and/or heating associated with the

initial subduction and arc activity within the Qilian arc. The youngest age population of the included-in-garnet monazite grains correlates to a similar age population in the matrix monazite grains (Fig. 13B). This ca. 490–470 Ma signature is the largest age population of all of the analyses. The weighted mean age of this population is 478 ± 5 Ma (MSWD = 1.3; Fig. 13B). Because these monazite grains are included in garnet, they have been shielded from reactions with other phases, Pb loss, and overgrowth (e.g., DeWolf et al., 1993; Foster et al., 2000; Catlos et al., 2002; cf. Martin et al., 2007). We interpret the 478 ± 5 Ma age to best represent the age of synkinematic garnet growth and peak prograde metamorphism. The 478 ± 5 Ma age overlaps with the overall weighted mean age of all analyses, 479 ± 9 Ma (MSWD = 3.5). The included-in-garnet monazite grains were variably located across the garnet grains, and the significant zonation observed in the analyzed garnets (Fig. DR6 [see footnote 1]) implies large temperature changes during prograde growth. Thus, the monazite growth history is probably more complicated than a single population of monazite grains, but for the purpose of this study, we document prograde amphibolite-grade (see Thermobarometry section) metamorphism during the Early to Middle Ordovician.

Last, there is a minor population of younger ages from the matrix monazite grains at ca. 440 Ma (Fig. 13B). The weighted mean age of this population is 437 ± 17 Ma (MSWD = 0.34). These younger matrix monazite ages may either represent late-stage monazite overgrowth or Pb loss during fluid infiltration. This age range coincides with late-stage magmatism and/or the collision age of the Qilian orogen. An undeformed ca. 445 Ma dike crosscutting the foliation of the metamorphic complex (Figs. 10K and 13) indicates that ductile shearing and prograde metamorphism were complete by this time, at least locally. This suggests that the youngest monazite age population (i.e., ca. 437 Ma) probably does not represent prograde growth, but rather late-stage Pb loss or pluton intrusion and monazite overgrowth. Note that this youngest age population overlaps within error with some of the youngest magmatic zircon ages; for example, sample AZ 05-04-12 (7) has two zircons with a U-Pb age cluster of ca. 420 Ma.

## WHOLE-ROCK GEOCHEMISTRY

Major- and trace-element geochemical data were obtained from plutonic bodies to determine their source and tectonic setting, and from several metamorphic rock samples to constrain protoliths. Three samples were analyzed by inductively coupled plasma–optical emission spectrometry (ICP-OES) and ICP-MS at Activation Laboratories in Ontario, Canada, whereas the other samples were analyzed by X-ray fluorescence (XRF) at Pomona College, California. Complete detailed methods and full geochemical analyses can be found in the GSA Data Repository (see footnote 1).

Here, we present the geochemical evidence that supports the interpretation that both the early Paleozoic (i.e., the Qilian arc) and 0.90–0.95 Ga granitoid samples were formed in a continental arc setting, which is consistent with field and regional geologic relationships discussed earlier herein (e.g., Song et al., 2013; Wu et al., 2017a). More thorough discussion of these plutonic rocks, the diabase dike and serpentinite samples (i.e., AZ 05-05-12 [7] and AZ 05-03-12 [13]), and metamorphic rock samples (i.e., garnet amphibolite and garnet–mica schist samples) is presented in the GSA Data Repository (see footnote 1).

The undeformed early Paleozoic granitoid samples RR 05-03-12 (6), AZ 04-30-12 (11), and AZ 07-17-13 (4) are classified as alkali feldspar granite, granite (syenogranite), and alkali feldspar granite, respectively, based on their normative quartz–alkali feldspar–plagioclase mineralogy (for sample locations, see Fig. 9). Their geochemical classifications span quartz monzonite to granite based on their weight percentage of silica and alkaline elements ($SiO_2$ vs. $Na_2O+K_2O$; Table DR3 [see footnote 1]). The Neoproterozoic granitoid rocks—samples AZ 07-21-13 (7) and AY 09-21-11 (3) (for sample locations, see Fig. 9)—are classified as alkali feldspar granite and quartz diorite, respectively, based on their normative quartz–alkali feldspar–plagioclase mineralogy and granite based on their weight percentage of silica and alkaline elements ($SiO_2$ vs. $Na_2O + K_2O$; Table DR3 [see footnote 1]).

All samples are felsic ($SiO_2$ 63–75 wt%), highly peraluminous ($Al_2O_3/[Na_2O + CaO + K_2O] > 1.30$; Table DR5 [see footnote 1]), and calc-alkaline (Fig. 14A). On the granite classification diagrams of Pearce et al. (1984; cf. Snow, 2006), samples plot mostly in the volcanic arc field, with minor overlap on the syncollisional and within-plate boundaries (Fig. 14B). Rare earth element data (REE) suggest that the granitoids were sourced from a continental arc setting based on light REE enrichment and negative Ba, Nb, P, and Ti anomalies (Fig. DR5 [see footnote 1]). More rigorous geochemical analysis is not within the scope of this study, but our geochemistry data are consistent with both the early Paleozoic and Neoproterozoic granitoids being derived from a continental arc.

## THERMOBAROMETRY

To determine the metamorphic conditions of the high-grade rocks in the central Qilian Shan, thermobarometric studies were conducted on representative garnet–mica schist, garnet amphibolite, and garnet-bearing gneiss samples. These samples were either part of, or adjacent and graded into, the right-slip ductile shear zone that is exposed throughout the mapping area (Figs. 9 and 10). The goal in constraining the *P-T* histories of these samples was to address two questions: (1) is there any significant variation in peak metamorphic grade to indicate that present-day rock exposures are part of a tilted section of the Qilian orogen, and (2) what part of the Qilian orogen and arc do these rocks represent? Map relationships indicate that these metamorphic rocks were intruded by early Paleozoic arc granites (Fig. 9), and thus they should represent part of the country rock of the Qilian arc and the basement of the Kunlun-Qaidam continent.

### Methods

The metamorphic samples were first examined through petrographic microscope to characterize the representative mineral assemblages and asses the phases that grew together in equilibrium. A JEOL JXA-8200 electron microprobe at UCLA was used to make X-ray compositional maps and measure phase compositions. *P-T* estimates were determined from the chemical data using the average *P-T* mode in THERMOCALC 3.37 (Holland and Powell, 1998), with the most up-to-date, internally consistent thermodynamic data set (i.e., data set 62; Holland and Powell, 2011). Additional geothermometers provided further constraints, including the fluid-independent Ti-in-biotite calibration of Henry et al. (2005) and the hornblende-plagioclase thermometer of Holland and Blundy (1994) calibrated for silica-saturated rocks. More detailed pressure-temperature-time (*P-T-t*) analysis, including pseudosection modeling and thermochronology analyses, are in preparation and will be presented elsewhere. Our thermobarometry methods broadly followed those of Cooper et al. (2010), and a complete methodology and our analytical data, including detailed sample descriptions, X-ray garnet maps, and phase-composition data, can be found in the GSA Data Repository (see footnote 1).

### Results

Seven samples were examined from the Precambrian basement unit (Fig. 9): two garnet–mica schists (i.e., AY 09-21-11 [1A] and AZ 04-17-12 [4b]), a quartzofeldspathic gneiss
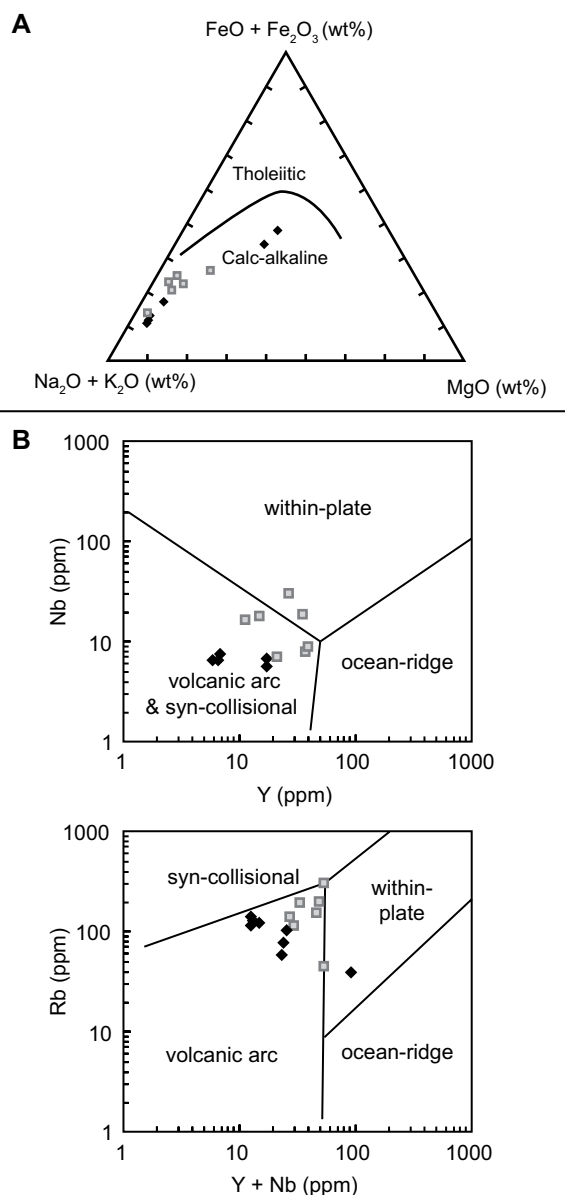
Figure 14. (A) AFM diagram for granitoid samples, where A = K₂O + Na₂O; F = Fe₂O₃ + FeO; and M = MgO. Curve for calc-alkaline and tholeiitic division is from Kuno (1968). (B) Geochemical discrimination diagrams for granites after Pearce et al. (1984). Black solid diamonds are from Zhang et al. (2006), and the other data points are from this study.

indistinguishable depths of 20–30 km, which is consistent with typical continental geothermal gradients of 20–35 °C/km. Thus, there is no evidence that these rocks represent different structural levels of the Qilian orogen, and they were probably at similar depths during prograde metamorphism (i.e., the present-day exposures do not represent any tilting of the metamorphic basement). Based on our monazite geochronology results, we interpret that the basement rocks experienced amphibolite-grade conditions in the Ordovician (Fig. 13), although their timing of exhumation is not constrained. Unmetamorphosed Carboniferous strata unconformably overlie these metamorphic units (Fig. 9), which indicates that these rocks were at or near Earth's surface prior to the Carboniferous.

## STRUCTURAL GEOLOGY

Structures dominantly trend northwest, including the strike of sedimentary units, strike of foliations within the metamorphic units, trend of the ranges, and surface trace of faults. Deformation can be categorized into three distinct regimes: (1) Cenozoic folds and faults, (2) early Paleozoic folds, faults, and unit juxtapositions, and (3) early Paleozoic ductile shearing and metamorphism. There is no direct evidence of Mesozoic deformation or normal faulting, but our field observations are consistent with earlier work that suggests that Jurassic and Cretaceous sedimentation was caused by regional extension (Vincent and Allen, 1999; Chen et al., 2003; Yin et al., 2008b), including fining-upward sequences and growth strata relationships.

We interpret deformation of Carboniferous and younger strata to be Cenozoic in age based on the following observations: (1) most observed faults and folds of Carboniferous and younger rocks merge with present-day range-bounding thrusts; (2) these faults truncate Cenozoic terrestrial deposits and Quaternary alluvium; (3) deposition of parallel shallow-marine, lacustrine, and continental shelf Carboniferous through Triassic strata was not associated with any deformational structures during these time periods; and (4) Jurassic and Cretaceous strata are extension related (e.g., Vincent and Allen, 1999; Chen et al., 2003; Yin et al., 2008a, 2008b), so contractional structures involving these rocks must be Cenozoic in age. This also implies that folding and duplication of the Carboniferous unconformity occurred in the Cenozoic. Next, we present a detailed structural analysis of each range, including juxtaposition geometries, map-view relationships, kinematic indicators, and alternative interpretations, starting with the Shule Nan Shan in the south and progressing to the ranges to the north (Fig. 4).

(i.e., RR 05-05-12 [8]), three garnet amphibolites (i.e., AY 09-21-11 [6], RR 05-05-12 [12], and AZ 07-21-13 [5]), and one garnet-epidote amphibolite gneiss (i.e., AZ 0-4-18-12 [4]). Estimated peak *P-T* conditions for the selected samples reached (epidote-)amphibolite grades, spanning pressures of 8–5 kbar and temperatures of 550–700 °C (Fig. 15; Table 4). These estimates are consistent with the observation of mostly to entirely dynamically recrystallized quartz in all of the samples. Garnets in samples AY 09-21-11 (1A), RR 05-05-12 (8), and AZ 07-21-13(5) (i.e., a metapelite, quartzofeldspathic gneiss, and garnet amphibolite, respectively) showed prograde growth zoning with decreasing Mn and increasing Fe and Mg from core to rim (Fig. DR6 [see footnote 1]), which suggest

that these samples experienced temperatures <650 °C. The Ti-in-Bt thermometer (Henry et al., 2005) suggests that the metapelite and gneiss samples recorded temperatures of 552 ± 24 °C to 662 ± 24 °C and 678 ± 24 °C to 692 ± 24 °C, respectively (not plotted; Table 4). Garnets from the other garnet amphibolite samples show relatively flat compositional zoning (Fig. DR6 [see footnote 1]), which suggests diffusional reequilibration at temperatures >600 °C. All of the samples display signs of minor retrogression, including higher Mn along the rims (outer 15–25 μm) of garnet grains (Fig. DR6 [see footnote 1]) and minor chlorite overgrowth in the metapelite sample.

In summary, the metamorphic basement samples analyzed here experienced temperatures of 550–700 °C and were exhumed from
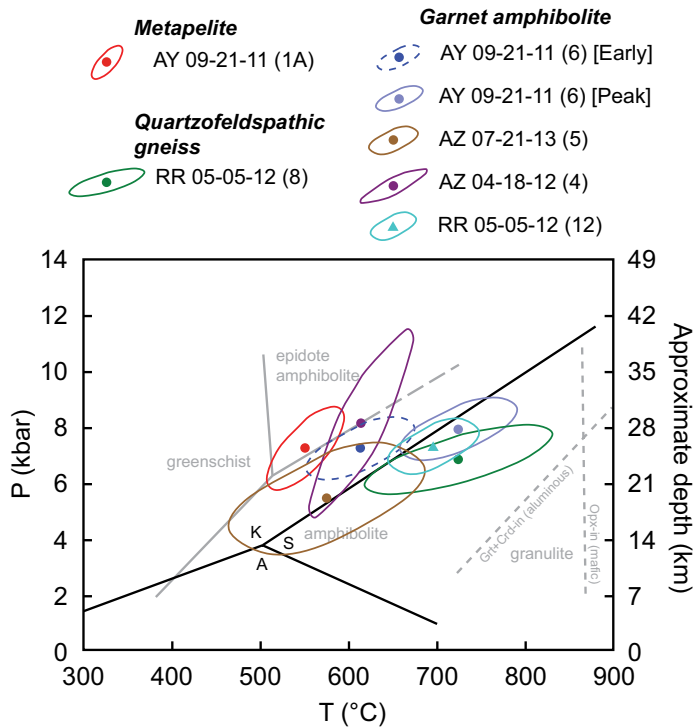
**Figure 15. Thermobarometry results, plotted as 2σ error ellipses for each sample. Aluminosilicate triple junction, greenschist-amphibolite-epidote amphibolite stability field (Evans, 1990), and granulate stability field (Pattison et al., 2003) are shown for reference. Approximate depth scale assumes a crustal density of 2850 kg/m³. A—andalusite; K—kyanite; S—sillimanite; Grt—garnet; Crd—cordierite; Opx—orthopyroxene; P—pressure; T—temperature.**

## Shule Nan Shan

The ranges bounding Hala Lake to the northeast and northwest expose Ordovician and Proterozoic basement rocks overlain by Carboniferous through Triassic strata (Fig. 8). The Shule Nan Shan range is bounded to the southwest by NW-striking thrust faults (Fig. 8) that place Proterozoic–Paleozoic rocks over Neogene–Quaternary rocks in the Hala Lake Basin. Structures under Hala Lake were inferred by projecting along-strike geometric relationships and bedding attitudes observed to the northwest of the lake. For convenience of description, the NW- to W-striking thrust faults are labeled *f*a through *f*f, from south to north, respectively (Fig. 8), and they are discussed in this order next.

### Fault a

The WNW-striking *f*a fault dips 70° to the NE, juxtaposes Triassic rocks ($\text{Ŧ}_2$-$\text{Ŧ}_3$) against Permian-Triassic strata (P-$\text{Ŧ}_2$), and truncates overlying Neogene sediments (Fig. 8). The observed juxtaposition must have accommodated <100 m of slip. The fault trace to the east is obscured by Hala Lake.

### Fault b

The WNW-striking *f*b-fault dips 60° NNE and places Carboniferous rocks (C) against Permian strata (P; Fig. 8). Units beneath Carboniferous rocks are not exposed, which constrains the maximum fault offset on *f*b to hundreds of meters.

### Fault c

This S-dipping *f*c fault has a variable E-ENE strike. In the west, the fault places an ~8-km-wide hanging-wall anticline of Permian strata (P) over a footwall syncline of Permian–Triassic rocks (P-$\text{Ŧ}_1$; Fig. 8). Map-view relationships suggest that offset increases to the east, but exposure is obscured by Hala Lake and the surrounding basin. This fault appears to either be truncated by, or merge with, *f*d, although this relationship is not directly observed (Fig. 8).

### Fault d

The trace of the *f*d NE-dipping fault is readily identified in satellite images as a conspicuous fault scarp that cuts across abandoned Quaternary alluvial fans. It also uplifts Neogene sediments (Fig. 8), and it is probably an active structure. The fault merges with *f*e to the east and is assumed to be north-dipping and merge with both *f*e and *f*f at depth.

### Fault e

This NW-striking, NE-dipping, range-bounding *f*e-fault of the Shule Nan Shan places Carboniferous rocks over Permian strata and overlying Neogene sediments (Fig. 8). The fault merges to the east with the Haiyuan fault (Fig. 8) and represents the westernmost termination structure of this major strike-slip fault. Kilometer-scale folds are observed in the hanging wall of this fault, exposing Carboniferous–Late Triassic rocks (C-$\text{Ŧ}_3$; Fig. 8). Although no direct fault kinematic measurements were made for this fault, the fold axes are parallel to the fault strike, which may suggest that this fault is primarily a dip-slip structure. Fault offset must be <1 km based on the map-view relationships, and the tight (~1 km wavelength) hanging-wall folds accommodate a similar magnitude of shortening. This fault is possibly a splay of *f*f, which accommodates larger-magnitude offset associated with the growth of the Shule Nan Shan range (Fig. 8).

### Fault f

This NE-dipping *f*f-thrust places the Proterozoic schist unit (Pt[sch]) over Permian rocks (P). The gently NE-dipping (15°–20°) Carboniferous–Triassic strata are interpreted to parallel the hanging-wall flat of this south-directed thrust fault, and thus parallel the dip of the fault. A minor fault splay *f*f$_2$ links with *f*f to the east and truncates an Ordovician granitoid and overlying Carboniferous strata. Fault *f*f$_2$ cuts the granitoid and overlying sedimentary strata, but offset diminishes within the granitoid. The fault trace of *f*f$_2$ to the east is covered by Quaternary sediments, but it is assumed that the fault merges to the east with *f*f at depth.

## Tuo Lai Nan Shan

The Tuo Lai Nan Shan range bounds the Shule River valley to the north (Fig. 9). Neogene outcrops are exposed along the margins of the valley, unconformably overlying Triassic strata (Fig. 9). Proterozoic–Paleozoic rocks are juxtaposed against the Neogene deposits by south-directed Cenozoic thrust faults. Discussion of these faults, which are labeled *f*1 through *f*4 from south to north, respectively (Fig. 9), is given next.

### Fault 1

This WNW-striking, N-dipping thrust fault places Triassic rocks over Neogene sediments and other Triassic strata (Fig. 9). Here, we denote the western and eastern traces off these faults as *f*1a and *f*1b, respectively.

TABLE 4. PRESSURE-TEMPERATURE (*P-T*) DATA FROM THERMOCALC FOR SELECTED METAMORPHIC ROCKS

| Sample | Location* | Minerals† | *T* (°C) | S.D. | *P* (kbar) | S.D. | Corr§ |
|---|---|---|---|---|---|---|---|
| AY 09-21-11 (1A) | grt3b_p | Grt Bt Ms Pl | 490 | 83 | 7.4 | 1.4 | 0.813 |
| Garnet–mica schist | grt3a_p | Grt Bt Ms Pl | 591 | 80 | 8.3 | 1.3 | 0.729 |
| [38.71625°N, | | Grt Bt Ms Pl | 531 | 90 | 7.8 | 1.5 | 0.757 |
| 98.59714°E, 3503 m] | grt4_p | Grt Chl Ms Pl H₂O# | 555 | 19 | 6.2 | 1.0 | 0.595 |
| | grt5_p | Grt Bt Ms Pl | 450 | 153 | 7.0 | 2.6 | 0.865 |
| | | Ti-in-Bt** | 569 | 24 | – | – | – |
| | *Weighted average (95% confidence)#* | | 552 | 35 | 7.2 | 1.2 | 0.724 |

#$X_{H_2O}$ = 0.68; no water yields 561 ± 72 °C and 5.1 ± 1.1 kbar

| Sample | Location* | Minerals† | *T* (°C) | S.D. | *P* (kbar) | S.D. | Corr§ |
|---|---|---|---|---|---|---|---|
| AZ 04-18-12 (4b) | grt1_p | Grt Bt | 589 | 23 | – | – | |
| Garnet–mica schist | grt4_p | Grt Bt | 674 | 23 | – | – | |
| [38.50647°N, | grt1 | Ti-in-Bt** | 572 | 24 | – | – | |
| 98.69933°E, 4314 m] | grt4 | Ti-in-Bt** | 662 | 24 | – | – | |
| | *Weighted average (95% confidence)* | | 625 | 23 | | | |
| RR 05-05-12 (8) | grt1_p | Grt Bt Ms Pl H₂O | 714 | 27 | 6.1 | 1.1 | 0.722 |
| Quartzofeldspathic gneiss | | | 730 | 29 | 6.5 | 1.1 | 0.727 |
| | | Ti-in-Bt** | 692 | 24 | – | – | – |
| [38.58889°N, | grt2_p | Grt Bt Ms Pl Kf H₂O | 748 | 29 | 7.4 | 1.1 | 0.716 |
| 98.54025°E, 4215 m] | | | 733 | 28 | 6.7 | 1.1 | 0.722 |
| | | Ti-in-Bt** | 678 | 24 | – | – | – |
| | grt3_p | Grt Bt Ms Pl Kf H₂O | 728 | 27 | 7.0 | 1.1 | 0.726 |
| | *Weighted average (95% confidence)#* | | 725 | 85 | 6.8 | 1.0 | 0.723 |
| AY 09-21-11 (6) | grt1_p | Grt Pl Qtz Hbl | 748 | 93 | 7.8 | 1.5 | 0.607 |
| Garnet amphibolite | | | 872 | 101 | 9.8 | 1.6 | 0.725 |
| [38.65617°N, | grt2_p | Grt Pl Qtz Hbl | 685 | 73 | 7.6 | 1.2 | 0.635 |
| 98.60970°E, | | | 664 | 89 | 7.2 | 1.5 | 0.698 |
| 3853 m] | | | 699 | 72 | 7.9 | 1.2 | 0.635 |
| | | | 738 | 80 | 8.1 | 1.3 | 0.645 |
| | grt4_p | Grt Pl Qtz Hbl | 638 | 65 | 6.4 | 1.0 | 0.585 |
| | | | 799 | 90 | 9.0 | 1.4 | 0.673 |
| | | | 838 | 95 | 9.7 | 1.5 | 0.689 |
| | *Weighted average (95% confidence)* | | 725 | 53 | 7.9 | 0.9 | 0.655 |
| | grt1_c | Grt Pl Qtz Hbl | 635 | 68 | 6.7 | 1.2 | 0.664 |
| | | | 638 | 69 | 6.7 | 1.2 | 0.659 |
| | grt2_c | Grt Pl Qtz Hbl | 591 | 63 | 6.8 | 1.1 | 0.670 |
| | | | 634 | 68 | 6.5 | 1.1 | 0.641 |
| | grt2_c | | 601 | 64 | 7.6 | 1.2 | 0.672 |
| | | | 601 | 64 | 8.2 | 1.3 | 0.671 |
| | grt4_c | Grt Pl Qtz Hbl | 607 | 65 | 7.9 | 1.2 | 0.675 |
| | *Weighted average (95% confidence)* | | 614 | 49 | 7.2 | 0.9 | 0.665 |
| RR 05-05-12 (12) | grt1_c | Grt Pl Qtz Hbl | 629 | 135 | 6.7 | 2.2 | 0.555 |
| Garnet amphibolite | | | 613 | 161 | 6.0 | 2.6 | 0.515 |
| [38.66431°N, | | | 605 | 157 | 6.3 | 2.6 | 0.531 |
| 98.56219°E, 3725m] | grt4_c | Grt Pl Qtz Hbl | 669 | 67 | 7.3 | 1.1 | 0.540 |
| | *Weighted average (95% confidence)* | | 650 | 100 | 7.0 | 1.7 | 0.535 |
| | grt1_p | Grt Pl Qtz Hbl | 772 | 91 | 9.0 | 1.5 | 0.683 |
| | | | 825 | 96 | 10.1 | 1.6 | 0.644 |
| | grt4_p | Grt Pl Qtz Hbl | 788 | 138 | 7.8 | 2.1 | 0.591 |
| | | | 772 | 123 | 7.9 | 1.9 | 0.589 |
| | grt1 | Hbl-Pl†† | 695 | 35 | – | – | – |
| | *Weighted average (95% confidence)#* | | 791 | 110 | 8.9 | 1.7 | 0.627 |
| | grt1_r | Grt Pl Qtz Hbl | 667 | 68 | 6.3 | 1.1 | 0.558 |
| | grt4_r | Grt Pl Qtz Hbl | 658 | 67 | 6.0 | 1.1 | 0.550 |
| | *Weighted average (95% confidence)* | | 662 | 95 | 6.2 | 1.6 | 0.554 |
| | Overall weighted average (95% confidence) | | 696 | 41 | 7.3 | 0.8 | 0.575 |
| AZ 07-21-13 (5) | grt1_c | Grt Pl Qtz Hbl | 574 | 102 | 4.6 | 1.8 | 0.590 |
| Garnet amphibolite | grt1_p | | 574 | 71 | 5.2 | 1.3 | 0.587 |
| [38.73502°N, | grt1_r | | 578 | 68 | 6.1 | 1.3 | 0.573 |
| 98.52050°E, 3459 m] | *Weighted average (95% confidence)* | | 576 | 88 | 5.4 | 1.6 | 0.583 |
| AZ 04-18-12 (4) | grtb1_p | Hbl-Pl†† | 611 | 24 | – | – | |
| Garnet-epidote amphibolite gneiss | grt1a_p | Grt Pl Qtz Hbl Ep | 686 | 133 | 8.2 | 1.9 | 0.867 |
| | grt1b_p | Grt Pl Qtz Hbl Ep | 683 | 145 | 8.1 | 2.0 | 0.873 |
| [38.50647°N, 98.69933°E, 4314 m] | *Weighted average (95% confidence)* | | 615 | 47 | 8.1 | 2.7 | 0.870 |

*Location within the thin section (e.g., the specific garnet grain); r—retrogressed rim, p—inferred peak-metamorphism position based on garnet compositional zoning, and c—early metamorphism recorded in the core of the garnet grain.
†Mineral abbreviations: Grt—garnet, Bt—Biotite, Chl—Cholorite, Ms—muscovite, Pl—Plagioclase, Kf—Alkali feldspar, Qtz—Quartz, Hbl—Hornblende, Ep—Epidote.
§Corr is correlation coefficient from Tʜᴇʀᴍᴏᴄᴀʟᴄ (Holland and Powell, 1998).
#Average of Tʜᴇʀᴍᴏᴄᴀʟᴄ data only.
**Ti-in-biotite geothermometer of Henry et al. (2005).
††Geothermometer for coexisting hornblende and plagioclase of Holland and Blundy (1994).

Fault *f1a* places an anticline of Triassic strata (Ŧ₃), which is likely cored by P-Ŧ₂ as in the east, over Neogene sediments. A minor (~100 m wavelength) hanging-wall anticline forms in the hanging wall of this steeply dipping thrust fault. In the east, *f1b* branches into several fault splays, which variably place Triassic (Ŧ₃) rocks over Neogene sediments and other Late Triassic rocks (Ŧ₃; Figs. 10E–10F). Offset on this fault is minor, as evidenced by minor map-view offset of the Ŧ₃–Ŧ₂ contact and the duplication of similar-aged units. This fault is inferred to merge to the east with the range-bounding *f3*. The geometry of *f1b* at depth is constrained by the focal mechanism (thrust dipping 27°N) from a 1993 $M_w = 5.9$ event that has been relocated by Chu et al. (2009) to have occurred at a depth of ~7 km (Fig. 9). In light of this observation, it is apparent that *f1b* is an active structure.

### Fault 2

The WNW-striking faults are anomalous in the mapping area because they involve a northward transport direction. In the west, this fault is labeled as *f2a* (Fig. 9). It is south-dipping and places a hanging-wall anticline of Triassic strata (Ŧ₃) over Jurassic rocks. Jurassic strata in the footwall of *f2a* are internally deformed, with numerous 100-m-wavelength folds and faults. *Fault 2a* must be relatively low angle (10–20°S) based on its map trace (Fig. 9).

In the east, this fault is labeled as *f2b*. This fault merges to the west and east with *f3*. There is a prominent ~5-km-wide anticline in the hanging wall of *f2b*, just to the south of the surface trace *of f2b*, which is referred to as the Shule anticline because it is exposed along the northern bank of the Shule River (Fig. 9). The anticline is overturned and north-verging; its northern limb is overturned to the south, and its southern limb dips to the south (50–60°S; Fig. 9). Fault *2b* truncates this anticline, and cuts up section to the northwest through Lower Triassic to Upper Triassic rocks (Ŧ₁–Ŧ₃). This truncation relationship suggests that *f2b* is a south-dipping thrust, the Shule anticline is the hanging-wall anticline of this thrust, and fault *2b* accommodated top-to-the-north motion. However, where this fault is exposed in a north-trending drainage along the northern overturned limb of the Shule anticline, the fault dips to the north (Figs. 9 and 10D). At this locality, the fault surface dips 60°N, Jurassic strata in the hanging wall are parallel to the fault, and Triassic rocks in the footwall are oblique to the fault surface (Fig. 10D). This geometric relationship alone would suggest a hanging-wall flat-footwall ramp in a north-dipping normal fault. Alternatively, this fault juxtaposition may be part of an overturned thrust that was originally S-dipping and placed Triassic rocks over Jurassic

strata. Following this interpretation, the Triassic rocks make up a hanging-wall ramp, whereas the Jurassic strata are part the footwall flat, and the fault was overturned by south-directed shear. The north-verging Shule anticline and map-view truncation relationships support this second interpretation (Fig. 9), and the south-directed *f3* may have caused this overturning of *f2b*. A field photograph in Figure 10C shows the overturned thrust *f2b* and south-directed *f3*.

### Fault 3

This NW-striking fault dips to the north and juxtaposes Triassic (Ŧ₂) through Proterozoic rocks over Cenozoic–Triassic strata (N-Ŧ₃). The laterally continuous fault crosses the entire mapping region (Fig. 9). The hanging wall consists of Middle Triassic strata (Ŧ₂) unconformably overlying Proterozoic basement rocks (Pt[sch] and Pt[gn]). There is a thin veneer of Carboniferous rock beneath the Triassic strata, which also unconformably overlie the Proterozoic rocks (Fig. 9). In the west, this fault juxtaposes Triassic rocks (Ŧ₂) over Jurassic–Neogene strata (J-N). Here, the fault either merges with or truncates *f2a* (Fig. 9). The eastern portion of this fault cuts both up and down section through the Shule anticline, which requires this fault to be out-of-sequence with respect to north-verging *f2b*. These two faults either merge above the erosional surface, or *f3* crosscuts *f2b*; the second option, and the duplication of *f2b*, is not observed in the mapping area.

### Fault 4

This N-dipping fault places metamorphic basement rocks over a syncline of Triassic strata (Ŧ₂-Ŧ₃). The surface trace of *f4* is readily identifiable along the southern flank of the highest peaks of the Tuo Lai Nan Shan, as this fault defines a sharp change in slope; Triassic rocks in the footwall are less resistant than the metamorphic rocks in the hanging wall. The Triassic footwall syncline is truncated by *f4*, and map relationships suggest that this syncline is overturned in the west, above the erosional surface. Fault *4* splits into two fault splays in the west: *f4a* and *f4b*. Fault *4a* places undifferentiated marble and schist rocks over the southern limb of the Triassic syncline (Fig. 9). Based on its surface trace, *f4b* must be relatively low angle (10–20°N). This fault juxtaposes Proterozoic schist and gneiss against undifferentiated marble and schist rocks. There are no constraints as to whether this fault is Cenozoic in age or older. Northeast-dipping (35–45°NE) Carboniferous–Permian strata unconformably overlie the Pt(sch) along the southern bank of the Tuo Lai River (Fig. 9), which indicates that this this unconformity horizon continues above the erosional surface to the southeast.

### Tuo Lai Shan

The Tuo Lai Shan is bounded by the Tuo Lai River to the south and Heihe River to the north (Fig. 9). This range was constructed primarily by south-directed thrusting of early Paleozoic rocks over Cretaceous and younger strata (Fig. 9). Numerous fault splays within nonbedded and highly deformed units make precise interpretation of these faults difficult, but we discuss three major thrust faults here. These are labeled *f5* through *f8*, from south to north respectively (Fig. 9).

### Fault 5

The NW-striking, NE-dipping thrust fault consists of Ordovician strata and early Paleozoic granitoid rocks in its hanging wall (units O, O[gr], and gr) and Proterozoic metamorphic rocks (Pt[sch], Pt[gn], and Pt[gr₁]) in its footwall (Fig. 9). The main fault and related splays dip ~35–60°NE. The fault is covered by Quaternary river deposits in the west, and its eastern extent is unknown (Fig. 9).

### Fault 6

This label is given to the major thrust fault(s) that place Precambrian and/or high-grade metamorphic rocks (Z and sch) over strongly deformed Ordovician strata and early Paleozoic granitoid rocks (units O, O[gr], and gr; Fig. 9). In the west, the label *f6a* specifically refers to the fault that juxtaposes Z(sch) against Ordovician strata that are intruded by early Paleozoic plutons (Fig. 9). This NE-dipping thrust fault also has Cretaceous and Carboniferous rocks in its footwall. It merges to the east with *f6b*, which specifically places the undifferentiated sch unit over the combined Ordovician strata–pluton unit (O and gr; Fig. 9). This fault is also N-dipping and has a syncline of Carboniferous and Cretaceous rocks in its footwall. Fault *6b* also places the ophiolite complex over Ordovician strata in the farthest east portion of the mapping area (Fig. 9). To the south of the ophiolite complex, several splays of *f6b* duplicate a suite of Ordovician rocks that are intruded by O(gr) and overlain by Carboniferous–Permian rocks (Fig. 9).

### Fault 7

This NW-striking, SW-dipping fault places a complex of Neoproterozoic marble and schist and Cambrian ophiolitic rocks (Z and Ɛ) over Ordovician and late Paleozoic strata (O, C, and P; Fig. 9). Where observed, this fault dips 40°SW (Fig. 9). This fault is inferred to be a back thrust of *f6*, and thus they are expected to merge at depth. Footwall strata (C and P) are variably folded at wavelengths of ~2–3 km. Fault 7 merges to the west with *f6a* and *f8*.

## Fault 8

This major NE-dipping fault brings Neoproterozoic marble and schist rocks (Z[sch] and Z[mb]) over footwall rocks that include Neoproterozoic and Ordovician rocks unconformably overlain by Carboniferous–Permian strata (Fig. 9). These late Paleozoic footwall strata are folded at a kilometer scale. In the west, several fault splays duplicate series of Neoproterozoic schist overlain by Carboniferous strata (Fig. 9). Hanging-wall rocks of *f8* are unconformably overlain by Mesozoic strata (J and K; Fig. 9). Several faults observed in the hanging wall of *f8* are entirely within Paleozoic or older rocks, and the timing of their activity is unconstrained.

## Structural Data from the Metamorphic Basement

The Proterozoic schist and gneiss units have strongly developed foliations and stretching lineations. These fabrics are inferred to have developed in the early Paleozoic as a result of the Qilian arc and orogen at amphibolite-grade conditions as documented in this study (Fig. 15). Our geochronologic analyses suggest that this broad shear zone was active in the Early Ordovician, and shearing ceased by ca. 445 Ma. Foliations are defined by mica layering in the mica ± garnet schist rocks, gneissic banding with relatively mafic (biotite and amphibole) and felsic (plagioclase and quartz) layers, plagioclase layering in foliated garnet amphibolite rocks, or weak-to-strong mineral alignment (mostly mica and amphibole grains) in the foliated granitoid rocks. Stretching lineations are observed within the foliation surface, and stretched quartz or plagioclase is most evident in many outcrops. Kinematic indicators, including S-C fabric and mantled porphyroclasts (e.g., σ- and δ-clasts), suggest apparent right-lateral shear (Figs. 6 and 10G–10I).

The foliation and stretching lineation data from the metamorphic basement rocks were compiled and analyzed in several stereonets (Fig. 9) using Stereonet 9 (software by Rick Allmendinger). In the metamorphic rocks to the north of *f4* in the Tuo Lai Nan Shan (Fig. 9), the foliations are all roughly parallel, near vertical, and strike northwest. Stretching lineations within these units are subhorizontal and trend northwest. South of *f4*, the data are more diverse. Foliations are variable, generally NW striking, and most lineations are SE trending and subhorizontal (Fig. 9).

Because this metamorphic unit has been affected by later deformation (e.g., Cenozoic folding and thrust faulting), it is possible that these foliation and lineation attitudes were modified from their original early Paleozoic configuration. For example, the near-vertical foliations and subhorizontal lineations could have originally been part of a major early Paleozoic thrust fault with dip-slip stretching lineations. To constrain their original orientation, the foliation and lineation attitudes were rotated back to a pre-Carboniferous state by rotating the data so that the Carboniferous strata are horizontal (Fig. 9B; further explanation is in the GSA Data Repository [see footnote 1]). The average foliation attitude and lineation plunge-trend observations from the corrected pre-Carboniferous data sets are 126/84 SW and 12/119, respectively (Fig. 9B). Considering the observed right-lateral shear sense across this broad zone (Figs. 10G–10I), our observations suggest that the sheared basement rocks were part of an early Paleozoic right-slip strike-slip shear zone (Fig. 6).

The Cambrian ophiolite (i.e., fragments of the Yushigou ophiolite) and mélange units (Figs. 10L–10M) are only juxtaposed against the Neoproterozoic marble unit, and, where observed, the Neoproterozoic unit is always structurally beneath the ophiolite suite (Fig. 6). Although this tectonic contact may have been reactivated in the Cenozoic, this relationship suggests that the Neoproterozoic strata were originally thrust beneath the obducted ophiolite suite during the Qilian orogen.

Early Paleozoic slightly deformed to undeformed plutonic rocks are common throughout the mapping area (Figs. 8 and 9). These granitoids, which range in composition from alkali feldspar granite to quartz monzonite, intrude basement rocks and early Paleozoic strata. Furthermore, these plutons intrude the contact between the Ordovician and Proterozoic basement units (Fig. 9), which requires that Ordovician sediments were deposited on Proterozoic basement prior to intrusion. The plutons also intrude the northern schist unit in the Tuo Lai Shan (Fig. 9), which presently has no independent age constraints, suggesting that this schist is similar to the Proterozoic schist in the Tuo Lai Nan Shan (Fig. 9). It is important to note that the Ordovician plutons do not intrude Neoproterozoic rocks that are inferred to be part of North China's passive continental margin (e.g., Xu et al., 2015).

Carboniferous strata unconformably overlie these plutonic rocks, Proterozoic rocks, and early Paleozoic strata (Figs. 8 and 9), which indicates that following early Paleozoic Qilian orogeny, all of these units were at or near the surface. We also use this unconformity surface as a marker horizon for cross-section restoration.

## DISCUSSION

### Pre-Cenozoic Deformation in Northern Tibet

Early Neoproterozoic (i.e., ca. 1.0–0.9 Ga) plutonism across northern Tibet (e.g., Wu et al., 2016, 2017a) was followed by local deformation. Leucogranites and metamorphic zircon rims have been reported with ages of ca. 0.9–0.85 Ga in the Tian Shan, Tarim, and Qilian Shan (Gehrels et al., 2003b; Zhu et al., 2011; Kröner et al., 2013; Wang et al., 2014; Käßner et al., 2017). This age signature is associated with the inferred collision between North and South Tarim along the Tarim suture (Guo et al., 2005; Zuza and Yin, 2017).

In the late Neoproterozoic, rifting led to the opening of the Qilian Ocean (e.g., Song et al., 2013). Cambrian-aged ophiolites are found throughout the Qilian Shan, and many are supra-subduction zone types with zircon ages ranging from 540 to 500 Ma (Xia and Song, 2010; Song et al., 2013; this study). Continental volcanic arc magmatism began by at least ca. 520 Ma, and arc-related plutons have ages that range from ca. 520 Ma to 440 Ma (e.g., Dang, 2011; Xia et al., 2012; Xiao et al., 2012; Song et al., 2013; Wu et al., 2016). Supra-subduction zone ophiolite formation and subduction initiation may correspond with the oldest monazite age population obtained in this study (i.e., 538 Ma; Fig. 13).

The earliest recorded local magmatism occurred at ca. 475 Ma (Table 2), which overlaps with the main population of included-in-garnet monazite ages at ca. 485–475 Ma (Fig. 13). Peak prograde metamorphism at this time and right-slip shearing were operating at depths of 20–30 km (Figs. 15 and 16). Ductile shearing of these rocks ceased by ca. 445 Ma, when the foliated metamorphic rocks were crosscut by an undeformed granitoid dike with a U-Pb age of 445 ± 3 Ma (Figs. 10K and 13; Table 2). The depth of dike emplacement is not constrained, but it must have occurred somewhere between when the intruded gneiss was at amphibolite-grade conditions at ca. 480 Ma and when the Qilian basement was exposed at the surface during the deposition of Devonian sediments.

Intrusions with ages ranging from 450 to 440 Ma are widespread throughout the Qilian Shan (e.g., Song et al., 2013; Wu et al., 2016, 2017a). Such extensive plutonism may have resulted from the collision between the North China and Kunlun-Qaidam continents (Wu et al., 2017a), although this cannot be directly confirmed in the study area. This pulse of magmatism also corresponds to the youngest matrix monazite ages in the analyzed metapelite samples (Fig. 13).
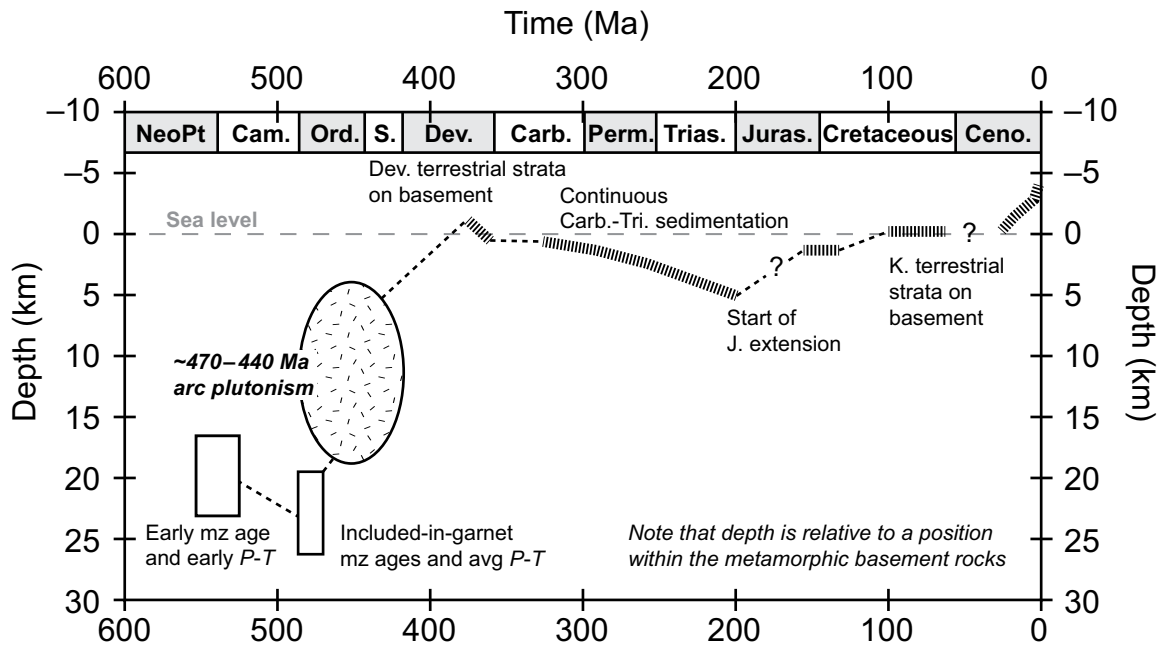
**Figure 16. Estimated depth history for the metamorphic basement rocks of the central Qilian Shan from the Neoproterozoic to the present. The oldest population of monazite ages (ca. 540 Ma) may correspond to the earliest stage pressure-temperature (*P-T*) estimates. Subduction and arc magmatism thickened the continent, resulting in peak *P-T* conditions and the main population of included-in-garnet monazite ages (ca. 480 Ma). Magmatism continued throughout the Silurian, and late *P-T* conditions record shallow crustal depths, possibly as a result of erosion. Metamorphic foliations were truncated by undeformed granite at ca. 445 Ma. Devonian molasse was unconformably deposited on basement rocks, which requires that the basement rocks were exhumed to near the surface by this time. Continuous shallow-marine to lacustrine Carboniferous–Triassic sedimentation suggests that these rocks remained near Earth's surface. Jurassic and Cretaceous extension led to progressively shallower to terrestrial sedimentation, and Cenozoic deposits are entirely terrestrial during intracontinental shortening. Abbreviations: mz—monazite; avg—average; NeoPt—Neoproterozoic; Cam.—Cambrian; Ord.—Ordovician; S.— Silurian; Dev.—Devonian; Carb.—Carboniferous; Trias.—Triassic; Juras.—Jurassic; Ceno.—Cenozoic.**

Prior to and during continental collision in the Qilian orogen, there was deposition of Silurian turbidite sequences to the north and south of the central Qilian Shan (e.g., Yan et al., 2010; Yang et al., 2012). These strata were likely deposited in back-arc and forearc-to-foreland basin settings as the Qilian arc transitioned to a collisional orogen. They were strongly deformed during the protracted continental collision. This collision brought basement rocks toward the surface, and Silurian strata and Devonian terrestrial sediments were deposited unconformably over the exposed basement rocks.

Widespread and laterally continuous Carboniferous shallow-marine deposition indicates that much of the Qilian Shan was at or just below sea level at this time (Fig. 16). Nearly uninterrupted shallow-marine sedimentation continued into the Triassic. The sedimentary facies do not vary significantly in the Carboniferous–Triassic sections, which requires either subsidence of the postorogenic Qilian Shan or eustatic

sea-level rise to accommodate the deposition of these strata.

Jurassic extension exhumed these rocks toward the surface, and Jurassic strata were deposited in a marginal marine to swamp setting (Fig. 7). Extensive Jurassic-aged coal deposits are widespread across the Qilian Shan. Regional extension continued into the Cretaceous, and subaerial sedimentation requires that local regions of the Qilian Shan were above sea level at this time (Fig. 16). Terrestrial late Oligocene to Miocene deposits record the initiation of shortening across the central Qilian Shan.

**Nature of the Early Paleozoic Qilian Arc**

In several of the reconstructions of the Qilian orogen and suture zone, the exposures of discontinuous UHP metamorphic rocks, ophiolite and mélange complexes, arc plutons, and blueschist rocks have been used as evidence to suggest that the Qilian orogen resulted from the

collision of multiple arcs along multiple sutures in the early Paleozoic (Table 1; Li et al., 1978; Hsü et al., 1995; Yin and Nie, 1996; Yin and Harrison, 2000; Xiao et al., 2009; Gehrels et al., 2011; Song et al., 2013, 2014). However, we note that the effects of Ordovician arc construction, protracted Silurian–Devonian continental collision, Mesozoic extension, and Cenozoic intracontinental deformation modified the original geological configuration.

Any viable model for the Qilian arc must explain the following key observations (Fig. 3; Table 1): (1) northward younging magmatism across northern Tibet (e.g., Zuza et al., 2015; Wu et al., 2016), (2) Cambrian supra-subduction zone–type ophiolite and mélange material dispersed throughout the Qilian Shan, (3) the spatial and temporal overlap between arc magmatism and UHP metamorphism in North Qaidam (e.g., Yin et al., 2007b), and (4) high-pressure blueschist rocks exposed in the northeastern Qilian Shan (e.g., Song et al., 2013; Fig. 2). The

temporal and spatial distribution of arc plutons could fit with any of the Qilian arc models except the north-dipping subduction model, because no Ordovician plutons intrude the North China craton (Fig. 3; Table 1). Given that most of the ophiolite complexes are supra-subduction zone–type ophiolites (e.g., Meng et al., 2010; Xia and Song, 2010; Song et al., 2013), these rocks may have been variably obducted onto the continental arc and/or underthrust beneath the Kunlun-Qaidam continent. This suggests the ophiolite fragments were initially scattered throughout the Kunlun-Qaidam continent even before Qilian orogen-related collision, which means that the bidirectional or multiple-arc models are not required to account for the extensive ophiolite-mélange distribution across the Qilian Shan (Fig. 3).

In light of these considerations, we believe that a single south-dipping subduction system operated along the northern margin of the Kunlun-Qaidam continent (Sobel and Arnaud, 1999; Gehrels et al., 2003a, 2003b). The distribution of Cambrian ophiolites and strata throughout the Qilian Shan may be the result of complex mélange/ophiolite obduction or ophiolite underthrusting. For example, the Mesozoic North American Cordilleran arc involved both complicated supra-subduction zone ophiolite obduction of the Coast Range ophiolite (e.g., Wakabayashi et al., 2010) and significant mélange underthrusting/underplating as far east as the Rand Schist outcrops (e.g., Grove et al., 2003; Chapman et al., 2016). Across the Qilian Shan, the wide belt of arc plutons that generally young to the north-northeast (e.g., Zuza et al., 2015; Wu et al., 2016, 2017a) can be explained by northward rollback of the Qilian oceanic slab. This also explains why Ordovician arc plutons intrude older Ordovician forearc sediments (Figs. 6 and 9). The blueschist rocks in the northeast Qilian Shan were generated in this subduction system. The 466–462 Ma Lu-Hf and Sm-Nd garnet ages from the blueschist record Ordovician subduction (Cheng et al., 2016), and the younger Early Silurian and/or Devonian blueschist cooling ages either record peak metamorphism or exhumation, respectively (e.g., Liu et al., 2006; Lin et al., 2010).

### Lateral Extent of the Qilian Suture

Based on similar lithological assemblages and geologic histories, it has been argued that the Qilian orogen and suture(s) were laterally continuous with the Qinling suture(s) to the southeast (Figs. 1 and 17; e.g., Xu et al., 2008; Tseng et al., 2009; Dong et al., 2011; Wu et al., 2017a; Zuza and Yin, 2017). However, the northwestern termination of this orogen

and suture is not known. Three geometrically plausible models exist for its continuation (Fig. 17): (i) it may continue into Tarim and be currently covered by Mesozoic–Cenozoic sediments (i.e., the contiguous South Tarim–Qaidam continent model) (e.g., Yu et al., 2017); (ii) it may veer to the south of Tarim and be overprinted by the Cenozoic Western Kunlun and Pamir thrust belts (i.e., the separate South Tarim and Qaidam continents model), although evidence for this suture in the Altyn Tagh Range suggests that the suture cannot be that far to the southwest (e.g., Sobel and Arnaud, 1999); or (iii) the Kunlun-Qaidam continent may have only partially separated from Tarim, and the abrupt western termination of the Qilian suture represents the western extent of the Qilian Ocean (i.e., the peninsular Kunlun-Qaidam continent model).

Each of the aforementioned configurations has implications for the nature of the Kunlun-Qaidam continent, including its size, geometry, origin, and tectonic relationships between constituent blocks (Fig. 17C). For example, the contiguous South Tarim–Qaidam continent model requires the southern portion of Tarim to have linked with the Kunlun-Qaidam continent in the Precambrian and that an early Paleozoic suture traverses Tarim. The separate South Tarim and Qaidam continents model is the only one that predicts the Kunlun-Qaidam continent to be an individual entity surrounded entirely by oceans, and therefore presently surrounded by suture zones, whereas the peninsular Kunlun-Qaidam continent model requires a Precambrian linkage between Qaidam and Tarim.

The Precambrian basement of Kunlun-Qaidam is similar to that of Tarim–North China (Hu et al., 2000; Gehrels et al., 2003b; Tung et al., 2007; Long et al., 2010; Zhao et al. 2012; Wu et al., 2016; Yu et al., 2017; Zuza and Yin, 2017), which indicates that these two continents may have been contiguous prior to Neoproterozoic rifting. In addition, no Phanerozoic sutures or amalgamation structures have been reported between the Kunlun-Qaidam and Tarim continents (Fig. 2), which further bolsters their Precambrian connection. Some researchers have argued that the Kunlun-Qaidam continent was connected to the South China craton in the Neoproterozoic based on correlative ca. 1100–900 Ma granites. However, this age signature is not unique among Precambrian continents, as similar-aged plutons are found within North China, Tarim, the Tian Shan, and the Central Asian microcontinents (e.g., Han et al., 2011; Rojas-Agramonte et al., 2011; Ma et al., 2012; Käßner et al., 2017; Wu et al., 2017a; Zuza and Yin, 2017). Based on these observations, we tentatively support the peninsu-

lar Kunlun-Qaidam continent model (scenario iii in Fig. 17C), although we emphasize that this issue is still unresolved.

### Mesoproterozoic–Paleozoic Tectonic Evolution of Northern Tibet

Here, we present a self-consistent tectonic model for the Mesoproterozoic to Paleozoic tectonic evolution of northern Tibet that conforms to our present understanding of the Qilian Shan (Fig. 18). In the Mesoproterozoic, passive-margin, continental-shelf, and/or continental-slope sediments were deposited along the southern edge of the linked North Tarim–North China craton (Fig. 18A). This margin faced the Tarim (or paleo-Qilian) Ocean, and the sediments consisted of ca. 1.8 Ga and ca. 1.45 Ga detrital zircon grains derived from the North China craton (i.e., sample AY 09-21-11 [1] in Fig. 5B; see also Gehrels et al., 2003a; Wu et al., 2017a). At ca. 1.0 Ga, north-dipping subduction along the southern margin of the North Tarim–North China continent accommodated the convergence of the continuous South Tarim–Qaidam continent and the closure of the Tarim Ocean (Fig. 18B; e.g., Guo et al., 2005; Xu et al., 2013). The 1.0–0.9 Ga granitoid belt that is exposed throughout Qaidam, the Qilian Shan, the Altyn Tagh Range, Tarim, and Tian Shan is evidence for the existence of the Tarim Ocean and Tarim arc (Fig. 18B). This subduction system generated Precambrian blueschist rocks that are presently observed near Aksu in Tarim (e.g., Liou et al., 1996; Zhu et al., 2011). The inferred suture associated with the collision of the South Tarim–Qaidam and North Tarim–North China continents is exposed at Aksu and partially parallels and overlaps with the Qilian and Qinling sutures to the southeast (Guo et al., 2005; Wu et al., 2016).

In the late Neoproterozoic, rifting of this joined continent initiated at variable times, resulting in the opening of the Paleo-Asian, Qilian, and Tethys Oceans, from north to south, respectively (Fig. 18C; Wu et al., 2016). The earliest phase of rifting and the opening of the Tethys Ocean initiated during or immediately following the aforementioned collision; bimodal volcanism and rift-basin development occurred at 900–870 Ma (Wang et al., 2015a, 2015b) along South Tarim's southern margin. The ca. 825 Ma Jinchuan ultramafic intrusion (Li et al., 2005) and deposition of the Hanmushan Group passive-margin strata may have been associated with the opening of the Paleo-Asian Ocean to the north of the North China craton (Fig. 18C; e.g., Wu et al., 2016). A-type ca. 820 Ma granites in the central Qilian Shan have been related to postorogenic extension fol-
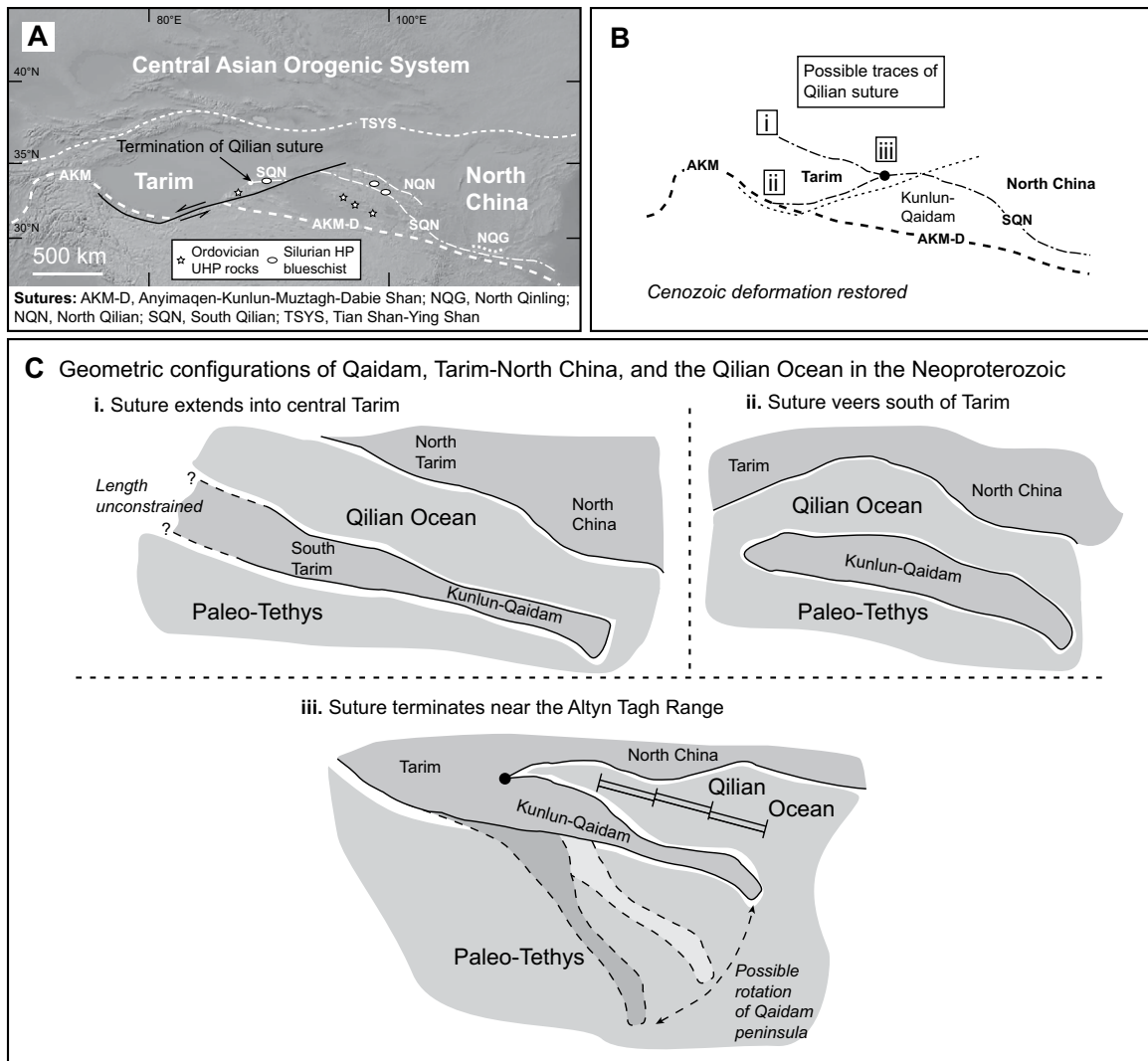
**Figure 17. (A) Simplified trace of Phanerozoic sutures showing outcrops of Ordovician ultrahigh-pressure (UHP) rocks and Silurian high-pressure (HP) blueschist. Note that the Qilian suture is offset by the Altyn Tagh fault. (B) Restored position of the Kunlun and Qilian sutures, after removal of the effects of Cenozoic shortening across the Qimen Tagh, Qaidam Basin, North Qaidam, and Qilian Shan thrust belts, and offset along the Altyn Tagh fault. Note that the Qilian suture aligns with the Altyn Tagh suture (i.e., the Lapeiquan suture of Sobel and Arnaud, 1999), and that the trace of the Qilian suture may either (i) continue across central Tarim to the northwest, (ii) veer south of the Tarim craton, or (iii) terminate near the Altyn Shan. (C) Three possible geometric configurations of the Kunlun-Qaidam continent and restored surface trace of the Qilian suture as shown in B. Figure is modified from Zuza and Yin (2017), and data were compiled from Sobel and Arnaud (1999), Yin et al. (2007a), Song et al., (2006, 2013, 2014), Gao et al. (2013), and Wu et al. (2016).**

lowing ca. 0.9 Ga orogeny (Wu et al., 2017a). The opening of the Qilian Ocean was preceded by bimodal volcanism from ca. 775 Ma to 600 Ma and the deposition of the passive-margin Baiyangguo/Daliugou Group (Fig. 18C; Tseng et al., 2006, 2007; Xu et al., 2015). This rifting occurred subparallel to the early Neoproterozoic Tarim suture zone. Because there are no observed Phanerozoic sutures or amalgamation structures between Qaidam and Tarim,

we infer that these continents remained connected during the opening of the Qilian Ocean (Fig. 17C). The Kunlun-Qaidam continent may have rotated away from North China as a peninsula that led to the opening of a westward-tapering Qilian Ocean. This interpretation also suggests that the Qilian Ocean was a relatively small sea and not a through-going ocean separating Laurasia and Gondwana (cf. Stampfli and Borel, 2002). The duration of Qilian arc ac-

tivity can place bounds on the minimum width of the Qilian Ocean. Given the arc was active for at least ~40 m.y. (i.e., 490–450 Ma), and observed modern subduction rates are typically 1–5 cm/yr (e.g., Clift and Vannucchi, 2004; Stern, 2011), there must have been between 400 and 2000 km of the Qilian Ocean to be consumed in the Qilian arc. These widths are reasonable given that the Kunlun-Qaidam continent was ≥1000 km long (Fig. 17C).
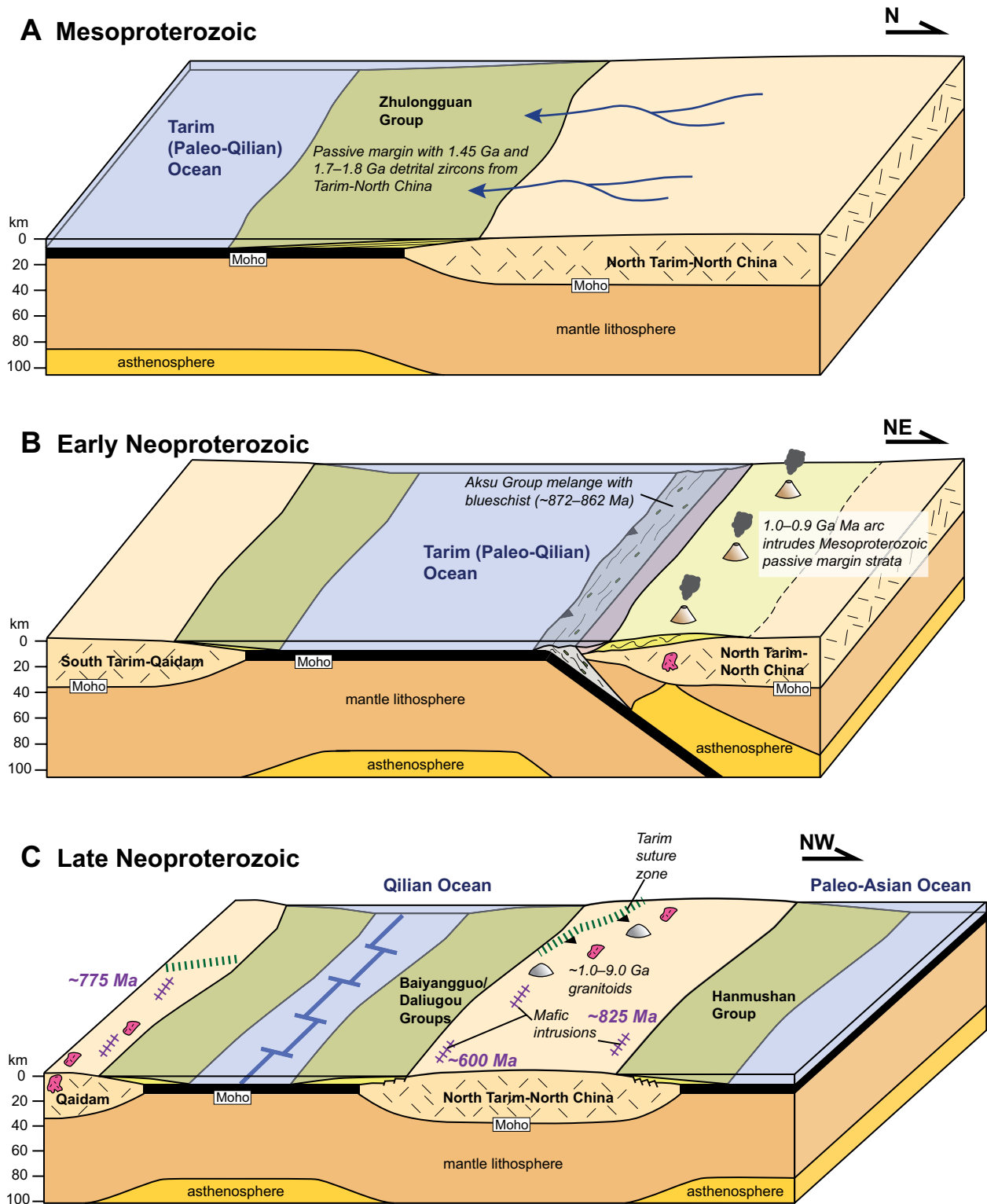
**Figure 18 (*on this and following two pages*). Block models showing the tectonic evolution of north Tibet and the Qilian Shan from the Mesoproterozoic through Devonian. (A) In the Mesoproterozoic, cratonal and/or passive-margin deposits along the southern margin of a combined North Tarim–North China continent possess ca. 1.45 and ca. 1.8 Ga detrital zircons. (B) Early Neoproterozoic north-dipping subduction leads to the development of the Tarim arc (with ca. 1.0–0.9 Ga magmatism), which accommodates the convergence of the South Tarim–Qaidam and North Tarim–North China continents. (C) Late Neoproterozoic rifting leads to the opening of the Qilian and Paleo-Asian Oceans. Bimodal volcanism (ca. 830–600 Ma) occurs throughout Qaidam, Tarim, and North China.**
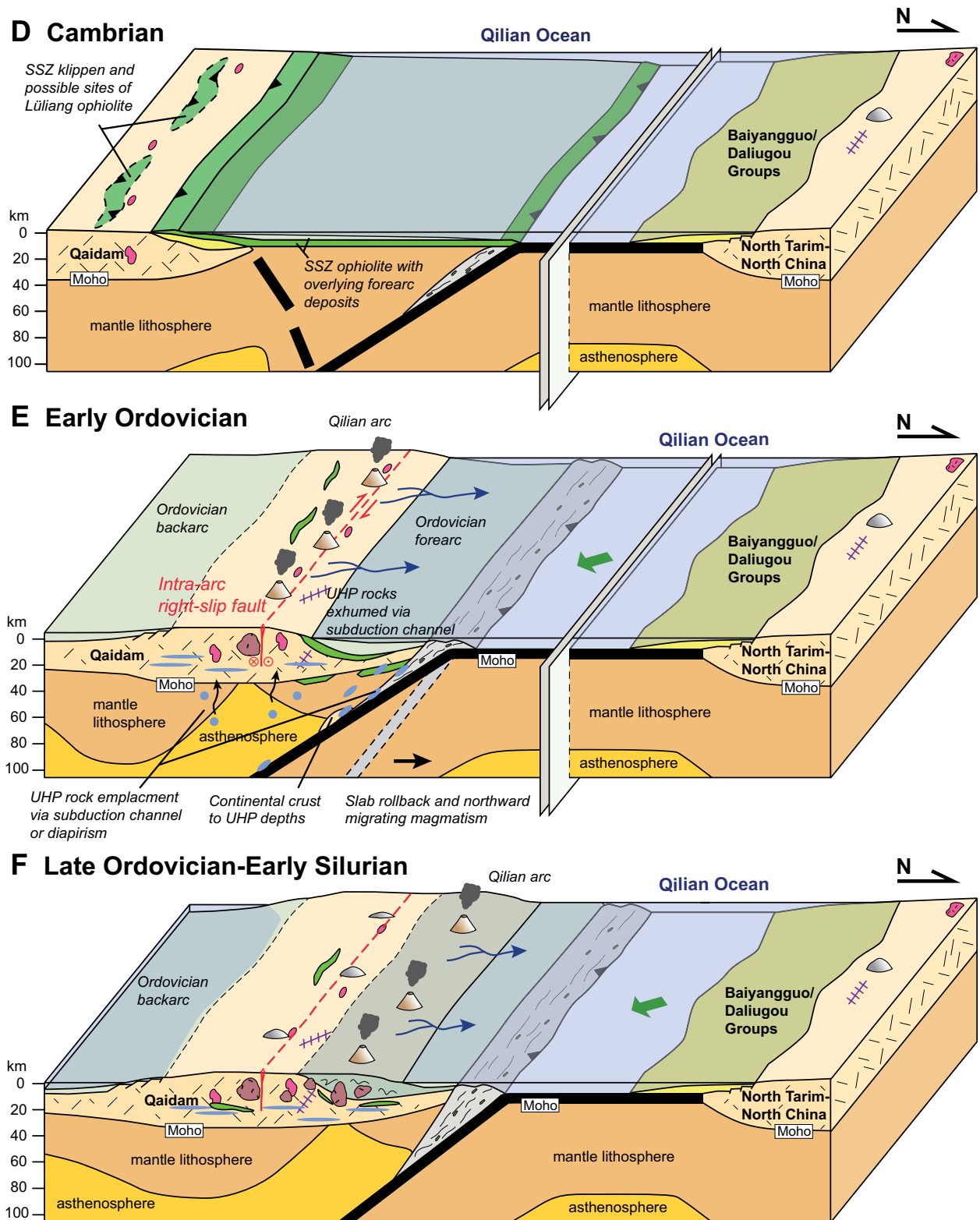
**Figure 18** (*continued*). **(D)** Cambrian-aged supra-subduction zone (SSZ) ophiolites are generated in an incipient arc setting, as south-dipping subduction initiates just north of Qaidam's northern margin. The supra-subduction zone ophiolites are obducted onto Qaidam and underthrust beneath the continent. **(E)** Continental arc magmatism initiates in earnest in the Ordovician, along with a trench-parallel intra-arc right-lateral strike-slip fault. Continental crust is brought to ultrahigh-pressure (UHP) depths along the subduction channel, and it is returned to midcrustal levels by via diapiric flow or subduction channel flow. **(F)** Slab rollback causes the northward-migrating arc to develop on older Ordovician and Cambrian strata.

**G Silurian-Devonian**
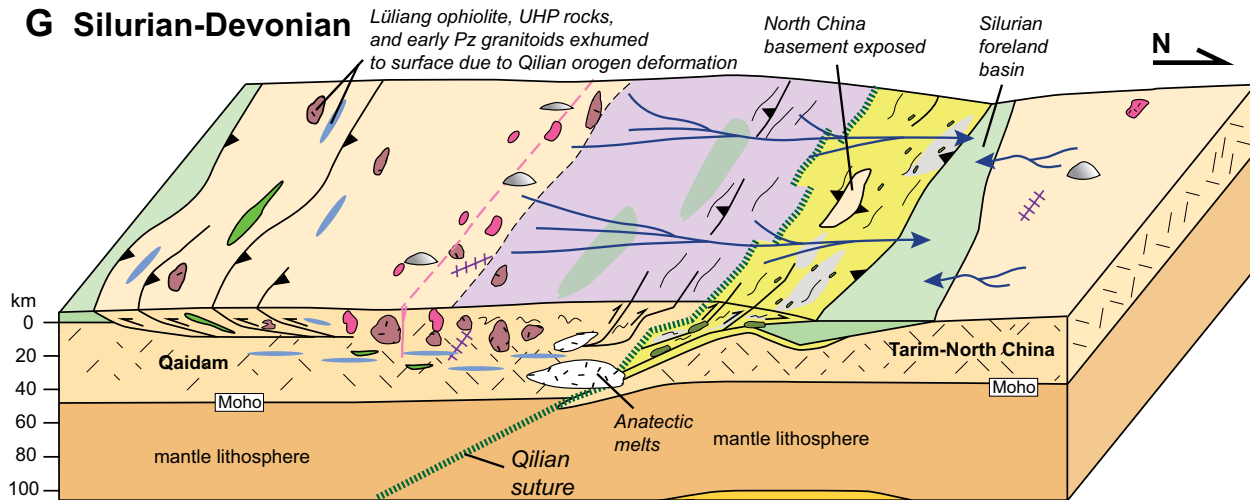


**Figure 18** (*continued*). **(G) Collision between Qaidam and North China occurs at ca. 440 Ma and is associated with a magmatic pulse at this time. Syn- and postorogenic magmatism is diffuse but widespread. Continued convergence variably exposes ophiolites and basement rocks to surface by the Devonian. Pz—Paleozoic.**

In the Cambrian, the Qilian Ocean reached its maximum extent, and subduction initiated along the southern bounds of this ocean. During nascent arc formation, the Qilian supra-subduction zone ophiolites were generated (ca. 540–500 Ma) to the north of the Kunlun-Qaidam continent (Fig. 18D). Inherited zircon ages during this time recorded a complex process of recycling and influence of underlying and adjacent continental crust. Continental subduction began in the Early Ordovician as Qilian oceanic lithosphere dipped southward beneath the Qaidam continent. The Qilian supra-subduction zone ophiolite obducted onto Qaidam and was also simultaneously underthrust beneath the continent (Fig. 18D; e.g., Grove et al., 2003; Chapman et al., 2016). These dispersed ophiolites are observed throughout the present-day Qilian Shan and North Qaidam.

In the Ordovician, volcanic arc magmatism began as the Qilian Ocean subducted beneath the Kunlun-Qaidam continent (Fig. 18E). Ordovician strata were deposited in back-arc and forearc settings, to the south and north of the Qilian arc, respectively. During this time, fragments of the Kunlun-Qaidam continent were brought to UHP depths via the subduction channel (e.g., Yin et al., 2007b; Menold et al., 2016; Sievers et al., 2017). The UHP rocks were later exhumed to the middle crust via either diapiric or subduction-channel flow (e.g., Mattinson et al., 2007; Yin et al., 2007b; Menold et al., 2009, 2016), where they were juxtaposed against amphibolite-grade supra-subduction zone ophiolite rocks (Menold et al., 2016). Observations of subduction-fluid metasomatism suggest that the UHP rocks interacted with the subduction channel during metamorphism

and exhumation (Menold et al., 2016; Sievers et al., 2017), thus refuting diapir-flow models. A trench-parallel intra-arc right-slip strike-slip fault developed within the Qilian arc, which is evidenced by the right-lateral shear zone that is exposed in the central Qilian Shan (Fig. 9). Ages from monazite grains included in garnet indicate that this shear zone was operating at ca. 480 Ma (Fig. 13). We envision that this strike-slip fault was similar to the present-day Sumatra strike-slip fault (e.g., Fitch, 1972; Diament et al., 1992). The kinematics of the Qilian strike-slip fault suggest right-lateral obliquity during the subduction of the Qilian Ocean, which is consistent with counterclockwise closure of the Qilian Ocean (Figs. 17C and 18E).

Northward slab rollback at the south-dipping Qilian arc subduction zone can explain three key observations (Fig. 18F): (1) the northeastward-younging trend of arc magmatism throughout the Qilian Shan (e.g., Zuza et al., 2015; Wu et al., 2016, 2017a); (2) the observation that late Ordovician arc plutons intrude Ordovician forearc strata (Figs. 6 and 9); and (3) the position of ophiolite fragments and UHP rocks within and behind the Qilian arc. The arc may have propagated northeast over these features (Figs. 18F and 18G).

By ca. 445–440 Ma, the Tarim–North China cratons collided with the Kunlun-Qaidam continent (Fig. 18F). The timing of collision is not well constrained, but diffuse ca. 445–440 Ma plutonism was followed by relatively little magmatism (e.g., Wu et al., 2017a). Also, the youngest pulse of monazite ages corresponds to this time period (Fig. 13). Silurian strata have been classified as flysch deposits that transition to Devonian molasse rocks. During this colli-

sion, North China's passive-margin strata were juxtaposed against the accretionary wedge, mélange rocks, and ophiolite complex of the Qilian arc (Figs. 9 and 18G). Protracted convergence led to shortening and exhumation of the early Paleozoic granitoids, UHP rocks, and ophiolite suites in the Devonian.

This protracted history of two major ocean-closure events in the Neoproterozoic and early Paleozoic was reactivated in the Cenozoic by focused strike-slip and thrust faulting. The major left-slip faults of northern Tibet parallel Phanerozoic sutures (Taylor and Yin, 2009; Zuza and Yin, 2016; Zuza et al., 2017), and the Haiyuan fault parallels the surface trace of the Qilian-Qinling suture zone (Fig. 1). In addition, the Neoproterozoic north-dipping and early Paleozoic south-dipping subduction zones suggested in this work would provide subduction-mélange channels to focus Cenozoic shortening in northern Tibet. This may explain why significant crustal shortening across the Qilian Shan–Nan Shan thrust belt occurs nearly 1500 km north of the Himalayan collisional front (Fig. 1).

**Cenozoic Deformation and Shortening Estimates**

***Shortening Across the Central Qilian Shan***

Our detailed mapping and structural analysis, presented in the form of several balanced cross sections, provide quantitative estimates of Cenozoic deformation that has affected northern Tibet and the central Qilian Shan. Although cross sections developed from surface geology alone are nonunique tectonic models (e.g., Yin et al., 2010; Judge and Allmendinger, 2011), their uncertainty can be minimized by conform-

ing to direct field observations, including bedding truncations, fault cutoffs, unit juxtapositions, and fault-geometry requirements.

The ultimate goal of our balanced cross-section construction was to restore the sections to an undeformed state to estimate the minimum magnitude of Cenozoic shortening. Because of thick-skinned deformation and large variations/uncertainties in stratigraphic thicknesses, we used the line-balancing method to restore deformation, as opposed to an area balance (Chamberlin, 1923; Mitra and Namson, 1989; Judge and Allmendinger, 2011). Parallel folding was assumed to be accommodated by flexural slip along bedding horizons (Elliott, 1983; Suppe, 1983). Unlike the area balance technique, line-length balancing requires well-constrained knowledge of bedding geometry, particularly at depth below the erosional surface. We used the kink-band technique (Dahlstrom, 1969; Suppe, 1983) to approximate these geometries, and we adhered to the observed map relationships (e.g., the along-strike projection of map relationships aids in interpretation of structures at depth) and empirical cross-section "rules" (Bally et al., 1966; Dahlstrom, 1969; Boyer and Elliott, 1982; Elliott, 1983; Suppe, 1983). By choosing cross-section profile lines along traverses with the best exposure of bedded strata and a high density of bedding measurements, we strived to reduce dip-domain spacing to approximate circular folds. Bedding thickness was kept constant, except where geologic observations showed otherwise (e.g., the pinching out of specific units). When hanging-wall cutoffs were eroded, minimum fault offset was assumed.

The balanced and restored cross-section models are presented in Figures 8 and 9. The deformed-state cross sections adhere to the map-view relationships and structural observations discussed above. The restoration of these sections involved restoring slip along the mapped faults to reposition the middle-to-late Paleozoic unconformity surfaces (e.g., the Carboniferous unconformity horizon) back to horizontal. Pin lines were placed through undeformed strata. Additional cross-section–specific explanations are presented along with each cross section in Figures 8 and 9. A detachment depth of at least ~14 km below Earth's surface was calculated using area-balance methods for the Shule Nan Shan cross section (Fig. 8). Crustal seismicity suggests that the brittle crust in northern Tibet is approximately ~17 km thick (~14 km below sea level; Chu et al., 2009; Sloan et al., 2011; see also GSA Data Repository [see footnote 1]), and therefore the thrust faults may sole into a major décollement at or near the brittle-ductile transition zone (see similar assertion by Lease et al., 2012). We note that geophysical studies

show that multiple horizontal detachment surfaces exist in the crust (Gao et al., 1999, 2013; Ye et al., 2015).

The minimum magnitude of shortening estimated from cross-section restoration is, generally from north to south, 16.5 km (26.5% strain), 15.5 km (47% strain), 6.3 km (38% strain), and 11 km (35% strain) for profiles A-A′, B-B′, C-C′, and D-D′, respectively (Figs. 4, 8, and 9). The summation of these estimates—ignoring section C-C′, which is parallel to section D-D′ (Fig. 9)—suggests that the mapping area accommodated a minimum of 43 km of Cenozoic shortening or ~35% strain.

The section that spans E-E′ in Figure 4 (i.e., across the southern North Qilian Shan range) is totally unconstrained because we have not mapped this region in detail, and very few post-Silurian bedded strata are exposed to constrain fault and fold geometries (Fig. 6). That said, we can provide a first-order shortening estimate by applying the average strain estimate (i.e., 35%) for the central Qilian Shan, taken from sections A-A′ through D-D′, to the ~35-km-long section E-E′ (Fig. 4). This approach yields a minimum shortening magnitude of ~19 km.

The combination of these balanced and restored cross sections across the central Qilian Shan–Nan Shan thrust belt, from Hala Lake in the south to just south of the northern frontal Qilian Shan thrust system (i.e., sections A-A′, B-B′, C-C′, and E-E′, which has a deformed-section length of 118.5 km; Figs. 1 and 4), indicates that the region has accommodated a minimum of ~62 km Cenozoic shortening (~34% strain). The initiation age for this deformation is not constrained. The most direct evidence for shortening initiation is the truncation of Miocene terrestrial strata by thrust faults (Figs. 9, 10E, and 10F). Based on sedimentological evidence, Zhuang et al. (2011) suggested an early to middle Miocene (i.e., ca. 23–15 Ma) deformation initiation age. Using this age yields a long-term shortening rate across the central Qilian Shan-Nan Shan thrust belt of 4.1–2.6 mm yr$^{-1}$. Alternatively, if deformation initiated earlier at ca. 50 Ma, as in southern Qilian Shan and North Qaidam thrust belts (Yin et al., 2008a; Zhuang et al., 2011; Bush et al., 2016), the shortening rate would be ~1.2 mm yr$^{-1}$. Given the range of initiation ages, the central Qilian Shan-Nan Shan thrust belt experienced strain rates of $7.4 \times 10^{-16}$ s$^{-1}$ to $2.2 \times 10^{-16}$ s$^{-1}$.

### Shortening Across the Northeastern Tibetan Plateau

The ~62 km value of Cenozoic shortening (~34% strain) estimated via the restoration of balanced cross sections along our ~118.5 km traverse (Fig. 4) is comparable to regional

shortening estimates across the region (Meyer et al., 1998; Yin and Harrison, 2000). Zuza et al. (2016) estimated a minimum of ~50 km of shortening (53% strain) across the North Qilian thrust system to the north (Fig. 4). The combined results of this study and those of Zuza et al. (2016) suggest that deformation is concentrated along the northern Qilian Shan–Nan Shan margin (53% strain), and the thrust-belt interior has experienced more modest shortening (30%–35% strain). Because the thrust-belt geometry and deformational style to the southwest of Hala Lake appear be similar to our mapping area (Figs. 1 and 4), we suggest that the observed regional ~34% bulk strain can be extrapolated across the entire ~350-km-wide central Qilian Shan–Nan Shan thrust belt (Fig. 1), with the exception of the ~40-km-wide North Qilian Shan thrust system, which has experienced higher strain (Zuza et al., 2016). Following this assumption, we calculated a minimum shortening of ~210 km (38% strain) across the entire central Qilian Shan–Nan Shan thrust belt, from the North Qaidam thrust belt in the south to the Hexi Corridor in the north (Figs. 1 and 4).

The north-south shortening rate across the North Qilian Shan thrust system since ca. 10 Ma is $3.3 \pm 0.6$ mm yr$^{-1}$ (Zuza et al., 2016), which is comparable to shortening rates estimated across other frontal Qilian Shan thrust systems to the east-northeast (e.g., Champagnac et al., 2010; Daout et al., 2016). These relatively high rates account for ~60% of the geodetic shortening rate across the entire Qilian Shan–Nan Shan thrust belt (i.e., 5.5 mm $\pm$ 1.5 yr$^{-1}$; Zhang et al., 2004). The remaining convergence (~2.2 mm/yr) must be accommodated within the interior of the Qilian Shan–Nan Shan thrust belt (Fig. 4). Our shortening estimates suggest geologic time-scale shortening rates across the thrust-belt interior, depending on the initiation age, ranging from ~1.2 mm yr$^{-1}$ (i.e., ca. 50 Ma initiation age) to ~4.1 mm yr$^{-1}$ (i.e., ca. 15 Ma initiation age). Assuming that shortening rates have remained constant during this time, this suggests that shortening may have started prior to ca. 15 Ma (i.e., ~4.1 mm yr$^{-1}$ shortening rate), and possibly before ca. 23 Ma (i.e., ~2.6 mm yr$^{-1}$ shortening rate), because younger deformation initiation ages necessitate shortening rates that are higher than geodetically observed today (i.e., >2.2 mm yr$^{-1}$). However, these rates may have varied in the past, and range-specific cooling and/or fault initiation ages are necessary to further constrain rates. Other fault and shortening rate data sets from across the interior of the Qilian Shan–Nan Shan thrust belt are consistent with rates of <2.5 mm yr$^{-1}$ (Hetzel et al., 2004; W.J. Zheng et al., 2009, 2013; D. Zheng et al., 2010; Yuan et al., 2011; Craddock et al., 2014), whereas

the northern frontal thrust systems generally have shortening rates of >3 mm yr⁻¹ (Champagnac et al., 2010; Zuza et al., 2016; Daout et al., 2016).

The shortening magnitude and rate distribution across the central Qilian Shan–Nan Shan thrust belt corroborate the inference presented by Zuza et al. (2016) that the northern Tibetan Plateau, from the Kunlun fault to the Hexi Corridor (Fig. 1), has experienced bulk north-south shortening of >250 km accommodated by southward underthrusting of the Asian mantle lithosphere beneath the northern margin of the plateau and a similar magnitude of upper-crustal shortening and pure shear crustal thickening. Strain observed away from the margins of the northeastern plateau is >35%, which is enough to thicken an initially ~40-km-thick crust to the observed present-day crustal thickness (i.e., 65–55 km; Yue et al., 2012; Ye et al., 2015) by distributed crustal shortening and pure shear thickening. Along the northern plateau margin, localized higher strain (>53%) results from southward underthrusting of the Asian mantle lithosphere to a position beneath the northern Qaidam Basin (e.g., Feng et al., 2014; Ye et al., 2015).

Our refined shortening estimates are a step toward reconciling the apparent disparity between India-Asia convergence and crustal shortening across the Himalayan-Tibetan orogen (e.g., van Hinsbergen et al., 2011; Webb, 2013; Yakovlev and Clark, 2014; Ingalls et al., 2016). There has been 2000–2500 km of convergence between India and Asia since the onset of collision at 65–55 Ma (e.g., Molnar and Tapponnier, 1975; Dewey et al., 1989; Le Pichon et al., 1992; Molnar and Stock, 2009; Zhu et al., 2005; van Hinsbergen et al., 2011). The documented crustal shortening across the Himalayan-Tibetan orogen is significantly less: shortening estimates are 600–1300 km in the Himalaya (DeCelles et al., 2002; Robinson et al., 2006; Yin et al., 2010; Long et al., 2011; Webb, 2013) and 300–400 km across all of Tibet (e.g., Yakovlev and Clark, 2014). However, integration of the shortening estimates presented here with existing syntheses suggests that that observed minimum shortening across the Himalayan-Tibetan orogen may be up to 1900 km, which is nearly compatible with the 2000–2500 km of convergence between India and Asia predicted by plate circuit reconstructions and paleomagnetic data (e.g., Molnar and Stock, 2009; van Hinsbergen et al., 2011).

### Implications for the Western Termination of the Haiyuan Fault

The Shule Nan Shan is the western termination of the left-slip Haiyuan fault, and strike-slip faulting, shear, or offset is not observed to the west of this range (Figs. 1, 4, 8, and 19; Burchfiel et al., 1989; Meyer et al., 1998; Duvall et al.,

2013; Zuza and Yin, 2016). The range-bounding SSW-directed thrust faults in Shule Nan Shan, Tuo Lai Nan Shan, and Tuo Lai Shan ranges merge to the southeast with the Haiyuan fault (Fig. 4). This geometric relationship between the strike-slip and thrust faults suggests a kinematic linkage between shortening and strike-slip faulting (i.e., there are no truncational relationships to suggest one fault system crosscuts the other). Because left-lateral motion ceases to the west of the Shule Nan Shan, all of the lateral motion must be accommodated within these termination thrust faults (Fig. 19). Thus, the dip-slip shortening documented in this study across each range-bounding thrust system can be used as an indirect estimate for the maximum magnitude of left-slip offset along the western segment of the Haiyuan fault. This is a maximum estimate, because these thrust faults may accommodate more dip-slip shortening that is not a component of Haiyuan-fault–derived left-lateral shear (Fig. 19).

The SW-directed shortening documented in each range is ~10–15 km (Figs. 8 and 9), which, given the angle between shortening and the Haiyuan fault, equals a total of ~11 km of left-lateral offset (Fig. 19). This preliminary estimate of fault slip along the Haiyuan fault provides constraints on the slip rate and fault offset gradients. The central segment of the Haiyuan

fault experienced ~95 km of left-lateral offset (Gaudemer et al., 1995) and has an estimated global positioning system–based slip rate of 11–19 mm yr⁻¹ (Gaudemer et al., 1995; Lasserre et al., 1999, 2002). If the Haiyuan fault initiated at ca. 17–12 Ma in the west (Duvall et al., 2013), our estimates suggest that the local slip rate is <1 mm yr⁻¹ (i.e., ~11 km divided by 17–12 Ma). Thus, the offset magnitude and slip rate decrease significantly from the central fault segment to its western termination in the Shule Nan Shan (e.g., Zuza and Yin, 2016). This offset pattern is inconsistent with extrusion-fault models for the Haiyuan fault (e.g., Tapponnier et al., 1982; Peltzer and Tapponnier, 1988; Avouac and Tapponnier, 1993; Cheng et al., 2015). Instead, these observations are consistent with models where the Haiyuan fault either assists with strain transfer between thrust systems (e.g., Burchfiel et al., 1991; Zhang et al., 1991; Duvall and Clark, 2010) or accommodates clockwise rotation of northern Tibet and bookshelf faulting (e.g., England and Molnar, 1990; Zuza and Yin, 2016).

### CONCLUSIONS

The Qilian Shan, North Qaidam, and Qaidam Basin of northern Tibet experienced two major arc/collisional events in the Neoproterozoic and early Paleozoic. Through an integrated investi-



**Figure 19. Sketched relationship between dip-slip shortening and strike-slip faulting at the western termination of the left-slip Haiyuan fault. (A) Fault map of the western termination structures of the Haiyuan fault, including the range-bounding dip-slip thrusts faults in Shule Nan Shan (a), Tuo Lai Nan Shan (b), and Tuo Lai Shan (c) ranges. Note that no strike-slip offset is observed west of the Shule Nan Shan. (B) Simplified geometric relationships between Haiyuan strike-slip offset ($x$) and shortening ($sh$) across the central Qilian Shan thrust faults, assuming some angle ($\theta$) between the strikes of the thrust faults and the Haiyuan fault. Because no strike-slip shear is observed to the west of the Shule Nan Shan, all of $x$ must be accommodated within these termination-thrust faults. The observed dip-slip shortening across each range (e.g., Figs. 8–9) translates to a summed maximum strike-slip fault offset of ~11 km. Inset shows vector relationships between shortening ($sh$) and strike-slip offset ($x$) directions; $l_i$ and $l_f$ are the initial and final lengths of a deformed section, respectively, at a termination-thrust fault.**
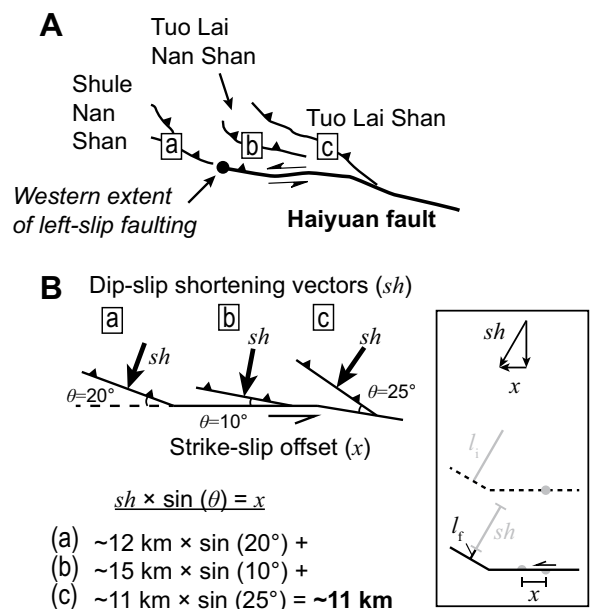
gation of the magmatic and deformational history of the central Qilian Shan, together with existing work across northern Tibet, we have developed a coherent tectonic model that describes the evolution of the southern margins of the continuous Tarim–North China craton from ca. 1.0 Ga to the present.

(1) Early Neoproterozoic subduction accommodated the convergence and collision between the South Tarim–Qaidam and North Tarim–North China continents. Arc-related plutons associated with this subduction system (ca. 1.0–0.9 Ga) are exposed across the Qilian Shan, North Qaidam, Tarim, and Tian Shan regions.

(2) Late Neoproterozoic rifting partially separated a peninsular Qaidam from North China and opened the Qilian Ocean as an embayed marginal sea; this separation broadly followed the trace of the early Neoproterozoic suture zone.

(3) South-dipping subduction along the northern margin of the Kunlun-Qaidam continent initiated in the Cambrian, which led to the formation of the Yushigou supra-subduction zone ophiolite (which links along strike with the supra-subduction zone Aoyougou and Dongcaohe ophiolites) and the formation of the Qilian arc.

(4) Subduction, arc magmatism, and the convergence between Qaidam and North China continued throughout the Ordovician, with a trench-parallel intra-arc strike-slip fault system that is presently represented by the high-grade metamorphic rocks showing a pervasive right-lateral shear sense.

(5) The closure of the Qilian Ocean occurred following the counterclockwise rotation of the peninsular Kunlun-Qaidam continent toward North China, which is supported by the right-lateral kinematics of the intra-arc strike-slip fault and the westward tapering map-view geometry of Silurian flysch basins. Collision occurred at ca. 445–440 Ma, which led to widespread plutonism across the Qilian Shan.

This tectonic model implies the parallel closure of two oceans along the Qilian suture zone since ca. 1.0 Ga (Wu et al., 2016). In addition, the Qilian Ocean was not the Proto-Tethys (i.e., the earliest through-going ocean separating Gondwana from Laurasia) as suggested by earlier studies, but rather represented a smaller marginal sea along the southern margin of the Laurasian continent.

Cenozoic deformation resulting from India-Asia collision and convergence is focused along these sites of repeated past ocean closure. The major left-slip faults parallel these sutures, and Cenozoic shortening and continental underthrusting may have been assisted by the subduction-mélange channels. We document a

minimum of 210 km of Cenozoic north-south shortening across the Qilian Shan–Nan Shan thrust belt, and we extrapolate this estimate to suggest that northern Tibet, between the Kunlun fault in the south and the Hexi Corridor in the north, has accommodated >250–350 km of Cenozoic shortening. The observed strain distribution across the northern Tibetan Plateau—i.e., >50% across the plateau margin and >35% within the Qilian Shan–Nan Shan thrust belt interior—suggests that the dominant processes of plateau construction operating in northern Tibet are a combination of distributed crustal shortening, pure shear thickening, and southward underthrusting of the Asian mantle lithosphere. Our refined shortening estimates represent a step toward reconciling the strain deficit between the 2000–2500 km of convergence between India and Asia (e.g., Molnar and Stock, 2009; van Hinsbergen et al., 2011) and crustal shortening observed across the Himalayan-Tibetan orogen (Yakovlev and Clark, 2014; Ingalls et al., 2016). The integration of our shortening estimates with existing syntheses suggests that at least ~1900 km of Cenozoic upper-crustal shortening has been accommodated across the Himalayan-Tibetan orogen.

## REFERENCES CITED

Aleinikoff, J.N., Schenck, W.S., Plank, M.O., Srogi, L., Fanning, C.M., Kamo, S.L., and Bosbyshell, H., 2006, Deciphering igneous and metamorphic events in high-grade rocks of the Wilmington complex, Delaware: Morphology, cathodoluminescence and backscattered electron zoning, and SHRIMP U-Pb geochronology of zircon and monazite: Geological Society of America Bulletin, v. 118, no. 1–2, p. 39–64, https://doi.org/10.1130/B25659.1.

Argand, E., 1924, La tectonique de l'Asie, *in* Congrès Géologique International, Comptes Rendus de la XIIe Session: Liege, Vaillant-Carmanne.

Avouac, J.P., and Tapponnier, P., 1993, Kinematic model of active deformation in Central Asia: Geophysical Re-search Letters, v. 20, no. 10, p. 895–898, https://doi.org/10.1029/93GL00128.

Badarch, G., Cunningham, W.D., and Windley, B.F., 2002, A new terrane subdivision for Mongolia: Implications for the Phanerozoic crustal growth of Central Asia: Journal of Asian Earth Sciences, v. 21, no. 1, p. 87–110, https://doi.org/10.1016/S1367-9120(02)00017-2.

Bally, A.W., Gordy, P.L., and Stewart, G.A., 1966, Structure, seismic data, and orogenic evolution of southern Canadian Rocky Mountains: Bulletin of Canadian Petroleum Geology, v. 14, no. 3, p. 337–381.

Bird, P., 1991, Lateral extrusion of lower crust from under high topography in the isostatic limit: Journal of Geophysical Research, v. 96, p. 10,275–10,286, https://doi.org/10.1029/91JB00370.

Biske, Y.S., and Seltmann, R., 2010, Paleozoic Tian-Shan as a transitional region between the Rheic and Urals-Turkestan Oceans: Gondwana Research, v. 17, p. 602–613, https://doi.org/10.1016/j.gr.2009.11.014.

Bosse, V., Boulvais, P., Gautier, P., et al., 2009, Fluid-induced disturbance of the monazite Th-Pb chronometer: In situ dating and element mapping in pegmatites from the Rhodope (Greece, Bulgaria): Chemical Geology, v. 261, no. 3–4, p. 286–302, https://doi.org/10.1016/j.chemgeo.2008.10.025.

Bovet, P.M., Ritts, B.D., Gehrels, G., Abbink, A.O., Darby, B., and Hourigan, J., 2009, Evidence of Miocene crustal shortening in the north Qilian Shan from Cenozoic stratigraphy of the western Hexi Corridor, Gansu Province, China: American Journal of Science, v. 309, p. 290–329, https://doi.org/10.2475/00.4009.02.

Boyer, S.E., and Elliott, D., 1982, Thrust systems: American Association of Petroleum Geologists Bulletin, v. 66, p. 1196–1230.

Burchfiel, B.C., and Chen, Z., 2012, Tectonics of the Southeastern Tibetan Plateau and its Adjacent Foreland: Geological Society of America Memoir 210, 231 p.

Burchfiel, B.C., Quidong, D., Molnar, P., Royden, L., Yipeng, W., Peizhen, Z., and Weiqi, Z., 1989, Intracrustal detachment within zones of continental deformation: Geology, v. 17, no. 8, p. 748–752, https://doi.org/10.1130/0091-7613(1989)017<0448:IDWZOC>2.3.CO;2.

Burchfiel, B.C., Zhang, P., Wang, Y., Zhang, W., Song, F., Deng, Q., Molnar, P., and Royden, L., 1991, Geology of the Haiyuan fault zone, Ningxia-Hui Autonomous Region, China, and its relation to the evolution of the northeastern margin of the Tibetan Plateau: Tectonics, v. 10, no. 6, p. 1091–1110, https://doi.org/10.1029/90TC02685.

Bush, M.A., Saylor, J.E., Horton, B.K., and Nie, J., 2016, Growth of the Qaidam Basin during Cenozoic exhumation in the northern Tibetan Plateau: Inferences from depositional patterns and multiproxy detrital provenance signatures: Lithosphere, v. 8, no. 1, p. 58–82, https://doi.org/10.1130/L449.1.

Catlos, E.J., Gilley, L.D., and Harrison, T.M., 2002, Interpretation of monazite ages obtained via in situ analysis: Chemical Geology, v. 188, no. 3–4, p. 193–215, https://doi.org/10.1016/S0009-2541(02)00099-2.

Chamberlin, R.T., 1923, On the crustal shortening of the Colorado Rockies: American Journal of Science, v. 5–6, no. 33, p. 215–221, https://doi.org/10.2475/ajs.s5-6.33.215.

Champagnac, J.D., Yuan, D.Y., Ge, W.P., Molnar, P., and Zheng, W.J., 2010, Slip rate at the north-eastern front of the Qilian Shan, China: Terra Nova, v. 22, p. 180–187, https://doi.org/10.1111/j.1365-3121.2010.00932.x.

Chapman, A.D., Jacobson, C.E., Ernst, W.G., Grove, M., Dumitru, T., Hourigan, J., and Ducea, M.N., 2016, Assembling the world's type shallow subduction complex: Detrital zircon geochronologic constraints on the origin of the Nacimiento block, central California Coast Ranges: Geosphere, v. 12, no. 2, p. 533–557, https://doi.org/10.1130/GES01257.1.

Chen, X., Yin, A., Gehrels, G.E., Cowgill, E.S., Grove, M., Harrison, T.M., and Wang, X.-F., 2003, Two phases of Mesozoic north-south extension in the eastern Altyn Tagh range, northern Tibetan Plateau: Tectonics, v. 22, 1053, https://doi.org/10.1029/2001TC001336.

Cheng, F., Jolivet, M., Dupont-Nivet, G., Wang, L., Yu, X., and Guo, Z., 2015, Lateral extrusion along the Altyn

Tagh fault, Qilian Shan (NE Tibet): Insight from a 3D crustal budget: Terra Nova, v. 27, no. 6, p. 416–425, https://doi.org/10.1111/ter.12173.

Cheng, H., Lu, T., and Cao, D., 2016, Coupled Lu-Hf and Sm-Nd geochronology constrains blueschist-facies metamorphism and closure timing of the Qilian Ocean in the North Qilian orogen: Gondwana Research, v. 34, p. 99–108, https://doi.org/10.1016/j.gr.2016.03.008.

Chu, R., Zhu, L., and Helmberger, D.V., 2009, Determination of earthquake focal depths and source time functions in Central Asia using teleseismic P waveforms: Geophysical Research Letters, v. 36, no. 17, L17317, https://doi.org/10.1029/2009GL039494.

Clark, M.K., and Royden, L.H., 2000, Topographic ooze: Building the eastern margin of Tibet by lower crustal flow: Geology, v. 28, p. 703–706, https://doi.org/10.1130/0091-7613(2000)28<703:TOBTEM>2.0.CO;2.

Clift, P., and Vannucchi, P., 2004, Controls on tectonic accretion versus erosion in subduction zones: Implications for the origin and recycling of the continental crust: Reviews of Geophysics, v. 42, no. 2, RG2001, https://doi.org/10.1029/2003RG000127.

Coleman, D.S., Gray, W., and Glazner, A.F., 2004, Rethinking the emplacement and evolution of zoned plutons: Geochronologic evidence for incremental assembly of the Tuolumne intrusive suite, California: Geology, v. 32, no. 5, p. 433–436, https://doi.org/10.1130/G20220.1.

Cooper, F.J., Platt, J.P., Anczkiewicz, R., and Whitehouse, M.J., 2010, Footwall dip of a core complex detachment fault: Thermobarometric constraints from the northern Snake Range (Basin and Range, USA): Journal of Metamorphic Geology, v. 28, no. 9, p. 997–1020, https://doi.org/10.1111/j.1525-1314.2010.00907.x.

Cowgill, E., Yin, A., Feng, W.X., and Qing, Z., 2000, Is the North Altyn fault part of a strike-slip duplex along the Altyn Tagh fault system?: Geology, v. 28, no. 3, p. 255–258, https://doi.org/10.1130/0091-7613(2000)28<255:ITNAFP>2.0.CO;2.

Cowgill, E., Yin, A., Harrison, T.M., and Xiao-Feng, W., 2003, Reconstruction of the Altyn Tagh fault based on U-Pb geochronology: Role of back thrusts, mantle sutures, and heterogeneous crustal strength in forming the Tibetan Plateau: Journal of Geophysical Research–Solid Earth, v. 108, no. B7, 2346, https://doi.org/10.1029/2002JB002080.

Cowgill, E., Yin, A., Arrowsmith, J.R., Feng, W.X., and Shuanhong, Z., 2004a, The Akato Tagh bend along the Altyn Tagh fault, northwest Tibet 1: Smoothing by vertical-axis rotation and the effect of topographic stresses on bend-flanking faults: Geological Society of America Bulletin, v. 116, no. 11–12, p. 1423–1442, https://doi.org/10.1130/B25359.1.

Cowgill, E., Arrowsmith, J.R., Yin, A., Xiaofeng, W., and Zhengle, C., 2004b, The Akato Tagh bend along the Altyn Tagh fault, northwest Tibet 2: Active deformation and the importance of transpression and strain hardening within the Altyn Tagh system: Geological Society of America Bulletin, v. 116, no. 11–12, p. 1443–1464, https://doi.org/10.1130/B25360.1.

Cowgill, E., Gold, R.D., Xuanhua, C., Xiao-Feng, W., Arrowsmith, J.R., and Southon, J., 2009, Low Quaternary slip rate reconciles geodetic and geologic rates along the Altyn Tagh fault, northwestern Tibet: Geology, v. 37, no. 7, p. 647–650, https://doi.org/10.1130/G25623A.1.

Craddock, W.H., Kirby, E., Zhang, H., Clark, M.K., Champagnac, J.D., and Yuan, D., 2014, Rates and style of Cenozoic deformation around the Gonghe Basin, northeastern Tibetan Plateau: Geosphere, v. 10, p. 1255–1282, https://doi.org/10.1130/GES01024.1.

Dahlstrom, C.D.A., 1969, Balanced cross section: Canadian Journal of Earth Sciences, v. 6, p. 743–757, https://doi.org/10.1139/e69-069.

Dan, W., Li, X.H., Guo, J., Liu, Y., and Wang, X.C., 2012, Paleoproterozoic evolution of the eastern Alxa block, westernmost North China: Evidence from in situ zircon U-Pb dating and Hf-O isotopes: Gondwana Research, v. 21, no. 4, p. 838–864, https://doi.org/10.1016/j.gr.2011.09.004.

Dang, J., 2011, Geochemical characteristics and tectonic implications of Jinfosi granite in north Qilian: Gansu Geology, v. 20, p. 40–44.

Daout, S., Jolivet, R., Lasserre, C., Doin, M.P., Barbot, S., Tapponnier, P., Peltzer, G., Socquet, A., and Sun, J., 2016, Along-strike variations of the partitioning of convergence across the Haiyuan fault system detected by InSAR: Geophysical Journal International, v. 205, no. 1, p. 536–547, https://doi.org/10.1093/gji/ggw028.

DeCelles, P.G., Robinson, D.M., and Zandt, G., 2002, Implications of shortening in the Himalayan fold-thrust belt for uplift of the Tibetan Plateau: Tectonics, v. 21, no. 6, p. 12-1–12-25, https://doi.org/10.1029/2001TC001322.

Dewey, J.F., 1988, Extensional collapse of orogens: Tectonics, v. 7, no. 6, p. 1123–1139, https://doi.org/10.1029/TC007i006p01123.

Dewey, J.F., and Bird, J.M., 1970, Mountain belts and the new global tectonics: Journal of Geophysical Research, v. 75, p. 2625–2647, https://doi.org/10.1029/JB075i014p02625.

Dewey, J.F., and Burke, K.C., 1973, Tibetan, Variscan, and Precambrian basement reactivation: Products of continental collision: The Journal of Geology, v. 81, no. 6, p. 683–692, https://doi.org/10.1086/627920.

Dewey, J.F., Cande, S., and Pitman, W.C., 1989, Tectonic evolution of the India/Eurasia collision zone: Eclogae Geologicae Helvetiae, v. 82, no. 3, p. 717–734.

DeWolf, C.P., Beshaw, N., and O'Nions, R.K., 1993, A metamorphic history from micro-scale $^{207}Pb/^{206}Pb$ chronometry of Archean monazite: Earth and Planetary Science Letters, v. 120, p. 207–220, https://doi.org/10.1016/0012-821X(93)90240-A.

Diament, M., Harjono, H., and Karta, K., 1992, Mentawai fault zone off Sumatra: A new key to the geodynamics of western Indonesia: Geology, v. 20, no. 3, p. 259–262, https://doi.org/10.1130/0091-7613(1992)020<0259:MFZOSA>2.3.CO;2.

Dong, Y., Zhang, G., Neubauer, F., Liu, X., Genser, J., and Hauzenberger, C., 2011, Tectonic evolution of the Qinling orogen, China: Review and synthesis: Journal of Asian Earth Sciences, v. 41, no. 3, p. 213–237, https://doi.org/10.1016/j.jseaes.2011.03.002.

Du, Y., Wang, J., Han, X., and Shi, G.R., 2003, From flysch to molasse-sedimentary and tectonic evolution of late Caledonian–early Hercynian foreland basin in North Qilian Mountains: Journal of China University of Geosciences, v. 14, no. 1, p. 1–7.

Duvall, A.R., and Clark, M.K., 2010, Dissipation of fast strike-slip faulting within and beyond northeastern Tibet: Geology, v. 38, no. 3, p. 223–226, https://doi.org/10.1130/G30711.1.

Duvall, A.R., Clark, M.K., Kirby, E., Farley, K.A., Craddock, W.H., Li, C., and Yuan, D.Y., 2013, Low-temperature thermochronometry along the Kunlun and Haiyuan faults, NE Tibetan Plateau: Evidence for kinematic change during late-stage orogenesis: Tectonics, v. 32, no. 5, p. 1190–1211, https://doi.org/10.1002/tect.20072.

Elliott, D., 1983, The construction of balanced cross-sections: Journal of Structural Geology, v. 5, no. 2, p. 101, https://doi.org/10.1016/0191-8141(83)90035-4.

England, P., and Houseman, G., 1986, Finite strain calculations of continental deformation: 2. Comparison with the India-Asia collision zone: Journal of Geophysical Research, v. 91, no. B3, p. 3664–3676, https://doi.org/10.1029/JB091iB03p03664.

England, P., and Houseman, G., 1989, Extension during continental convergence, with application to the Tibetan Plateau: Journal of Geophysical Research–Solid Earth, v. 94, no. B12, p. 17,561–17,579, https://doi.org/10.1029/JB094iB12p17561.

England, P., and Molnar, P., 1990, Right-lateral shear and rotation as the explanation for strike-slip faulting in eastern Tibet: Nature, v. 344, no. 6262, p. 140–142, https://doi.org/10.1038/344140a0.

England, P., and Searle, M., 1986, The Cretaceous–Tertiary deformation of the Lhasa block and its implications for crustal thickening in Tibet: Tectonics, v. 5, no. 1, p. 1–14, https://doi.org/10.1029/TC005i001p00001.

Evans, B.W., 1990, Phase relations of epidote-blueschists: Lithos, v. 25, no. 1–3, p. 3–23, https://doi.org/10.1016/0024-4937(90)90003-J.

Feng, M., Kumar, P., Mechie, J., Zhao, W., Kind, R., Su, H., Xue, G., Shi, D., and Qian, H., 2014, Structure of

the crust and mantle down to 700 km depth beneath the East Qaidam basin and Qilian Shan from P and S receiver functions: Geophysical Journal International, v. 199, p. 1416–1429, https://doi.org/10.1093/gji/ggu335.

Fitch, T.J., 1972, Plate convergence, transcurrent faults, and internal deformation adjacent to southeast Asia and the western Pacific: Journal of Geophysical Research, v. 77, no. 23, p. 4432–4460, https://doi.org/10.1029/JB077i023p04432.

Foster, G., Kinny, P., Vance, D., Prince, C., and Harris, N., 2000, The significance of monazite U-Th-Pb age data in metamorphic assemblages; a combined study of monazite and garnet chronometry: Earth and Planetary Science Letters, v. 181, no. 3, p. 327–340, https://doi.org/10.1016/S0012-821X(00)00212-0.

Gansu Bureau of Geology, 1974, Second Regional Geological Surveying Team of the Bureau of Geology of Gansu Province: Geologic Map of Qilian Mountains and Its Directions: Gansu Bureau of Geology, scale 1:200,000.

Gansu Geological Bureau, 1989, Regional Geology of Gansu Province: Beijing, Geological Publishing House, 692 p. [in Chinese].

Gao, R., Cheng, X., and Wu, G., 1999, Lithospheric structure and geodynamic model of the Golmud-Ejn transect in northern Tibet, *in* Macfarlane, A., et al., eds., Himalaya and Tibet: Mountain Roots to Mountain Tops: Geological Society of America Special Paper 328, p. 9–17.

Gao, R., Wang, H., Yin, A., Dong, S., Kuang, Z., Zuza, A.V., Li, W., and Xiong, X., 2013, Tectonic development of the northeastern Tibetan Plateau as constrained by high-resolution deep seismic-reflection data: Lithosphere, v. 5, no. 6, p. 555–574, https://doi.org/10.1130/L293.1.

Gasser, D., Bruand, E., Rubatto, D., and Stüwe, K., 2012, The behaviour of monazite from greenschist facies phyllites to anatectic gneisses: An example from the Chugach metamorphic complex, southern Alaska: Lithos, v. 134–135, p. 108–122, https://doi.org/10.1016/j.lithos.2011.12.003.

Gaudemer, Y., Tapponnier, P., Meyer, B., Peltzer, G., Shunmin, G., Zhitai, C., Huagung, D., and Cifuentes, I., 1995, Partitioning of crustal slip between linked, active faults in the eastern Qilian Shan, and evidence for a major seismic gap, the 'Tianzhu gap,' on the western Haiyuan fault, Gansu (China): Geophysical Journal International, v. 120, p. 599–645, https://doi.org/10.1111/j.1365-246X.1995.tb01842.x.

Gehrels, G.E., Yin, A., and Wang, X.F., 2003a, Detrital zircon geochronology of the northeastern Tibet: Geological Society of America Bulletin, v. 115, p. 881–896, https://doi.org/10.1130/0016-7606(2003)115<0881:DGOTNT>2.0.CO;2.

Gehrels, G.E., Yin, A., and Wang, X.F., 2003b, Magmatic history of the Altyn Tagh, Nan Shan, and Qilian Shan region of western China: Journal of Geophysical Research, v. 108, 2423, https://doi.org/10.1029/2002JB001876.

Gehrels, G.E., Kapp, P., DeCelles, P., et al., 2011, Detrital zircon geochronology of pre-Tertiary strata in the Tibetan-Himalayan orogen: Tectonics, v. 30, no. 5, p. 1–27, https://doi.org/10.1029/2011TC002868.

Gong, J.H., Zhang, J.X., and Yu, S.Y., 2011, The origin of Longshoushan Group and associated rocks in the southern part of the Alxa block: Constraint from LA-ICP-MS U-Pb zircon dating: Acta Petrologica et Mineralogica, v. 30, no. 5, p. 795–818.

Grove, M., Jacobson, C. E., Barth, A. P., and Vucic, A., 2003, Temporal and spatial trends of Late Cretaceous–Early Tertiary underplating of Pelona and related schist beneath southern California and southwestern Arizona, *in* Johnson, S.E., Paterson, S.R., Fletcher, J.M., Girty, G.H., Kimbrough, D.L., and Martín-Barajas, A., eds., Tectonic Evolution of Northwestern Mexico and the Southwestern USA: Geological Society of America Special Paper 374, p. 381–406, https://dx.doi.org/10.1130/0-8137-2374-4.381.

Guo, Z.J., Zhang, Z., and Wang, J., 1999, Sm-Nd isochron age of ophiolite along northern margin of Altun Tagh Mountain and its tectonic significance: Chinese Science Bulletin, v. 44, no. 5, p. 456–458, https://doi.org/10.1007/BF02977887.

Guo, Z.J., Yin, A., Robinson, A., and Jia, C.Z., 2005, Geochronology and geochemistry of deep-drill-core samples from the basement of the central Tarim Basin: Journal of Asian Earth Sciences, v. 25, no. 1, p. 45–56, https://doi.org/10.1016/j.jseaes.2004.01.016.

Han, G., Liu, Y., Neubauer, F., Genser, J., Li, W., Zhao, Y., and Liang, C., 2011, Origin of terranes in the eastern Central Asian orogenic belt, NE China: U-Pb ages of detrital zircons from Ordovician–Devonian sandstones, North Da Xing'an Mts: Tectonophysics, v. 511, p. 109–124, https://doi.org/10.1016/j.tecto.2011.09.002.

Harrison, T.M., Copeland, P., Kidd, W.S.F., and Yin, A., 1992, Raising Tibet: Science, v. 255, no. 5052, p. 1663–1670, https://doi.org/10.1126/science.255.5052.1663.

Harrison, T.M., McKeegan, K.D., and LeFort, P., 1995, Detection of inherited monazite in the Manaslu leucogranite by $^{208}Pb/^{232}Th$ ion microprobe dating: Crystallization age and tectonic implications: Earth and Planetary Science Letters, v. 133, no. 3–4, p. 271–282, https://doi.org/10.1016/0012-821X(95)00091-P.

Harrison, T.M., Grove, M., and Lovera, O.M., 1997, New insights into the origin of two contrasting Himalayan granite belts: Geology, v. 25, p. 899–902, https://doi.org/10.1130/0091-7613(1997)025<0899:NIITOO>2.3.CO;2.

Harrison, T.M., Grove, M., McKeegan, K.D., Coath, C.D., Lovera, O.M., and Le Fort, P., 1999, Origin and episodic emplacement of the Manaslu intrusive complex, central Himalaya: Journal of Petrology, v. 40, p. 3–19, https://doi.org/10.1093/petroj/40.1.3.

He, S., Wang, H., Chen, J., Xu, X., Zhang, H., Ren, G., and Yu, J., 2007, LA-ICP-MS U-Pb zircon geochronology of basic dikes within Maxianshan rock group in the central Qilian orogenic belt and its tectonic implications: Journal of China University of Geosciences, v. 18, no. 1, p. 19–29, https://doi.org/10.1016/S1002-0705(07)60015-6.

Henry, D.J., Guidotti, C.V., and Thomson, J.A., 2005, The Ti-saturation surface for low-to-medium pressure metapelitic biotites: Implications for geothermometry and Ti-substitution mechanisms: The American Mineralogist, v. 90, no. 2–3, p. 316–328, https://doi.org/10.2138/am.2005.1498.

Hetzel, R., Tao, M., Stokes, S., Niedermann, S., Ivy-Ochs, S., Gao, B., Stecker, M.R., and Kubik, P.W., 2004, Late Pleistocene/Holocene slip rate of the Zhangye thrust (Qilian Shan, China) and implications for the active growth of the northeastern Tibetan Plateau: Tectonics, v. 23, no. 6, TC6006, https://doi.org/10.1029/2004TC001653.

Heubeck, C., 2001, Assembly of Central Asia during the middle and late Paleozoic, *in* Hendrix, M.S., and Davis, G.A., eds., Paleozoic and Mesozoic Tectonic Evolution of Central Asia: From Continental Assembly to Intracontinental Deformation: Geological Society of America Memoir 194, p. 1–22, https://doi.org/10.1130/0-8137-1194-0.1.

Holland, T., and Blundy, J., 1994, Non-ideal interactions in calcic amphiboles and their bearing on amphibole-plagioclase thermometry: Contributions to Mineralogy and Petrology, v. 116, no. 4, p. 433–447, https://doi.org/10.1007/BF00310910.

Holland, T., and Powell, R., 1998, An internally consistent thermodynamic dataset for phases of petrological interest: Journal of Metamorphic Geology, v. 16, p. 309–343, https://doi.org/10.1111/j.1525-1314.1998.00140.x.

Holland, T., and Powell, R., 2011, An improved and extended internally consistent thermodynamic dataset for phases of petrological interest, involving a new equation of state for solids: Journal of Metamorphic Geology, v. 29, no. 3, p. 333–383, https://doi.org/10.1111/j.1525-1314.2010.00923.x.

Hou, Q., Zhao, Z., Zhang, H., Zhang, B., and Chen, Y., 2006, Indian Ocean-MORB-type isotopic signature of Yushigou ophiolite in North Qilian Mountains and its implications: Science in China, ser. D, v. 49, no. 6, p. 561–572, https://doi.org/10.1007/s11430-006-0561-8.

Hsü, K.J., Guitang, P., and Şengör, A.M.C., 1995, Tectonic evolution of the Tibetan Plateau: A working hypothesis based on the archipelago model of orogenesis: International Geology Review, v. 37, no. 6, p. 473–508, https://doi.org/10.1080/00206819509465414.

Hu, A., Jahn, B.M., Zhang, G., Chen, Y., and Zhang, Q., 2000, Crustal evolution and Phanerozoic crustal growth in northern Xinjiang: Nd isotopic evidence. Part I. Isotopic characterization of basement rocks: Tectonophysics, v. 328, no. 1–2, p. 15–51, https://doi.org/10.1016/S0040-1951(00)00176-1.

Hu, N.G., Xu, A.D., and Yang, J.X., 2005, Characteristics and tectonic environment of Zhigoumen pluton in Longshoushan area: Journal of Earth Sciences and Environment, v. 27, p. 5–11 [in Chinese with English abstract].

Hu, X., Garzanti, E., Moore, T., and Raffi, I., 2015, Direct stratigraphic dating of India-Asia collision onset at the Selandian (middle Paleocene, 59±1 Ma): Geology, v. 43, no. 10, p. 859–862, https://doi.org/10.1130/G36872.1.

Huang, H., Huang, Q., and Ma, Y., 1996, Geology of the Qaidam Basin and its Petroleum Prediction: Beijing, Geological Publishing House, 257 p. [in Chinese].

Huo, Y.L., and Tan, S.D., 1995, Exploration Case History and Petroleum Geology in Jiuquan Continental Basin: Beijing, China, Petroleum Industry Press, 211 p.

Ingalls, M., Rowley, D.B., Currie, B., and Colman, A.S., 2016, Large-scale subduction of continental crust implied by India-Asia mass-balance calculation: Nature Geoscience, v. 9, no. 11, p. 848–853, https://doi.org/10.1038/ngeo2806.

Jahn, B.M., Capdevila, R., Liu, D.Y., Vernon, A., and Badarch, G., 2004, Sources of Phanerozoic granitoids in the transect Bayanhongor–Ulaan Baatar, Mongolia: Geochemical and Nd isotopic evidence, and implications for Phanerozoic crustal growth: Journal of Asian Earth Sciences, v. 23, p. 629–653, https://doi.org/10.1016/S1367-9120(03)00125-1.

Judge, P.A., and Allmendinger, R.W., 2011, Assessing uncertainties in balanced cross sections: Journal of Structural Geology, v. 33, no. 4, p. 458–467, https://doi.org/10.1016/j.jsg.2011.01.006.

Kapp, P., Yin, A., Harrison, T.M., and Ding, L., 2005, Cretaceous–Tertiary shortening, basin development, and volcanism in central Tibet: Geological Society of America Bulletin, v. 117, no. 7, p. 865–878, https://doi.org/10.1130/B25595.1.

Kapp, P., DeCelles, P.G., Gehrels, G.E., Heizler, M., and Ding, L., 2007, Geological records of the Lhasa-Qiangtang and Indo-Asian collisions in the Nima area of central Tibet: Geological Society of America Bulletin, v. 119, no. 7–8, p. 917–933, https://doi.org/10.1130/B26033.1.

Käßner, A., Ratschbacher, L., Pfänder, J.A., Hacker, B.R., Zack, G., Sonntag, B., Khan, J., Stanek, K.P., Gadoev, M., and Oimahmadov, I., 2017, Proterozoic–Mesozoic history of the Central Asian orogenic belt in the Tajik and southwestern Kyrgyz Tian Shan: U-Pb, $^{40}Ar/^{39}Ar$, and fission-track geochronology and geochemistry of granitoids: Geological Society of America Bulletin, v. 129, no. 3–4, p. 281–303, https://doi.org/10.1130/B31466.1.

Kind, R., Yuan, X., Saul, J., et al., 2002, Seismic images of crust and upper mantle beneath Tibet: Evidence for Eurasian plate subduction: Science, v. 298, no. 5596, p. 1219–1221, https://doi.org/10.1126/science.1078115.

Kohn, M.J., Wieland, M.S., Parkinson, C.D., and Upreti, B.N., 2005, Five generations of monazite in Langtang gneisses: Implications for chronology of the Himalayan metamorphic core: Journal of Metamorphic Geology, v. 23, no. 5, p. 399–406, https://doi.org/10.1111/j.1525-1314.2005.00584.x.

Kong, X., Yin, A., and Harrison, T.M., 1997, Evaluating the role of preexisting weaknesses and topographic distributions in the Indo-Asian collision by use of a thin-shell numerical model: Geology, v. 25, no. 6, p. 527–530, https://doi.org/10.1130/0091-7613(1997)025<0527:ETROPW>2.3.CO;2.

Kröner, A., Alexeiev, D.V., Rojas-Agramonte, Y., Hegner, E., Wong, J., Xia, X., Belousova, E., Mikolaichuk, A.V., Seltmann, R., and Kiselev, V.V., 2013, Mesoproterozoic (Grenville-age) terranes in the Kyrgyz North Tianshan: Zircon ages and Nd-Hf isotopic constraints on the origin and evolution of basement blocks in the southern Central Asian orogen: Gondwana Research, v. 23, no. 1, p. 272–295, https://doi.org/10.1016/j.gr.2012.05.004.

Kröner, A., Kovach, V., Belousova, E., et al., 2014, Reassessment of continental growth during the accretionary history of the Central Asian orogenic belt: Gondwana Research, v. 25, no. 1, p. 103–125, https://doi.org/10.1016/j.gr.2012.12.023.

Kuno, H., 1968, Differentiation of basaltic magma, *in* Hess, H.H., and Poldervaart, A.A., eds., The Poldervaart Treatise on Rocks of Basaltic Composition, Volume 2: New York, Interscience, p. 623–688.

Lasserre, C., Morel, P.H., Gaudemer, Y., Tapponnier, P., Ryerson, F.J., King, G.C.P., Métivier, F., Kasser, M., Kashgarian, M., Liu, B., and Lu, T., 1999, Postglacial left slip rate and past occurrence of M≥8 earthquakes on the western Haiyuan fault, Gansu, China: Journal of Geophysical Research–Solid Earth, v. 104, p. 17,633–17,651, https://doi.org/10.1029/1998JB900082.

Lasserre, C., Gaudemer, Y., Tapponnier, P., Mériaux, A.S., Van der Woerd, J., Daoyang, Y., Ryerson, F.J., Finkel, R.C., and Caffee, M.W., 2002, Fast late Pleistocene slip rate on the Leng Long Ling segment of the Haiyuan fault, Qinghai, China: Journal of Geophysical Research–Solid Earth, v. 107, no. B11, 2276, https://doi.org/10.1029/2000JB000060.

Lease, R.O., Burbank, D.W., Zhang, H., Liu, J., and Yuan, D., 2012, Cenozoic shortening budget for the northeastern edge of the Tibetan Plateau: Is lower crustal flow necessary?: Tectonics, v. 31, no. 3, TC3011, https://doi.org/10.1029/2011TC003066.

Le Pichon, X., Fournier, M., and Jolivet, L., 1992, Kinematics, topography, shortening, and extrusion in the India-Eurasia collision: Tectonics, v. 11, p. 1085–1098, https://doi.org/10.1029/92TC01566.

Li, C.Y., Liu, Y.W., Zhu, B.C., Feng, Y.M., and Wu, H.Q., 1978, Structural Evolutions of Qinling and Qilian: Beijing, Geological Publishing House, p. 174–189 [in Chinese with English abstract].

Li, X.H., Su, L., Chung, S.L., Li, Z.X., Liu, Y., Song, B., and Liu, D.Y., 2005, Formation of the Jinchuan ultramafic intrusion and the world's third largest Ni-Cu sulfide deposit: Associated with the ~825 Ma South China mantle plume?: Geochemistry Geophysics Geosystems, v. 6, no. 11, Q11004, https://doi.org/10.1029/2005GC001006.

Li, Y.L., and Yang, J.C., 1998, Tectonic geomorphology in the Hexi Corridor, north-west China: Basin Research, v. 10, p. 345–352, https://doi.org/10.1046/j.1365-2117.1998.00070.x.

Lin, Y.H., Zhang, L.F., Ji, J.Q., and Song, S.G., 2010, $^{40}Ar/^{39}Ar$ age of Jiugequan lawsonite blueschists in northern Qilian Mountains and its petrologic significance: Chinese Science Bulletin, v. 55, p. 2021–2027, https://doi.org/10.1007/s11434-010-3239-8.

Liou, J.G., Graham, S.A., Maruyama, S., and Zhang, R.Y., 1996, Characteristics and tectonic significance of the late Proterozoic Aksu blueschists and diabasic dikes, Northwest Xinjiang, China: International Geology Review, v. 38, no. 3, p. 228–244, https://doi.org/10.1080/00206819709465332.

Liu, Y.J., Neubauer, F., Genser, J., Takasu, A., Ge, X.H., and Handler, R., 2006, $^{40}Ar/^{39}Ar$ ages of blueschist facies pelitic schists from Qingshuigou in the Northern Qilian Mountains, western China: The Island Arc, v. 15, no. 1, p. 187–198, https://doi.org/10.1111/j.1440-1738.2006.00508.x.

Liu-Zeng, J., Tapponnier, P., Gaudemer, Y., and Ding, L., 2008, Quantifying landscape differences across the Tibetan Plateau: Implications for topographic relief evolution: Journal of Geophysical Research–Earth Surface, v. 113, no. F4, F04018, https://doi.org/10.1029/2007JF000897.

Long, S., McQuarrie, N., Tobgay, T., and Grujic, D., 2011, Geometry and crustal shortening of the Himalayan fold-thrust belt, eastern and central Bhutan: Geological Society of America Bulletin, v. 123, p. 1427–1447, https://doi.org/10.1130/B30203.1.

Long, X., Yuan, C., Sun, M., Zhao, G., Xiao, W., Wang, Y., Yang, Y., and Hu, A., 2010, Archean crustal evolution of the northern Tarim craton, NW China: Zircon U-Pb and Hf isotopic constraints: Precambrian Research,

v. 180, no. 3–4, p. 272–284, https://doi.org/10.1016/j.precamres.2010.05.001.

Ludwig, K.R., 2003, User's Manual for Isoplot 3.00: A Geochronological Toolkit for Microsoft Excel: Berkeley Geochronology Center Special Publication 4, 74 p.

Ma, X., Shu, L., Santosh, M., and Li, J., 2012, Detrital zircon U-Pb geochronology and Hf isotope data from Central Tianshan suggesting a link with the Tarim block: Implications on Proterozoic supercontinent history: Precambrian Research, v. 206–207, p. 1–16, https://doi.org/10.1016/j.precamres.2012.02.015.

Mao, J., Zhang, Z., Yang, J., Song, B., Wu, M., and Zuo, G., 1998, Single-zircon dating of Precambrian strata in the west sector of the northern Qilian Mountains and its geological significance: Chinese Science Bulletin, v. 43, no. 15, p. 1289–1294, https://doi.org/10.1007/BF02884144.

Martin, A.J., Gehrels, G.E., and DeCelles, P.G., 2007, The tectonic significance of (U, Th)/Pb ages of monazite inclusions in garnet from the Himalaya of central Nepal: Chemical Geology, v. 244, no. 1–2, p. 1–24, https://doi.org/10.1016/j.chemgeo.2007.05.003.

Mattinson, C.G., Wooden, J.L., Liou, J.G., Bird, D.K., and Wu, C.L., 2006, Age and duration of eclogite-facies metamorphism, North Qaidam HP/UHP terrane, western China: American Journal of Science, v. 306, no. 9, p. 683–711, https://doi.org/10.2475/09.2006.01.

Mattinson, C.G., Menold, C.A., Zhang, J.X., and Bird, D.K., 2007, High- and ultrahigh-pressure metamorphism in the North Qaidam and South Altyn terranes, western China: International Geology Review, v. 49, no. 11, p. 969–995, https://doi.org/10.2747/0020-6814.49.11.969.

Meng, F.C., Zhang, J.X., Ker, C.M., and Li, J.P., 2010, Constraints on the evolution of the North Qilian ocean basin: MOR-type and supra-subduction zone-type ophiolites from Dachadaban: Acta Petrologica et Mineralogica, v. 29, no. 5, p. 453–466.

Menold, C.A., Manning, C.E., Yin, A., Tropper, P., Chen, X.H., and Wang, X.F., 2009, Metamorphic evolution, mineral chemistry and thermobarometry of orthogneiss hosting ultrahigh-pressure eclogites in the North Qaidam metamorphic belt, western China: Journal of Asian Earth Sciences, v. 35, no. 3–4, p. 273–284, https://doi.org/10.1016/j.jseaes.2008.12.008.

Menold, C.A., Grove, M., Manning, C.E., Yin, A., Young, E.D., and Ziegler, K., 2016, Argon and oxygen isotopic evidence for pervasive metasomatism during ultrahigh-pressure continental subduction: Earth and Planetary Science Letters, v. 446, p. 56–67, https://doi.org/10.1016/j.epsl.2016.04.010.

Métivier, F., Gaudemer, Y., Tapponnier, P., and Meyer, B., 1998, Northeastward growth of the Tibet Plateau deduced from balanced reconstruction of two depositional areas: The Qaidam and Hexi Corridor basins, China: Tectonics, v. 17, no. 6, p. 823–842, https://doi.org/10.1029/98TC02764.

Meyer, B., Tapponnier, P., Bourjot, L., Métivier, F., Gaudemer, Y., Peltzer, G., Shunmin, G., and Zhitai, C., 1998, Crustal thickening in Gansu-Qinghai, lithospheric mantle subduction, and oblique, strike-slip controlled growth of the Tibet Plateau: Geophysical Journal International, v. 135, p. 1–47, https://doi.org/10.1046/j.1365-246X.1998.00567.x.

Mitra, S., and Namson, J., 1989, Equal-area balancing: American Journal of Science, v. 289, no. 5, p. 563–599, https://doi.org/10.2475/ajs.289.5.563.

Mo, X., Hou, Z., Niu, Y., Dong, G., Qu, X., Zhao, Z., and Yang, Z., 2007, Mantle contributions to crustal thickening during continental collision: Evidence from Cenozoic igneous rocks in southern Tibet: Lithos, v. 96, no. 1–2, p. 225–242, https://doi.org/10.1016/j.lithos.2006.10.005.

Molnar, P., and Stock, J.M., 2009, Slowing of India's convergence with Eurasia since 20 Ma and its implications for Tibetan mantle dynamics: Tectonics, v. 28, no. 3, TC3001, https://doi.org/10.1029/2008TC002271.

Molnar, P., and Tapponnier, P., 1975, Cenozoic tectonics of Asia: Effects of a continental collision: Science, v. 189, no. 4201, p. 419–426, https://doi.org/10.1126/science.189.4201.419.

Molnar, P., England, P., and Martinod, J., 1993, Mantle dynamics, uplift of the Tibetan Plateau, and the Indian monsoon: Reviews of Geophysics, v. 31, no. 4, p. 357–396, https://doi.org/10.1029/93RG02030.

Montel, J.M., Kornprobst, J., and Vielzeuf, D., 2000, Preservation of old U-Th-Pb ages in shielded monazite: Example from the Beni Bousera Hercynian kinzigites (Morocco): Journal of Metamorphic Geology, v. 18, no. 3, p. 335–342, https://doi.org/10.1046/j.1525-1314.2000.00261.x.

Murphy, M.A., Yin, A., Harrison, T.M., Dürr, S.B., Chen, Z., Ryerson, F.J., Kidd, S.F., Wang, X., and Zhou, X., 1997, Did the Indo-Asian collision alone create the Tibetan Plateau?: Geology, v. 25, no. 8, p. 719–722, https://doi.org/10.1130/0091-7613(1997)025<0719:DTIACA>2.3.CO;2.

Pan, G., Ding, J., Yao, D., and Wang, L., 2004, Geological Map of Qinghai-Xiang (Tibet) Plateau and Adjacent Areas: Chengdu, China, Chengdu Institute of Geology and Mineral Resources, China Geological Survey, Chengdu Cartographic Publishing House, scale 1:1,500,000.

Pattison, D.R., Chacko, T., Farquhar, J., and McFarlane, C.R., 2003, Temperatures of granulite-facies metamorphism: Constraints from experimental phase equilibria and thermobarometry corrected for retrograde exchange: Journal of Petrology, v. 44, no. 5, p. 867–900, https://doi.org/10.1093/petrology/44.5.867.

Pearce, J.A., Harris, N.B., and Tindle, A.G., 1984, Trace element discrimination diagrams for the tectonic interpretation of granitic rocks: Journal of Petrology, v. 25, no. 4, p. 956–983, https://doi.org/10.1093/petrology/25.4.956.

Peltzer, G., and Tapponnier, P., 1988, Formation and evolution of strike-slip faults, rifts, and basins during the India-Asia collision: An experimental approach: Journal of Geophysical Research–Solid Earth, v. 93, no. B12, p. 15,085–15,117, https://doi.org/10.1029/JB093iB12p15085.

Peltzer, G., Tapponnier, P., and Armijo, R., 1989, Magnitude of late Quaternary left-lateral displacements along the north edge of Tibet: Science, v. 246, no. 4935, p. 1285–1289, https://doi.org/10.1126/science.246.4935.1285.

Pullen, A., Kapp, P., Gehrels, G.E., Vervoort, J.D., and Ding, L., 2008, Triassic continental subduction in central Tibet and Mediterranean-style closure of the Paleo-Tethys Ocean: Geology, v. 36, no. 5, p. 351–354, https://doi.org/10.1130/G24435A.1.

Pyle, J.M., and Spear, F.S., 2003, Four generations of accessory-phase growth in low pressure migmatites from SW New Hampshire: The American Mineralogist, v. 88, p. 338–351, https://doi.org/10.2138/am-2003-2-311.

Pyle, J.M., Spear, F.S., Wark, D.A., Daniel, C.G., and Storm, L.C., 2005, Contributions to precision and accuracy of monazite microprobe ages: The American Mineralogist, v. 90, no. 4, p. 547–577, https://doi.org/10.2138/am.2005.1340.

Qi, X.X., 2003, Large Size Ductile Strike-Slip Shearing and the Formation of Qilian Caledonian Orogen [Ph.D. thesis]: Beijing, Chinese Academy of Geological Sciences, 119 p.

Qian, Q., Wang, Y.M., Li, H.M., Jia, X.Q., Han, S., and Zhang, Q., 1998, Geochemical characteristics and genesis of diorites from Laohushan, Gansu Province: Acta Petrolei Sinica, v. 14, p. 520–528 [in Chinese with English abstract].

Qinghai Bureau of Geology and Mineral Resources (B.G.M.R.), 1991, Regional Geology of Qinghai Province: Beijing, Geological Publishing House, 662 p.

Quan, S., Jia, Q., Guo, Z., and Wang, W., 2006, Basic characterists of granitoids related to tungsten mineralization in the Qilian Mountains: Mineralium Deposita, v. 25, p. 143–146.

Quidelleur, X., Grove, M., Lovera, O.M., Harrison, T.M., Yin, A., and Ryerson, F.J., 1997, Thermal evolution and slip history of the Renbu Zedong thrust, southeastern Tibet: Journal of Geophysical Research, v. 102, no. B2, p. 2659–2679, https://doi.org/10.1029/96JB02483.

Rasmussen, B., and Muhling, J.R., 2007, Monazite begets monazite: Evidence for dissolution of detrital monazite and reprecipitation of syntectonic monazite during low grade regional metamorphism: Contributions to Mineralogy and Petrology, v. 154, p. 675–689, https://doi.org/10.1007/s00410-007-0216-6.

Robinson, D.M., DeCelles, P.G., and Copeland, P., 2006, Tectonic evolution of the Himalayan thrust belt in western Nepal: Implications for channel flow models: Geological Society of America Bulletin, v. 118, no. 7–8, p. 865–885, https://doi.org/10.1130/B25911.1.

Rojas-Agramonte, Y., Kröner, A., Demoux, A., Xia, X., Wang, W., Donskaya, T., Liu, D., and Sun, M., 2011, Detrital and xenocrystic zircon ages from Neoproterozoic to Palaeozoic arc terranes of Mongolia: Significance for the origin of crustal fragments in the Central Asian orogenic belt: Gondwana Research, v. 19, no. 3, p. 751–763, https://doi.org/10.1016/j.gr.2010.10.004.

Royden, L.H., Burchfiel, B.C., and van der Hilst, R.D., 2008, The geological evolution of the Tibetan Plateau: Science, v. 321, no. 5892, p. 1054–1058, https://doi.org/10.1126/science.1155371.

Royden, L.H., Burchfiel, B.C., King, R.W., Wang, E., Chen, Z., Shen, F., and Liu, Y., 1997, Surface deformation and lower crustal flow in eastern Tibet: Science, v. 276, no. 5313, p. 788–790, https://doi.org/10.1126/science.276.5313.788.

Ryan, W.B.F., Carbotte, S.M., Coplan, J.O., et al., 2009, Global multi-resolution topography synthesis: Geochemistry Geophysics Geosystems, v. 10, Q03014, https://doi.org/10.1029/2008GC002332.

Scherrer, N.C., Engi, M., Gnos, E., Jakob, V., and Leichti, A., 2000, Monazite analyses: From sample preparation to microprobe age dating and REE quantification: Schweizerische Mineralogische und Petrographische Mitteilungen, v. 80, p. 93–105.

Scotese, C.R., and McKerrow, W.S., 1990, Revised world maps and introduction, in McKerrow, W.S., and Scotese, C.R., eds., Palaeozoic Palaeogeography and Biogeography: Geological Society of London Memoir 12, p. 1–21, https://doi.org/10.1144/GSL.MEM.1990.012.01.01.

Şengör, A.M.C., and Natal'in, B.A., 1996, Paleotectonics of Asia: Fragments of a synthesis, in Yin, A., and Harrison, T.M., eds., The Tectonics of Asia: New York, Cambridge University Press, p. 486–640.

Shervais, J.W., 2001, Birth, death, and resurrection: The life cycle of supra-subduction zone ophiolites: Geochemistry Geophysics Geosystems, v. 2, no. 1, 1010, https://doi.org/10.1029/2000GC000080.

Shi, R.D., Yang, J.S., and Wu, C.L., 2004, First SHRIMP dating for the formation of the late Sinian Yushigou ophiolite North Qilian Mountains: Acta Geologica Sinica, v. 78, p. 649–657 [in Chinese with English abstract].

Sievers, N.E., Menold, C.A., Grove, M., and Coble, M.A., 2017, White mica trace element and boron isotope evidence for distinctive infiltration events during exhumation of deeply subducted continental crust: International Geology Review, v. 59, no. 5–6, p. 621–638.

Sloan, R.A., Jackson, J.A., McKenzie, D., and Priestley, K., 2011, Earthquake depth distributions in Central Asia, and their relations with lithosphere thickness, shortening and extension: Geophysical Journal International, v. 185, no. 1, p. 1–29, https://doi.org/10.1111/j.1365-246X.2010.04882.x.

Smith, A.D., 2006, The geochemistry and age of ophiolitic strata of the Xinglongshan Group: Implications for the amalgamation of the Central Qilian belt: Journal of Asian Earth Sciences, v. 28, no. 2–3, p. 133–142, https://doi.org/10.1016/j.jseaes.2005.09.014.

Smith, H.A., and Barreiro, B., 1990, Monazite U-Pb dating of staurolite grade metamorphism in pelitic schists: Contributions to Mineralogy and Petrology, v. 105, no. 5, p. 602–615, https://doi.org/10.1007/BF00302498.

Snow, C.A., 2006, A reevaluation of tectonic discrimination diagrams and a new probabilistic approach using large geochemical databases: Moving beyond binary and ternary plots: Journal of Geophysical Research, v. 111, B06206, https://doi.org/10.1029/2005JB003799.

Sobel, E.R., and Arnaud, N., 1999, A possible middle Paleozoic suture in the Altyn Tagh, NW China: Tectonics, v. 18, no. 1, p. 64–74, https://doi.org/10.1029/1998TC900023.

Sone, M., and Metcalfe, I., 2008, Parallel Tethyan sutures in mainland Southeast Asia: New insights for Palaeo-

Tethys closure and implications for the Indosinian orogeny: Comptes Rendus Geoscience, v. 340, no. 2–3, p. 166–179, https://doi.org/10.1016/j.crte.2007.09.008.

Song, S., Zhang, L., Niu, Y., Su, L., Song, B., and Liu, D., 2005, Evolution from oceanic subduction to continental collision: a case study from the Northern Tibetan Plateau based on geochemical and geochronological data: Journal of Petrology, v. 47, no. 3, p. 435–455.

Song, S.G., Zhang, L.F., Niu, Y.L., Su, L., Song, B., and Liu, D.Y., 2006, Evolution from oceanic subduction to continental collision: A case study of the Northern Tibetan Plateau inferred from geochemical and geochronological data: Journal of Petrology, v. 47, p. 435–455, https://doi.org/10.1093/petrology/egi080.

Song, S.G., Zhang, L.F., Niu, Y., Wei, C.J., Liou, J.G., and Shu, G.M., 2007, Eclogite and carpholite-bearing metasedimentary rocks in the North Qilian suture zone, NW China: Implications for early Palaeozoic cold oceanic subduction and water transport into mantle: Journal of Metamorphic Geology, v. 25, no. 5, p. 547–563, https://doi.org/10.1111/j.1525-1314.2007.00713.x.

Song, S.G., Niu, Y., Su, L., and Xia, X., 2013, Tectonics of the North Qilian orogen, NW China: Gondwana Research, v. 23, no. 4, p. 1378–1401, https://doi.org/10.1016/j.gr.2012.02.004.

Song, S.G., Niu, Y., Su, L., Zhang, C., and Zhang, L., 2014, Continental orogenesis from ocean subduction, continent collision/subduction, to orogen collapse, and orogen recycling: The example of the North Qaidam UHPM belt, NW China: Earth-Science Reviews, v. 129, p. 59–84, https://doi.org/10.1016/j.earscirev.2013.11.010.

Spear, F.S., 1993, Metamorphic Phase Equilibria and Pressure-Temperature-Time Paths: Washington, D.C., Mineralogical Society of America Monograph, 799 p.

Stampfli, G.M., and Borel, G.D., 2002, A plate tectonic model for the Paleozoic and Mesozoic constrained by dynamic plate boundaries and restored synthetic oceanic isochrones: Earth and Planetary Science Letters, v. 196, no. 1–2, p. 17–33, https://doi.org/10.1016/S0012-821X(01)00588-X.

Stern, C.R., 2011, Subduction erosion: Rates, mechanisms, and its role in arc magmatism and the evolution of the continental crust and mantle: Gondwana Research, v. 20, no. 2–3, p. 284–308, https://doi.org/10.1016/j.gr.2011.03.006.

Stern, R.A., and Berman, R.G., 2001, Monazite U-Pb and Th-Pb geochronology by ion microprobe, with an application to in situ dating of an Archean metasedimentary rock: Chemical Geology, v. 172, no. 1–2, p. 113–130, https://doi.org/10.1016/S0009-2541(00)00239-4.

Stern, R.J., 2004, Subduction initiation: Spontaneous and induced: Earth and Planetary Science Letters, v. 226, no. 3-4, p. 275–292, https://doi.org/10.1016/S0012-821X(04)00498-4.

Su, J., Zhang, X., Hu, N., Fu, G., and Zhang, H., 2004, Geochemical characteristics and genesis of adakite-like granites at Yema Nanshan in the western segment of the Central Qilian Mountains: Chinese Geology, v. 31, p. 365–371 [with English abstract].

Suppe, J., 1983, Geometry and kinematics of fault-bend folding: American Journal of Science, v. 283, no. 7, p. 684–721, https://doi.org/10.2475/ajs.283.7.684.

Tapponnier, P., Peltzer, G., Le Dain, A.Y., Armijo, R., and Cobbold, P., 1982, Propagating extrusion tectonics in Asia: New insights from simple experiments with plasticine: Geology, v. 10, no. 12, p. 611–616, https://doi.org/10.1130/0091-7613(1982)10<611:PETIAN>2.0.CO;2.

Tapponnier, P., Meyer, B., Avouac, J.P., Peltzer, G., Gaudemer, Y., Guo, S., Xiang, H., Yin, K., Chen, Z., Cai, S., and Dai, H., 1990, Active thrusting and folding in the Qilian Shan, and decoupling between upper crust and mantle in northeastern Tibet: Earth and Planetary Science Letters, v. 97, p. 382–403, https://doi.org/10.1016/0012-821X(90)90053-Z.

Tapponnier, P., Zhiqin, X., Roger, F., Meyer, B., Arnaud, N., Wittlinger, G., and Jingsui, Y., 2001, Oblique stepwise rise and growth of the Tibet Plateau: Science, v. 294, no. 5547, p. 1671–1677, https://doi.org/10.1126/science.105978.

Taylor, M., and Yin, A., 2009, Active structures of the Himalayan-Tibetan orogen and their relationships to earthquake distribution, contemporary strain field, and Cenozoic volcanism: Geosphere, v. 5, no. 3, p. 199–214, https://doi.org/10.1130/GES00217.1.

Tseng, C.Y., Yang, H.Y., Yusheng, W., Dunyi, L., Wen, D.J., Lin, T.C., and Tung, K.A., 2006, Finding of Neoproterozoic (~775 Ma) magmatism recorded in metamorphic complexes from the North Qilian orogen: Evidence from SHRIMP zircon U-Pb dating: Chinese Science Bulletin, v. 51, no. 8, p. 963–970, https://doi.org/10.1007/s11434-006-0963-1.

Tseng, C.Y., Yang, H.J., Yang, H.Y., Liu, D.Y., Tsai, C.L., Wu, H.Q., and Zuo, G.C., 2007, The Dongcaohe ophiolite from the North Qilian Mountains: A fossil oceanic crust of the Paleo-Qilian Ocean: Chinese Science Bulletin, v. 52, p. 2390–2401, https://doi.org/10.1007/s11434-007-0300-3.

Tseng, C.Y., Yang, H.J., Yang, H.Y., Liu, D., Wu, C., Cheng, C.K., Chen, C.H., and Ker, C.M., 2009, Continuity of the North Qilian and North Qinling orogenic belts, Central orogenic system of China: Evidence from newly discovered Paleozoic adakitic rocks: Gondwana Research, v. 16, p. 285–293, https://doi.org/10.1016/j.gr.2009.04.003.

Tung, K., Yang, H., Liu, D., Zhang, J., Tseng, C., and Wan, Y., 2007, SHRIMP U-Pb geochronology of the detrital zircons from the Longshoushan Group and its tectonic significance: Chinese Science Bulletin, v. 52, no. 10, p. 1414–1425, https://doi.org/10.1007/s11434-007-0189-x.

Tung, K.A., Yang, H.Y., Liu, D.Y., Zhang, J.X., Yang, H.J., Shau, Y.H., and Tseng, C.Y., 2012, The amphibolite-facies metamorphosed mafic rocks from the Maxianshan area, Qilian block, NW China: A record of early Neoproterozoic arc magmatism: Journal of Asian Earth Sciences, v. 46, p. 177–189, https://doi.org/10.1016/j.jseaes.2011.12.006.

van Hinsbergen, D.J., Kapp, P., Dupont-Nivet, G., Lippert, P.C., DeCelles, P.G., and Torsvik, T.H., 2011, Restoration of Cenozoic deformation in Asia and the size of Greater India: Tectonics, v. 30, no. 5, TC5003, https://doi.org/10.1029/2011TC002908.

van Hinsbergen, D.J., Lippert, P.C., Dupont-Nivet, G., McQuarrie, N., Doubrovine, P.V., Spakman, W., and Torsvik, T.H., 2012, Greater India Basin hypothesis and a two-stage Cenozoic collision between India and Asia: Proceedings of the National Academy of Sciences of the United States of America, v. 109, no. 20, p. 7659–7664, https://doi.org/10.1073/pnas.1117262109.

Vincent, S.J., and Allen, M.B., 1999, Evolution of the Minle and Chaoshui Basins, China: Implications for Mesozoic strike-slip basin formation in Central Asia: Geological Society of America Bulletin, v. 111, no. 5, p. 725–742, https://doi.org/10.1130/0016-7606(1999)111<0725:EOTMAC>2.3.CO;2.

Wakabayashi, J., Ghatak, A., and Basu, A.R., 2010, Suprasubduction-zone ophiolite generation, emplacement, and initiation of subduction: A perspective from geochemistry, metamorphism, geochronology, and regional geology: Geological Society of America Bulletin, v. 122, no. 9–10, p. 1548–1568, https://doi.org/10.1130/B30017.1.

Wallis, S., Tsujimori, T., Aoya, M., Kawakami, T., Terada, K., Suzuki, K., and Hyodo, H., 2003, Cenozoic and Mesozoic metamorphism in the Longmenshan orogen: Implications for geodynamic models of eastern Tibet: Geology, v. 31, no. 9, p. 745–748, https://doi.org/10.1130/G19562.1.

Wan, Y., Xu, Z., Yang, J., and Zhang, J., 2001, Ages and Compositions of the Precambrian High-Grade Basement of the Qilian Terrane and its Adjacent Areas: Acta Geologica Sinica [English Edition], v. 75, p. 375–384.

Wan, Y., Xu, Z., Yang, J., and Zhang, J., 2003, The Precambrian High-Grade Basement of the Qilian Terrane and Neighboring Areas: Its Ages and Compositions: Diqiu Xuebao, v. 24, p. 319–324 [in Chinese with English abstract].

Wan, Y., Xie, H., Yang, H., et al., 2013, Is the Ordos block Archean or Paleoproterozoic in age? Implications for the Precambrian evolution of the North China craton:

American Journal of Science, v. 313, no. 7, p. 683–711, https://doi.org/10.2475/07.2013.03.

Wang, C., Liu, L., Wang, Y.H., He, S.P., Li, R.S., Li, M., Yang, W.Q., Cao, Y.T., Collins, A.S., Shi, C., and Wu, Z.N., 2015a, Recognition and tectonic implications of an extensive Neoproterozoic volcano-sedimentary rift basin along the southwestern margin of the Tarim craton, northwestern China: Precambrian Research, v. 257, p. 65–82, https://doi.org/10.1016/j.precamres.2014.11.022.

Wang, C., Zhang, J.H., Li, M., Li, R.S., and Peng, Y., 2015b, Generation of ca. 900–870Ma bimodal rifting volcanism along the southwestern margin of the Tarim craton and its implications for the Tarim–North China connection in the early Neoproterozoic: Journal of Asian Earth Sciences, v. 113, p. 610–625, https://doi.org/10.1016/j.jseaes.2015.08.002.

Wang, E., and Burchfiel, B.C., 2004, Late Cenozoic right-lateral movement along the Wenquan fault and associated deformation: Implications for the kinematic history of the Qaidam Basin, northeastern Tibetan Plateau: International Geology Review, v. 46, no. 10, p. 861–879, https://doi.org/10.2747/0020-6814.46.10.861.

Wang, H., Gao, R., Zeng, L., Kuang, Z., Xue, A., Li, W., Xiong, X., and Huang, W., 2014, Crustal structure and Moho geometry of the northeastern Tibetan Plateau as revealed by SinoProbe-02 deep seismic-reflection profiling: Tectonophysics, v. 636, p. 32–39, https://doi.org/10.1016/j.tecto.2014.08.010.

Wang, L.Q., Pan, G.T., Ding, J., and Yao, D.S., compiler, 2013, Geological Map of the Tibetan Plateau at a Scale of 1:1.5 M with Explanations: Beijing, Geological Publishing House, 288 p.

Wang, Q., and Liu, X.Y., 1976, The Ancient Oceanic Crust and its Tectonic Implications, North Qilian Mountains, China: Scientia Geologica Sinica, v. 1, p. 42–55 [in Chinese with English abstract].

Wang, Q., Zhang, P.Z., Freymueller, J.T., Bilham, R., Larson, K.M., Lai, X.A., You, X., Niu, Z., Wu, J., Li, Y., Liu, J., Yang, Z., and Chen, Q., 2001, Present-day crustal deformation in China constrained by global positioning system measurements: Science, v. 294, no. 5542, p. 574–577, https://doi.org/10.1126/science.1063647.

Wang, Q.M., and Coward, M.P., 1993, The Jiuxi Basin, Hexi Corridor, NW China: Foreland structural features and hydrocarbon potential: Journal of Petroleum Geology, v. 16, no. 2, p. 169–182, https://doi.org/10.1111/j.1747-5457.1993.tb00104.x.

Wang, T., Hong, D.W., Jahn, B.M., Tong, Y., Wang, Y.B., Han, B.F., and Wang, X.X., 2006, Timing, petrogenesis, and setting of Paleozoic synorogenic intrusions from the Altai Mountains, Northwest China: Implications for the tectonic evolution of an accretionary orogen: The Journal of Geology, v. 114, no. 6, p. 735–751, https://doi.org/10.1086/507617.

Webb, A.A.G., 2013, Preliminary balanced palinspastic reconstruction of Cenozoic deformation across the Himachal Himalaya (northwestern India): Geosphere, v. 9, no. 3, p. 572–587, https://doi.org/10.1130/GES00787.1.

Willett, S.D., and Beaumont, C., 1994, Subduction of Asian lithospheric mantle beneath Tibet inferred from models of continental collision: Nature, v. 369, no. 6482, p. 642–645, https://doi.org/10.1038/369642a0.

Williams, I.S., 1998, U-Th-Pb geochronology by ion microprobe: Reviews in Economic Geology, v. 7, no. 1, p. 1–35.

Williams, M.L., Jercinovic, M.J., and Hetherington, C.J., 2007, Microprobe monazite geochronology: Understanding geologic processes by integrating composition and chronology: Annual Review of Earth and Planetary Sciences, v. 35, no. 1, p. 137–175, https://doi.org/10.1146/annurev.earth.35.031306.140228.

Windley, B.F., 1992, Proterozoic collisional and accretionary orogens, *in* Condie, K.C., ed., Proterozoic Crustal Evolution: Amsterdam, Netherlands, Elsevier, p. 419–446, https://doi.org/10.1016/S0166-2635(08)70125-7.

Worley, B.A., and Wilson, C.J., 1996, Deformation partitioning and foliation reactivation during transpressional orogenesis, an example from the Central Longmen Shan, China: Journal of Structural Geology,

v. 18, no. 4, p. 395–411, https://doi.org/10.1016/0191-8141(95)00095-U.

Wu, C., Yin, A., Zuza, A.V., Zhang, J., Liu, W., and Ding, L., 2016, Pre-Cenozoic geologic history of the central and northern Tibetan Plateau and the role of Wilson cycles in constructing the Tethyan orogenic system: Lithosphere, v. 8, no. 3, p. 254–292, https://doi.org/10.1130/L494.1.

Wu, C., Zuza, A.V., Yin, A., Liu, C., Reith, R.C., Zhang, J., Liu, W., and Zhou, Z., 2017a, Geochronology and geochemistry of Neoproterozoic granitoids in the central Qilian Shan of northern Tibet: Reconstructing the amalgamation processes and tectonic history of Asia: Lithosphere, v. 9, no. 4, p. 609–636, https://doi.org/10.1130/L640.1.

Wu, C., Wang, B., Zhou, Z., Wang, G., Zuza, A.V., Liu, C., Jiang, T., Liu, W., and Ma, S., 2017b, The relationship between magma and mineralization in Chaobuleng iron polymetallic deposit, Inner Mongolia: Gondwana Research, v. 45, p. 228–253, https://doi.org/10.1016/j.gr.2017.02.006.

Wu, C.L., Yang, J.S., Yang, H.Y., Wooden, J., Shi, R.D., Chen, S.Y., and Zheng, Q.G., 2004, Dating of two types of granite from North Qilian, China: Acta Petrolei Sinica, v. 20, p. 425–432.

Wu, C.L., Yao, S., Zeng, L., Yang, J., Wooden, J., Chen, S., and Mazadab, F., 2006, Double subduction of the early Paleozoic North Qilian oceanic plate: Evidence from granites in the central segment of North Qilian, NW China: Geology in China, v. 33, p. 1197–1208.

Wu, C.L., Xu, X.Y., Gao, Q.M., Li, X.M., Lei, M., Gao, Y.H., Frost, B.R., and Wooden, J., 2010, Early Palaeozoic granitoid magmatism and tectonic evolution in North Qilian, NW China: Yanshi Xuebao, v. 26, p. 1027–1044 [in Chinese with English abstract].

Wu, H.Q., Feng, Y.M., and Song, S.G., 1993, Metamorphism and deformation of blueschist belts and their tectonic implications, North Qilian Mountains, China: Journal of Metamorphic Geology, v. 11, p. 523–536, https://doi.org/10.1111/j.1525-1314.1993.tb00169.x.

Xia, X.H., and Song, S.G., 2010, Forming age and tectono-petrogeneses of the Jiugequan ophiolite in the North Qilian Mountain, NW China: Chinese Science Bulletin, v. 55, p. 1899–1907, https://doi.org/10.1007/s11434-010-3207-3.

Xia, L., Xia, Z., Zhao, J., Xu, X., Yang, H., and Zhao, D., 1999, Determination of properties of Proterozoic continental flood basalts of western part from North Qilian Mountains: Science in China, ser. D, Earth Sciences, v. 42, no. 5, p. 506–514, https://doi.org/10.1007/BF02875244.

Xia, L.Q., Xia, Z.C., and Xu, X.Y., 2003, Magmagenesis in the Ordovician in back basins of the northern Qilian Mountains, China: Geological Society of America Bulletin, v. 115, p. 1510–1522, https://doi.org/10.1130/B25269.1.

Xia, X.H., Song, S., and Niu, Y., 2012, Tholeiite-boninite terrane in the North Qilian suture zone: Implications for subduction initiation and back-arc basin development: Chemical Geology, v. 328, p. 259–277, https://doi.org/10.1016/j.chemgeo.2011.12.001.

Xiang, Z.Q., Lu, S.N., Li, H.K., Li, H.M., Song, B., and Zheng, J.K., 2007, SHRIMP U-Pb zircon age of gabbro in Aoyougou in the western segment of the North Qilian Mountains, China, and its geological implications: Geological Bulletin of China, v. 26, p. 1686–1691.

Xiao, W., Windley, B.F., Hao, J., and Zhai, M., 2003, Accretion leading to collision and the Permian Solonker suture, Inner Mongolia, China: Termination of the Central Asian orogenic belt: Tectonics, v. 22, no. 6, 1069, https://doi.org/10.1029/2002TC001484.

Xiao, W., Zhang, L.C., Qin, K.Z., Sun, S., and Li, J.L., 2004, Paleozoic accretionary and collisional tectonics of the eastern Tienshan (China): Implications for the continental growth of Central Asia: American Journal of Science, v. 304, p. 370–395, https://doi.org/10.2475/ajs.304.4.370.

Xiao, W., Windley, B.F., Yong, Y., Yan, Z., Yuan, C., Liu, C., and Li, J., 2009, Early Paleozoic to Devonian multiple-accretionary model for the Qilian Shan, NW China: Journal of Asian Earth Sciences, v. 35, no. 3–4, p. 323–333, https://doi.org/10.1016/j.jseaes.2008.10.001.

Xiao, W., Li, S., Santosh, M., and Jahn, B.M., 2012, Orogenic belts in Central Asia: Correlations and connections: Journal of Asian Earth Sciences, v. 49, p. 1–6, https://doi.org/10.1016/j.jseaes.2012.03.001.

Xiao, X.C., Chen, G.M., and Zhu, Z.Z., 1978, A preliminary study on the tectonics of ancient ophiolites in the Qilian Mountain, northwest China: Acta Geologica Sinica, v. 4, p. 279–295 [in Chinese with English abstract].

Xie, L., Zhang, Y., Zhang, H., Sun, J., and Wu, F., 2008, In situ simultaneous determination of trace elements, U-Pb and Lu-Hf isotopes in zircon and baddeleyite: Chinese Science Bulletin, v. 53, no. 10, p. 1565–1573.

Xiong, Z., Zhang, H., and Zhang, J., 2012, Petrogenesis and tectonic implications of the Maozangsi and Huangyanghe granitic intrusions in Lenglongling area, the eastern part of North Qilian Mountain, NW China: Earth Science Frontiers, v. 19, p. 214–227.

Xiu, Q.Y., Lu, S.N., Yu, H.F., and Yang, C.L., 2002, The isotopic age evidence for main Longshoushan Group contributing to Palaeoproterozoic: Progress in Precambrian Research, v. 25, no. 2, p. 93–96.

Xu, X., He, S., Wang, H., Zhang, E., Chen, J., and Sun, J., 2008, Tectonic framework of North Qilian Mountain and North Qilian Mountain conjunction area in early Paleozoic: A study of the evidence from strata and tectonic-magmatic events: Northwest Geology, v. 41, p. 1–21 [in Chinese with English abstract].

Xu, X., Song, S., Su, L., Li, Z., Niu, Y., and Allen, M.B., 2015, The 600–580 Ma continental rift basalts in North Qilian Shan, northwest China: Links between the Qilian-Qaidam block and SE Australia, and the reconstruction of East Gondwana: Precambrian Research, v. 257, p. 47–64, https://doi.org/10.1016/j.precamres.2014.11.017.

Xu, Z.Q., He, B.Z., Zhang, C.L., Zhang, J.X., Wang, Z.M., and Cai, Z.H., 2013, Tectonic framework and crustal evolution of the Precambrian basement of the Tarim block in NW China: New geochronological evidence from deep drilling samples: Precambrian Research, v. 235, p. 150–162, https://doi.org/10.1016/j.precamres.2013.06.001.

Xue, N., Wang, J., Tan, S.X., Lin, H., Li, W.F., Ren, J.Q., and Liu, S.J., 2009, Geological significance of granite of Jinningian age in Yeniugou-Tuole region on the northern margin of Central Qilian block: Journal of Qinghai University, v. 27, p. 23–28.

Yakovlev, P.V., and Clark, M.K., 2014, Conservation and redistribution of crust during the Indo-Asian collision: Tectonics, v. 33, no. 6, p. 1016–1027, https://doi.org/10.1002/2013TC003469.

Yan, Z., Xiao, W., Wang, Z., and Li, J., 2007, Integrated analyses constraining the provenance of sandstones, mudstones, and conglomerates: A case study, the Laojunshan conglomerate, Qilian orogen, northwest China: Canadian Journal of Earth Sciences, v. 44, no. 7, p. 961–986, https://doi.org/10.1139/e07-010.

Yan, Z., Xiao, W.J., Windley, B.F., Wang, Z.Q., and Li, J.L., 2010, Silurian clastic sediments in the North Qilian Shan, NW China: Chemical and isotopic constraints on their forearc provenance with implications for the Paleozoic evolution of the Tibetan Plateau: Sedimentary Geology, v. 231, no. 3–4, p. 98–114, https://doi.org/10.1016/j.sedgeo.2010.09.001.

Yang, J., Xu, Z., Zhang, J., Song, S., Wu, C., Shi, R., Li, H., and Brunel, M., 2002, Early Paleozoic North Qaidam UHP metamorphic belt on the north-eastern Tibetan plateau and a paired subduction model: Terra Nova, v. 14, no. 5, p. 397–404, https://doi.org/10.1046/j.1365-3121.2002.00438.x.

Yang, J.H., Du, Y.S., Cawood, P.A., and Xu, Y.J., 2009, Silurian collisional suturing onto the southern margin of the North China craton: Detrital zircon geochronology constraints from the Qilian orogen: Sedimentary Geology, v. 220, p. 95–104, https://doi.org/10.1016/j.sedgeo.2009.07.001.

Yang, J.H., Du, Y., Cawood, P.A., and Xu, Y., 2012, From subduction to collision in the northern Tibetan Plateau: Evidence from the Early Silurian clastic rocks, northwestern China: The Journal of Geology, v. 120, p. 49–67, https://doi.org/10.1086/662717.

Yang, J.S., Xu, Z.Q., Zhang, J.X., Chu, C.Y., Zhang, R., and Liou, J.G., 2001, Tectonic significance of early Paleozoic high-pressure rocks in Altun-Qaidam-Qilian Mountains, northwest China, *in* Hendrix, M.S., and Davis, G.A., eds., Paleozoic and Mesozoic Tectonic Evolution of Central Asia: From Continental Assembly to Intracontinental Deformation: Geological Society of America Memoir 194, p. 151–170, https://doi.org/10.1130/0-8137-1194-0.151.

Yang, J.S., Wu, C.L., Zhang, J.X., Shi, R.D., Meng, F.C., Wooden, J., and Yang, H.Y., 2006, Protolith of eclogites in the north Qaidam and Altun UHP terrane, NW China: Earlier oceanic crust?: Journal of Asian Earth Sciences, v. 28, p. 185–204, https://doi.org/10.1016/j.jseaes.2005.09.020.

Yang, Y., and Liu, M., 2009, Crustal thickening and lateral extrusion during the Indo-Asian collision: A 3D viscous flow model: Tectonophysics, v. 465, no. 1–4, p. 128–135, https://doi.org/10.1016/j.tecto.2008.11.002.

Ye, Z., Gao, R., Li, Q., Zhang, H., Shen, X., Liu, X., and Gong, C., 2015, Seismic evidence for the North China plate underthrusting beneath northeastern Tibet and its implications for plateau growth: Earth and Planetary Science Letters, v. 426, p. 109–117, https://doi.org/10.1016/j.epsl.2015.06.024.

Yin, A., 2010, Cenozoic tectonic evolution of Asia: A preliminary synthesis: Tectonophysics, v. 488, p. 293–325, https://doi.org/10.1016/j.tecto.2009.06.002.

Yin, A., and Harrison, T.M., 2000, Geologic evolution of the Himalayan-Tibetan orogen: Annual Review of Earth and Planetary Sciences, v. 28, no. 1, p. 211–280, https://doi.org/10.1146/annurev.earth.28.1.211.

Yin, A., and Nie, S., 1996, A Phanerozoic palinspastic reconstruction of China and its neighboring regions, *in* Yin, A., and Harrison, T.M., eds., The Tectonics of Asia: New York, Cambridge University Press, p. 442–485.

Yin, A., Rumelhart, P.E., Butler, R., Cowgill, E., Harrison, T.M., Foster, D.A., Ingersoll, R.V., Qing, Z., Xian-Qiang, Z., Xiao-Feng, W., Hanson, A., and Raza, A., 2002, Tectonic history of the Altyn Tagh fault system in northern Tibet inferred from Cenozoic sedimentation: Geological Society of America Bulletin, v. 114, no. 10, p. 1257–1295, https://doi.org/10.1130/0016-7606(2002)114<1257:THOTAT>2.0.CO;2.

Yin, A., Dang, Y.-Q., Zhang, M., McRivette, M.W., Burgess, W.P., and Chen, X.-H., 2007a, Cenozoic tectonic evolution of Qaidam Basin and its surrounding regions (part 2): Wedge tectonics in southern Qaidam Basin and the Eastern Kunlun Range, *in* Sears, J.W., Harms, T.A., and Evenchick, C.A., eds., Whence the Mountains? Inquiries into the Evolution of Orogenic Systems: A Volume in Honor of Raymond A. Price: Geological Society of America Special Paper 433, p. 369–390, https://doi.org/10.1130/2007.2433(18).

Yin, A., Manning, C.E., Lovera, O., Menold, C.A., Chen, X., and Gehrels, G.E., 2007b, Early Paleozoic tectonic and thermomechanical evolution of ultrahigh-pressure (UHP) metamorphic rocks in the northern Tibetan Plateau, northwest China: International Geology Review, v. 49, p. 681–716, https://doi.org/10.2747/0020-6814.49.8.681.

Yin, A., Dang, Y.-Q., Wang, L.-C., Jiang, W.-M., Zhou, S.-P., Chen, X.-H., Gehrels, G.E., and McRivette, M.W., 2008a, Cenozoic tectonic evolution of Qaidam Basin and its surrounding regions (part 1): The southern Qilian Shan–Nan Shan thrust belt and northern Qaidam Basin: Geological Society of America Bulletin, v. 120, no. 7–8, p. 813–846, https://doi.org/10.1130/B26180.1.

Yin, A., Dang, Y.Q., Zhang, M., Chen, X.H., and McRivette, M.W., 2008b, Cenozoic tectonic evolution of the Qaidam Basin and its surrounding regions (Part 3): Structural geology, sedimentation, and regional tectonic reconstruction: Geological Society of America Bulletin, v. 120, no. 7–8, p. 847–876, https://doi.org/10.1130/B26232.1.

Yin, A., Dubey, C.S., Webb, A.A.G., Kelty, T.K., Grove, M., Gehrels, G.E., and Burgess, W.P., 2010, Geologic correlation of the Himalayan orogen and Indian craton: Part 1. Structural geology, U-Pb zircon geochronology, and tectonic evolution of the Shillong Plateau and its neighboring regions in NE India: Geological Society of America Bulletin, v. 122, p. 336–359, https://doi.org/10.1130/B26460.1.

Yu, X., Fu, S., Wang, Z., Li, Q., and Guo, Z., 2017, The discovery of early Paleoproterozoic high-Na trondhjemite in the northeastern Qaidam Basin: Evidence from the drilling core samples: Precambrian Research, v. 298, p. 615–628, https://doi.org/10.1016/j.precamres.2017.04.002.

Yuan, D.Y., Champagnac, J.D., Ge, W.P., Molnar, P., Zhang, P.Z., Zheng, W.J., Zhang, H.P., and Liu, X.W., 2011, Late Quaternary right-lateral slip rates of faults adjacent to the lake Qinghai, northeastern margin of the Tibetan Plateau: Geological Society of America Bulletin, v. 123, no. 9–10, p. 2016–2030, https://doi.org/10.1130/B30315.1.

Yue, H., Chen, Y.J., Sandvol, E., Ni, J., Hearn, T., et al., 2012, Lithospheric and upper mantle structure of the northeastern Tibetan Plateau: Journal of Geophysical Research–Solid Earth, v. 117, no. B5, B05307, https://doi.org/10.1029/2011JB008545.

Zhang, H.F., Zhang, B.R., Harris, N., Zhang, L., Chen, Y.L., Chen, N.S., and Zhao, Z.D., 2006, U-Pb zircon SHRIMP ages, geochemical and Sr-Nd-Pb isotopic compositions of intrusive rocks from the Longshan-Tianshui area in the southeast corner of the Qilian orogenic belt, China: Constraints on petrogenesis and tectonic affinity: Journal of Asian Earth Sciences, v. 27, no. 6, p. 751–764, https://doi.org/10.1016/j.jseaes.2005.07.008.

Zhang, J., Zhang, Z., Xu, Z., Yang, J., and Cui, J., 2001, Petrology and geochronology of eclogites from the western segment of the Altyn Tagh, northwestern China: Lithos, v. 56, no. 2–3, p. 187–206, https://doi.org/10.1016/S0024-4937(00)00052-9.

Zhang, J.X., Meng, F.C., and Wan, Y.S., 2007, A cold early Palaeozoic subduction zone in the North Qilian Mountains, NW China: Petrological and U-Pb geochronological constraints: Journal of Metamorphic Geology, v. 25, no. 3, p. 285–304, https://doi.org/10.1111/j.1525-1314.2006.00689.x.

Zhang, P., Burchfiel, B.C., Molnar, P., Zhang, W., Jiao, D., Deng, Q., Wang, Y., Royden, L., and Song, F., 1991, Amount and style of late Cenozoic deformation in the Liupan Shan area, Ningxia Autonomous Region, China: Tectonics, v. 10, no. 6, p. 1111–1129, https://doi.org/10.1029/90TC02686.

Zhang, P.Z., Shen, Z., Wang, M., et al., 2004, Continuous deformation of the Tibetan Plateau from global positioning system data: Geology, v. 32, no. 9, p. 809–812, https://doi.org/10.1130/G20554.1.

Zhang, X.T., Yang, S.D., and Yang, Z.J., 2005, Introduction to Regional Geology of Qinghai Province—Explanatory Notes of Geological Map of Qinghai Province in 1:1,000,000: Beijing, Geological Publishing House, 158 p. [in Chinese with English abstract].

Zhang, Z.M., Dong, X., Santosh, M., and Zhao, G.C., 2014, Metamorphism and tectonic evolution of the Lhasa terrane, central Tibet: Gondwana Research, v. 25, no. 1, p. 170–189, https://doi.org/10.1016/j.gr.2012.08.024.

Zhao, G., Cawood, P.A., Wilde, S.A., and Sun, M., 2002, Review of global 2.1–1.8 Ga orogens: Implications for a pre-Rodinia supercontinent: Earth-Science Reviews, v. 59, p. 125–162, https://doi.org/10.1016/S0012-8252(02)00073-9.

Zhao, G., Cawood, P.A., Li, S., Wilde, S.A., Sun, M., Zhang, J., He, Y., and Yin, C., 2012, Amalgamation of the North China craton: Key issues and discussion: Precambrian Research, v. 222–223, p. 55–76, https://doi.org/10.1016/j.precamres.2012.09.016.

Zhao, W.-L., and Morgan, W.J., 1987, Injection of Indian crust into Tibetan lower crust: A two-dimensional finite element model study: Tectonics, v. 6, no. 4, p. 489–504, https://doi.org/10.1029/TC006i004p00489.

Zheng, D., Clark, M.K., Zhang, P., Zheng, W., and Farley, K.A., 2010, Erosion, fault initiation and topographic growth of the North Qilian Shan (northern Tibetan Plateau): Geosphere, v. 6, no. 6, p. 937–941, https://doi.org/10.1130/GES00523.1.

Zheng, W.J., Zhang, P.Z., Yuan, D.Y., Zheng, D.W., Li, C., Zhang, P., Yin, J., Min, W., Heermance, R., and Chen, J., 2009, Deformation on the northern Tibetan Plateau from GPS measurement and geologic rates of the late Quaternary along the major fault: Chinese Journal of Geophysics, v. 52, p. 2491–2508.

Zheng, W.J., Zhang, P.Z., He, W.G., Yuan, D.Y., Shao, Y.X., Zheng, D.W., Ge, W.P., and Min, W., 2013, Transformation of displacement between strike-slip and crustal shortening in the northern margin of the Tibetan Plateau: Evidence from decadal GPS measurements and late Quaternary slip rates on faults: Tectonophysics, v. 584, p. 267–280, https://doi.org/10.1016/j.tecto.2012.01.006.

Zhiyi, Z., and Dean, W.T., 1996, Phanerozoic Geology of Northwest China: Beijing, China Science Press, 316 p.

Zhou, D., and Graham, S.A., 1996, Extrusion of the Altyn Tagh wedge: A kinematic model for the Altyn Tagh fault and palinspastic reconstruction of northern China: Geology, v. 24, no. 5, p. 427–430, https://doi.org/10.1130/0091-7613(1996)024<0427:EOTATW>2.3.CO;2.

Zhu, B., Kidd, W.S., Rowley, D.B., Currie, B.S., and Shafique, N., 2005, Age of initiation of the India-Asia collision in the east-central Himalaya: The Journal of Geology, v. 113, p. 265–285, https://doi.org/10.1086/428805.

Zhu, W., Zheng, B., Shu, L., et al., 2011, Neoproterozoic tectonic evolution of the Precambrian Aksu blueschist terrane, northwestern Tarim, China: Insights from LA-ICP-MS zircon U-Pb ages and geochemical data: Precambrian Research, v. 185, no. 3–4, p. 215–230, https://doi.org/10.1016/j.precamres.2011.01.012.

Zhuang, G., Hourigan, J.K., Ritts, B.D., and Kent-Corson, M.L., 2011, Cenozoic multiple-phase tectonic evolution of the northern Tibetan Plateau: Constraints from sedimentary records from Qaidam Basin, Hexi Corridor, and Subei Basin, northwest China: American Journal of Science, v. 311, no. 2, p. 116–152, https://doi.org/10.2475/02.2011.02.

Zonenshain, L.P., Kuz'min, M.I., and Natapov, L.M., 1990, Geology of the USSR: A Plate-Tectonic Synthesis: American Geophysical Union Geodynamics Monograph 21, 120 p.

Zuza, A.V., and Yin, A., 2016, Continental deformation accommodated by non-rigid passive bookshelf faulting: An example from the Cenozoic tectonic development of northern Tibet: Tectonophysics, v. 677–678, p. 227–240, https://doi.org/10.1016/j.tecto.2016.04.007.

Zuza, A.V., and Yin, A., 2017, Balkatach hypothesis: A new model for the evolution of the Pacific, Tethyan, and Paleo-Asian oceanic domains: Geosphere, v. 13, no. 5, p. 1664–1712, https://doi.org/10.1130/GES01463.1.

Zuza, A.V., Yin, A., and Wu, C., 2015, The Neoproterozoic–Paleozoic tectonic history of the Qilian Shan and its control on the development of the Tibetan Plateau's northern margin: Geological Society of America Abstracts with Programs, v. 47, no. 7, p. 38.

Zuza, A.V., Cheng, X., and Yin, A., 2016, Testing models of Tibetan Plateau formation with Cenozoic shortening estimates across the Qilian Shan–Nan Shan thrust belt: Geosphere, v. 12, no. 2, p. 501–532, https://doi.org/10.1130/GES01254.1.

Zuza, A.V., Yin, A., Lin, J., and Sun, M., 2017, Spacing and strength of active continental strike-slip faults: Earth and Planetary Science Letters, v. 457, p. 49–62, https://doi.org/10.1016/j.epsl.2016.09.041.